Spring 5-2020

Potential of Hydrodynamic Metamaterial Cloak for Drag Reduction

Rong Zou
Washington University in St. Louis

WASHINGTON UNIVERSITY IN ST. LOUIS

James McKelvey School of Engineering

Department of Mechanical Engineering and Material Science

Thesis Examination Committee:

Ramesh K. Agarwal, Chair

David Peters

Swami Karunamoorthy

Potential of Hydrodynamic Metamaterial Cloak for Drag Reduction

By

Rong Zou

A thesis presented to the James McKelvey School of Engineering

of Washington University in St. Louis

in partial fulfillment of the requirements for the degree of

Master of Science

May 2020

St. Louis, Missouri

Table of Contents

List of Tables

List of Figures

Acknowledgements

I would like to express the deepest appreciation to my research advisor Dr. Ramesh Agarwal for his significant guidance. He gave me an opportunity to join the CFD lab and guided me through the thesis.

Thanks to my committee members, Dr. David Peters and Dr. Swami Karunamoorthy for taking the time to read the thesis and attend its defense.

Thanks to my parents for their support. Studying abroad is a hard time for my family and me, but we have overcome all difficulties by our own efforts.

Thanks to all members in the CFD lab for their help during my research in these two semesters. The experience of working in the CFD lab sparked my interest in CFD and helped me to get my first job. I would like to especially thank Xiang Zhang, Wenjie Shang, Siyuan Chen, Qihang Xu and Zhenghao Lin for their useful help.

In addition, special thanks to my academic advisor Dr. David Peters for academic advice.

Finally, I would like to thank everyone who interfaced with me during the period of my Master's study at Washington University in St. Louis. This memory will accompany me forever.

Rong Zou

Washington University in St. Louis

May 2020

Dedication

I would like to dedicate this thesis to my father (Wenzhong Zou) and my mother (Hongxiu Zhang) for their unconditional support.

I will never succeed without their support, influence and encouragement.

Potential of Hydrodynamic Metamaterial Cloak for Drag Reduction

Rong Zou

Master of Science in Mechanical Engineering

Washington University in St. Louis, May 2020

Research Advisor: Professor Ramesh K. Agarwal

Abstract

Metamaterials are rationally designed artificial materials composed of tailored functional building blocks densely packed into an effective material. While metamaterials historically are primarily thought to be associated with negative index of refraction and invisibility cloaking in electromagnetism or optics, it turns out that the simple metamaterial concept also applies to many other areas of physics namely the thermodynamics, classical mechanics including elastostatics, acoustics, fluid dynamics and elastodynamics, and in principle also to the quantum mechanics. The goal of this thesis is to introduce and evaluate the potential of a hydrodynamic metamaterial cloak for drag reduction of objects in viscous flow. In recent years, the hydrodynamic metamaterial cloak has been created in very low Reynolds number Stokes flow by changing the viscosity tensor distribution in the cloak around the object. In practice, the spatially varying viscosity distribution is achieved by introducing a large number of micro-pillars in the cloak domain. In this thesis, the hydrodynamic cloaks for 2D objects of complex shapes such as airfoil are created by coordinate transformation using the Stokes equations for low Reynolds number flows. First, the viscosity tensor for a circular cylinder cloak is derived by coordinate transformation based on the Stokes equations. Then the viscosity tensors for an elliptic-cylinder cloak and an airfoil cloak are obtained by stretching the circular cylinder cloak. The effect of the

cloaks is simulated using the commercially available software ANSYS FLUENT 2019R2. The unstructured meshes for all cases are generated by the software ICEM. By comparing the velocity fields, pressure fields, streamlines and wall skin friction coefficient in flow about various geometries without and with cloak, the potential of a hydrodynamic metamaterial cloak for drag reduction is evaluated. The cloak changes the velocity field and pressure field in the cloak region such that the velocity distribution in the region outside the cloak becomes more uniform, and the pressure difference between the upstream and downstream regions of the object becomes smaller; this produces the hydrodynamic hiding effect and drag reduction. These effects are reduced at higher Reynolds numbers. The results for a cloak around a circular cylinder, an elliptic-cylinder, an airfoil and a flat plate (normal to the flow) show that a hydrodynamic cloak has the effect of hiding the object and reduces the drag, although these effects are reduced at high Reynolds numbers.

Chapter 1: Introduction

1.1 Brief Literature Review

Fluid drag plays an important role in scientific and engineering applications. Drag reduction technology can bring a breakthrough to the fluid mechanics industry [1]. The metamaterial cloak is a microfabricated structure which is obtained by using a coordinate transformation method analogous to transformation optics to get specific mapping of the material properties. The method of using a metamaterial cloak to hide an object in an electromagnetic field was first used in electromagnetism and optics [2,3], and later in thermodynamics [4,5], acoustics [6,7], solid mechanics[8,9], and porous media fluid flow [10,11]. The application of the metamaterial cloak in hydrodynamics provides a new possibility for fluid drag reduction.

In recent years, the study of the application of a hydrodynamic metamaterial cloak has gradually gained attention. Urzhumov et. al proposed that the mapping of viscosity can be achieved by using the coordinate transformation based on Darcy's pressure equation and Brinkman-Stokes equation [10]. They reported that an anisotropic mapping of permeability tensor enables the cloaking of the flow in a porous media and theoretically proposed active hydrodynamic metamaterials with negative permeability to achieve the fluidic cloaking [11,12]. Park et. al proposed a method to derive a viscosity tensor based on the invariant form of Navier-Stokes equations at low Reynolds number by using coordinate transformation of fluidic space [13]. They achieved the hydrodynamic hiding of a circular cylinder surrounded by a cloak and showed excellent drag reduction effect of the cloak in the numerical simulation. They verified the simulation results against the experiments of the flow in a tunnel model with micro-pillars. However, only one case of a circular cylinder cloak was considered in their work. To understand

the working principles of a hydrodynamic metamaterial cloak and explore its application, more investigations are needed.

1.2 Scope of the Thesis

The goal of this thesis is to understand the drag reduction effect and the hydrodynamic hiding effect of hydrodynamic metamaterial (HDMM) cloaks. This thesis addresses two problems: (1) study of the working principle of a HDMM cloak and (2) proposition and evaluation of a feasible method to create HDMM cloaks for objects of various shapes.

The working principle of a HDMM cloak is studied by conducting the simulation of the flow around a circular cylinder surrounded by a HDMM cloak at Reynolds numbers from 1.5 to 150. By comparing the velocity fields, pressure fields, streamlines and wall skin friction coefficient on the object in the flow around the cylinder without and with cloak, the hydrodynamic hiding effect and drag reduction effect of the cloak are analyzed.

The HDMM cloaks for objects of various shapes, including elliptic-cylinder, vertical flat plate and airfoil, are created based on the result of the circular cylinder cases at various Reynolds numbers. The cloaks for these objects are obtained by stretching the cloak for a circular cylinder based on the geometric relationship. The effects of the cloaks for these shapes are evaluated by comparing the flow fields with cloak and without cloak.

Chapter 2: HDMM Cloak for a Circular Cylinder

2.1 Modeling of HDMM Cloak for a Circular Cylinder

2.1.1 Hydrodynamic Coordinate Transformation

The basic idea of generating HDMM cloak is coordinate transformation analogous to that used in transformation optics or acoustics for cloaking. The coordinate transformation between two systems can be presented as a Jacobi matrix Λ. By denoting the position vector in the old system as p^i and in the new system as p'^j, the Jacobian matrix is given by:

$$\Lambda = \frac{\partial p'^j}{\partial p^i} \tag{1}$$

In the cloaking phenomenon, the space is affected by the cloak and is distorted such that it hides the object to the observer. The cloaking space in the observer's view becomes the virtual space [13]. The original space which has distorted field parameters is the physical space. Let p^i and q^k be the position vectors in the Cartesian coordinate system and the orthogonal coordinate system respectively in the virtual space, and $p'^j$and q'^l be the position vectors in the Cartesian coordinate system and the orthogonal coordinate system respectively in the physical space. The Jacobian matrix connecting these two spaces in the two coordinate systems becomes:

$$\Lambda = \frac{\partial p'^j}{\partial p^i} = \frac{\partial p'^j}{\partial q^l}\frac{\partial q'^l}{\partial q^k}\frac{\partial q^k}{\partial p^i} = B'^{-1}\lambda B \tag{2}$$

where λ is the Jacobian matrix between the two orthogonal coordinate systems and B is the Jacobian matrix between the orthogonal system and the Cartesian coordinate system.

The research on hiding objects in a field using the coordinate transformation started in transformation optics. Chen et. al achieved the hiding or cloaking of objects through coordinate

transformation governed by Maxwell's equations [14]. In fluid dynamics problems, the coordinate transformation is required for the Navier-Stokes equations which consist of a continuity equation and a momentum equation. These equations are given as:

$$\frac{\partial \rho}{\partial t} + \nabla \cdot (\rho \tilde{u}) = 0 \tag{3}$$

$$\rho\left(\frac{\partial \tilde{u}}{\partial t} + \tilde{u} \cdot \nabla \tilde{u}\right) = \nabla \cdot \left(\tilde{\tilde{\tau}} - p\tilde{\tilde{\delta}}\right) + \rho \tilde{g} \tag{4}$$

where ∇ is the del operator, ρ is the density of the fluid, $\tilde{u}$ is the velocity field in the flow, $\tilde{\tilde{\tau}}$ is the viscous stress tensor, p is the static pressure, $\tilde{\tilde{\delta}}$ is the identity tensor, and $\tilde{g}$ is the body acceleration. By assuming steady incompressible low Reynolds flow and neglecting the body acceleration, Navier-Stokes equations can be simplified as:

$$\nabla \cdot \tilde{u} = 0 \tag{5}$$

$$\nabla \cdot \tilde{\tilde{\tau}} = \nabla p \tag{6}$$

The viscous stress tensor can be expressed as $\tilde{\tilde{\tau}} = \mu(\nabla \tilde{u} + \nabla \tilde{u}^T)$ where μ is the viscosity of the fluid. Unlike the Maxwell's equation used in transformation optics, the momentum equation is Navier-Stokes equations contains a divergence term $\nabla \cdot \tilde{\tilde{\tau}}$. Therefore, the coordinate transformation of the divergence of the stress tensor needs to be derived. Park et. al presented the derivation process [13]. By the divergence theorem, $\tilde{\tilde{\tau}}\left(= \tau^{ij} x_i x_j\right)$ can be defined as follows.

$$\iint_s \tilde{\tilde{\tau}} \cdot d\tilde{s} = \iiint_v \nabla \cdot \tilde{\tilde{\tau}} dV \tag{7}$$

The above equation can be transformed to the new coordinate system $\left(\tau^{\tilde{\tilde{\prime}}} = \tau'^{ij} x'_i x'_j\right)$ as follows.

$$\iint_s \tilde{\tilde{\tau}} \cdot d\tilde{s} = dp'^3 \frac{\partial}{\partial p'^3}[\tilde{\tilde{\tau}} \cdot (\tilde{x}'_1 \partial p'^1 \times \tilde{x}'_1 \partial p'^2)] + dp'^1 \frac{\partial}{\partial p'^1}[\tilde{\tilde{\tau}} \cdot (\tilde{x}'_2 \partial p'^1 \times \tilde{x}'_3 \partial p'^2)]$$

$$+dp'^2\frac{\partial}{\partial p'^2}[\tilde{\tilde{\tau}}\cdot(\tilde{x}'_3\partial p'^1\times\tilde{x}'_3\partial p'^1)]$$

$$=\nabla\cdot\tilde{\tilde{\tau}}'\partial p'^1\partial p'^2\partial p'^3 \tag{8}$$

$$\iiint_v\nabla\cdot\tilde{\tilde{\tau}}dV=\tilde{x}'_1\,dp'^1\cdot(\tilde{x}'_2dp'^2\times\tilde{x}'_3dp'^3)\nabla\cdot\tilde{\tilde{\tau}}$$

$$=\nabla\cdot\tilde{\tilde{\tau}}\,det(\Lambda^{-1})\,\partial p'^1\partial p'^2\partial p'^3 \tag{9}$$

From Eqs. (8) and Eqs. (9), the following relationship is derived:

$$\nabla\cdot\tilde{\tilde{\tau}}=(det(\Lambda)\,\Lambda^{-1})\nabla'\cdot\tilde{\tilde{\tau}}' \tag{10}$$

where $\nabla=\Lambda^{-1}\nabla'$. Therefore, the following relationships are derived.

$$\nabla'\cdot\tilde{\tilde{\tau}}'=det(\Lambda^{-1})\,\Lambda\nabla\cdot\tilde{\tilde{\tau}}=det(\Lambda^{-1})\,\Lambda\Lambda^T\nabla'p \tag{11}$$

$$\nabla p=\Lambda^T\nabla'p \tag{12}$$

$$\tilde{u}'=det(\Lambda)\,\Lambda^{-1}\tilde{u} \tag{13}$$

$$\nabla'\cdot\tilde{\tilde{\tau}}=\nabla'\cdot\mu\left(\nabla'^{\tilde{u}'}+\nabla'^{\tilde{u}'^T}\right) \tag{14}$$

where $\tilde{\tilde{\tau}}'=det(\Lambda^{-1})\,\Lambda\tilde{\tilde{\tau}}\Lambda^T$. Hence, the transformation of viscosity can be derived as follows.

$$\nabla'\cdot\mu\left(\nabla'^{\tilde{u}'}+\nabla'^{\tilde{u}'^T}\right)=det(\Lambda^{-1})\,\Lambda\Lambda^T\nabla'p \tag{15}$$

$$\nabla'\cdot\left(det(\Lambda)\,\Lambda^{-1}\mu\Lambda^{-T}\left(\nabla'^{\tilde{u}'}+\nabla'^{\tilde{u}'^T}\right)\right)=\nabla'p \tag{16}$$

$$\nabla'\cdot\left(\tilde{\tilde{\mu}}'\left(\nabla'^{\tilde{u}'}+\nabla'^{\tilde{u}'^T}\right)\right)=\nabla'p \tag{17}$$

where $\tilde{\tilde{\mu}}'$ is the viscosity tensor expressed as $\tilde{\tilde{\mu}}'=det(\Lambda)\,\Lambda^{-1}\mu\Lambda^{-T}$.

2.1.2 Viscosity Tensor for a Circular Cylinder Cloak

The coordinate transformation from the virtual space to the physical space for a circular cylinder cloak includes three steps: (1) from the Cartesian coordinate system to the polar coordinate system in the physical space, (2) from the polar coordinate system in the physical space to the polar coordinate system in the virtual space, and (3) from the polar coordinate

system to the Cartesian coordinate system in the virtual space. These coordinate systems are shown in Figure 1. The position vectors for these four systems are p'^j, q'^l, q^k and p^i.

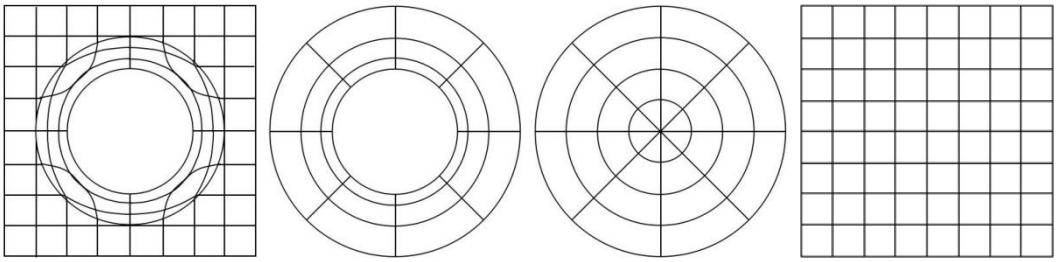

(a) (b) (c) (d)

(a) The Cartesian coordinate system in the physical space, (b) The polar coordinate system in the physical space, (c) The polar coordinate system in the virtual space, and (d) The Cartesian coordinate system in the virtual space.

Figure 1. Coordinate systems and coordinate transformations in physical and virtual space

In the Figure 1(a) and Figure 1(b), the inner and outer circles are the boundaries of the cylinder cloak and their radii are a and b. The effect of the cloak is to compress the fluid space from a circular region ($0 < r < b$) into an annular region ($a < r' < b$) by changing the viscosity tensor distribution in the cloaking region. The space in the region ($0 < r' < a$) is occupied by a circular cylinder whose radius is a. The relationships between these two spaces are as follows.

$$r' = \left(\frac{b-a}{b}\right) r + a \tag{18}$$

$$\theta' = \theta \tag{19}$$

The Jacobian matrices for the transformation between the two polar coordinate systems ($\lambda: q'^l \to q^k$) and between the polar coordinate system and the Cartesian coordinate system ($B: q^k \to p^i$) are as follows.

$$\lambda = \begin{bmatrix} \frac{\partial r'}{\partial r} & \frac{\partial r'}{\partial \theta} \\ \frac{\partial \theta'}{\partial r} & \frac{\partial \theta'}{\partial \theta} \end{bmatrix} = \begin{bmatrix} \frac{b-a}{b} & 0 \\ 0 & 1 \end{bmatrix} \tag{20}$$

$$B = \begin{bmatrix} \frac{\partial r}{\partial x} & \frac{\partial r}{\partial y} \\ \frac{\partial \theta}{\partial x} & \frac{\partial \theta}{\partial y} \end{bmatrix} = \begin{bmatrix} cos\,\theta & sin\,\theta \\ -\frac{sin\,\theta}{r} & \frac{cos\,\theta}{r} \end{bmatrix} \tag{21}$$

Consequently, the Jacobian matrix for the circular cylinder cloak ($\Lambda: p'^j \rightarrow p^i$) and its determinant are obtained as follows.

$$\Lambda = B'^{-1}\lambda B = \begin{bmatrix} \frac{b-a}{b} & 0 \\ 0 & \frac{r'}{r} \end{bmatrix} = \begin{bmatrix} \frac{b-a}{b} & 0 \\ 0 & \frac{r'}{r'-a}\frac{b-a}{b} \end{bmatrix} \tag{22}$$

$$det(\Lambda) = \left(\frac{b-a}{b}\right)^2 \left(\frac{r'}{r'-a}\right) \tag{23}$$

Thus, the expression for the viscosity tensor for the circular cylinder cloak is obtained as:

$$\tilde{\tilde{\mu}}' = \begin{bmatrix} \mu'_{rr} & \mu'_{r\theta} \\ \mu'_{\theta r} & \mu'_{\theta\theta} \end{bmatrix} = \begin{bmatrix} \frac{r'}{r'-a} & 0 \\ 0 & \frac{r'-a}{r'} \end{bmatrix} \mu \tag{24}$$

In the viscosity tensor above, the value at $r' = a$ and $r' = 0$ goes to infinity. Schittny et. al [4] and Schurig et. al [15] have presented a reduced set of the material properties calculated by multiplying the value by $det(\Lambda)$ in their study. A factor c should be multiplied to the viscosity tensor to resolve the mismatch at the outer boundary according to the study of Schurig et. al [15] and Stenger et. al [16]. The final viscosity tensor expression is as follows.

$$\tilde{\tilde{\mu}}'' = \begin{bmatrix} \mu''_{rr} & \mu''_{r\theta} \\ \mu''_{\theta r} & \mu''_{\theta\theta} \end{bmatrix} = c \begin{bmatrix} \left(\frac{b-a}{b}\right)^2 \left(\frac{r'}{r'-a}\right)^2 & 0 \\ 0 & \left(\frac{b-a}{b}\right)^2 \end{bmatrix} \mu \tag{25}$$

2.2 Simulation Model for a Circular Cylinder Cloak

The simulation model is a 10mm*10mm*50μm channel with a circular cylinder as shown in Figure 2. Figure 2(b) shows the top view of the simulation model. The HDMM cloak surrounds the cylinder. The radius of the cylinder (a) is 2mm. The radius of the cloaking region (b) is 4mm.

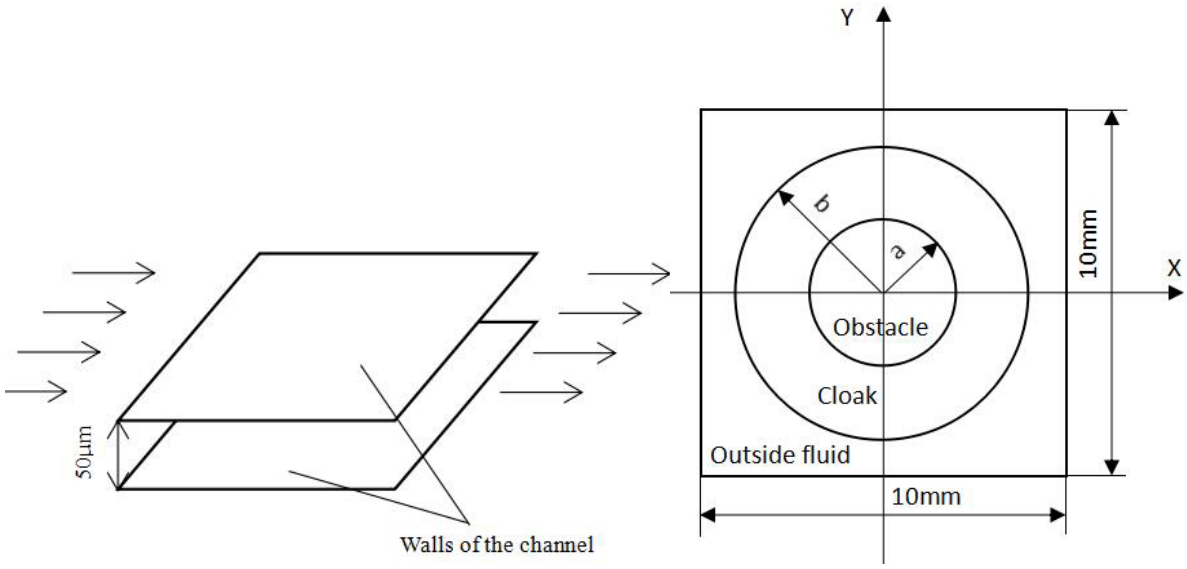

(a) Simulation model (b) Top view of the model

Figure 2. Simulation model of the circular cylinder with a cloak

Because the channel and the cylinder are very thin compared to their length and width, the simulation domain can be modeled as a 2D domain to reduce the difficulty of meshing and calculation. The variables in the field, such as velocity and pressure, are represented by their average value along *z*-axis. To keep the correct relationship among all the variables during the transformation from a 50μm thick channel to a 2D square domain, a source term is added in the governing equations. The relationship between pressure drop and the average velocity in a laminar channel flow is derived from Poiseuille equation written as follows.

$$-\frac{\Delta P}{\Delta x} = \frac{8\mu V_{bare}}{t^2} \tag{26}$$

where V_{bare} is the theoretical average velocity in the bare channel without the object, $\Delta P/\Delta x$ is the pressure drop per unit length, and t is the height of the channel. In ANSYS FLUENT, the fluid area can be defined as a porous zone which will add a source term in the momentum governing equation. That source term provides an additional pressure drop as follows.

$$-\Delta P = av^2 + bv,\ a = C_2\frac{1}{2}\rho\Delta x,\ b = \frac{\mu}{\alpha}\Delta x \tag{27}$$

where inertia resistance (C_2) and viscous resistance $(1/\alpha)$ are defined by users. Thus, the properties of the porous zone are as follows.

$$\frac{1}{\alpha} = \frac{8\mu}{t^2\mu} = \frac{8}{50\mu m^2} = 3.2\times 10^9\left[\frac{1}{m^2}\right],\ \ C_2 = 0 \tag{28}$$

To verify the method of simplifying a thin channel as a 2D domain, a validation simulation is conducted. Figure 3 shows an example of using a porous zone to simplify a channel flow which the channel is the same channel shown in Figure 2 but without the cylinder and the cloak. The left side is the pressure inlet. The right side is the pressure outlet. The upper and lower sides are symmetry boundary conditions. The inlet pressure is 1kPa and the outlet pressure is 0. The fluid is water where viscosity is 0.001003Pa*s. Figure 3(a) shows the uniform pressure drop which is 100kPa/m. The velocity in Figure 3(b) is 31.25mm/s in the whole domain. Both values match the theoretical values calculated by the Poiseuille equation. Therefore, the method of modeling a 3D thin channel as a 2D domain by defining the domain as a porous zone is feasible and is used in all simulation cases in this thesis.

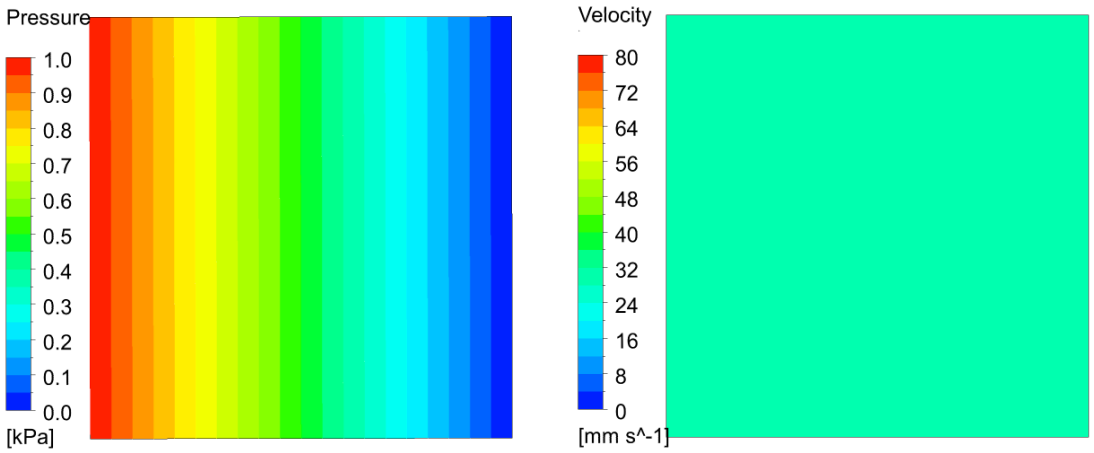

(a) Pressure contours (b) Velocity contours

Figure 3. Validation of the simplification of a laminar narrow channel flow model to a 2D porous zone model

The unstructured mesh for the simulation model in Figure 2(b) is generated in ICEM. The meshes in the cloak region and the outside the cloak region are generated separately and are merged. The outer boundary of the cloak region and the inner boundary of the region outside the cloak are defined as an interface and are matched automatically in ANSYS FLUENT to eliminate the error. The total number of cells is 260000. The boundary conditions are shown in Figure 4.

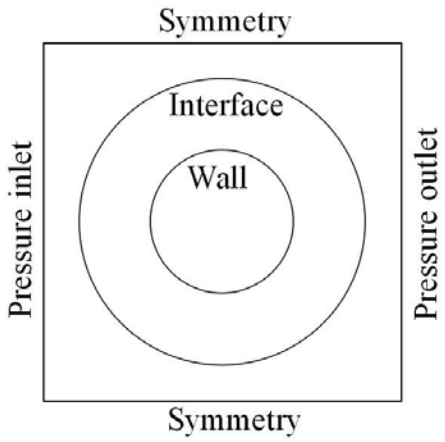

Figure 4. Boundary conditions of the cylinder cloak model

The fluid material for the entire domain is water where density is $\rho = 998.2kg/m^3$ and viscosity is $\mu = 0.001003kg/(m \cdot s)$. The surface of the cylinder is set as a no-slip stationary wall. The outlet pressure outlet is 0. The gauge pressure at the pressure inlet (P) is 1kPa, 10kPa and 100kPa for three cases considered. The relationships among the inlet pressure, the theoretical velocity in the bare channel (V_{bare}) calculated by Poiseuille equation and the Reynolds numbers are shown in Table 1. The Reynolds number is calculated as follows.

$$Re = \frac{\rho V_{bare} t}{\mu} \tag{29}$$

Table 1. Inlet pressure, theoretical velocity in the bare channel and Reynolds numbers for the circular cylinder cloak

Inlet Pressure (kPa)	V_{bare} (mm/s)	Re
1	31.25	1.5
10	312.5	15
100	3125	150

Based on the simplification of the simulation model discussed above, the region outside the cloak is modeled as a porous zone ($1/\alpha = 3.2 \times 10^9 [1/m^2]$, $C_2 = 0$). The cloak region is also modeled as a porous zone, but the properties are different because of the viscosity tensor. In the cloak region, the viscosity value used in Poiseuille equation and FLUENT source term expression are different. The viscosity in Poiseuille equation is the viscosity tensor derived from coordinate transformation ($\tilde{\tilde{\mu}}''$), but FLUENT uses the value from the material database (μ) in the expression of the source term. Hence, the porous zone properties expressions are modified as:

$$\frac{1}{\alpha} = \frac{8\tilde{\tilde{\mu}}''}{t^2\mu} = \frac{8}{50\mu m^2} c \begin{bmatrix} \left(\frac{b-a}{a}\right)^2 \left(\frac{r'}{r'-a}\right)^2 & 0 \\ 0 & \left(\frac{b-a}{a}\right)^2 \end{bmatrix}, \; C_2 = 0 \tag{30}$$

The viscous resistance can be separated by directions. The normal viscous resistance is $1/\alpha_r$ and the tangential viscous resistance is $1/\alpha_\theta$. In this model, $a = 2mm$ and $b = 4mm$. Therefore, the viscous resistance can be expressed as follows.

$$\frac{1}{\alpha_r} = 3.2 \times 10^9 \times \frac{1}{4} c \left(\frac{r'}{r' - 2mm}\right)^2 \left[\frac{1}{m^2}\right]$$

$$\frac{1}{\alpha_\theta} = 3.2 \times 10^9 \times \frac{1}{4} c \, [1/m^2]$$

where c is set as 1.5 for the cylinder cases with cloak according to the study of Schurig et. al [15] and Stenger et. al [16].

Laminar flow model is selected for simulation. SIMPLEC scheme for steady solver is used as pressure-velocity coupling method. Second order discretization for pressure, momentum and energy is selected for the solution algorithm. The double precision solver in ANSYS FLUENT is used to perform the numerical simulations. The convergence criterion is 0.00001. A comparison case without the cloak is conducted for every case. The comparison case has the same simulation models and the boundary conditions but the porous zone properties in the cloak region are set as the same value as in the region outside the cloak so that the cloaking will not be included.

2.3 Evaluation of the Effect of the HDMM Cloak on a Circular Cylinder

2.3.1 Evaluation of Hydrodynamic Hiding Effect

One main effect of a HDMM cloak is the hydrodynamic hiding of the internal object. To evaluate the hydrodynamic hiding effect of the circular cylinder HDMM cloak, the velocity distribution and streamlines are analyzed.

Figure 5 shows the velocity fields around the circular cylinder without cloak and with cloak at various Reynolds numbers. The velocity field is symmetric along x and y axes at Re=1.5

shown in Figure 5(a). Affected by the cloak, the high velocity areas move from the upper and lower surfaces of the cylinder to the sides of the interface in the cloak region, and the low velocity areas are contracted near the leading edge and the trailing edge. This velocity distribution is caused by the viscosity tensor in the cloak region. Because the normal viscosity is larger near the cylinder and larger than the tangential viscosity, the flow avoids the cylinder actively in the cloak region. When Re increases, the high velocity areas move to downstream and cross the interface as Figure 5(b) and Figure 5(c).

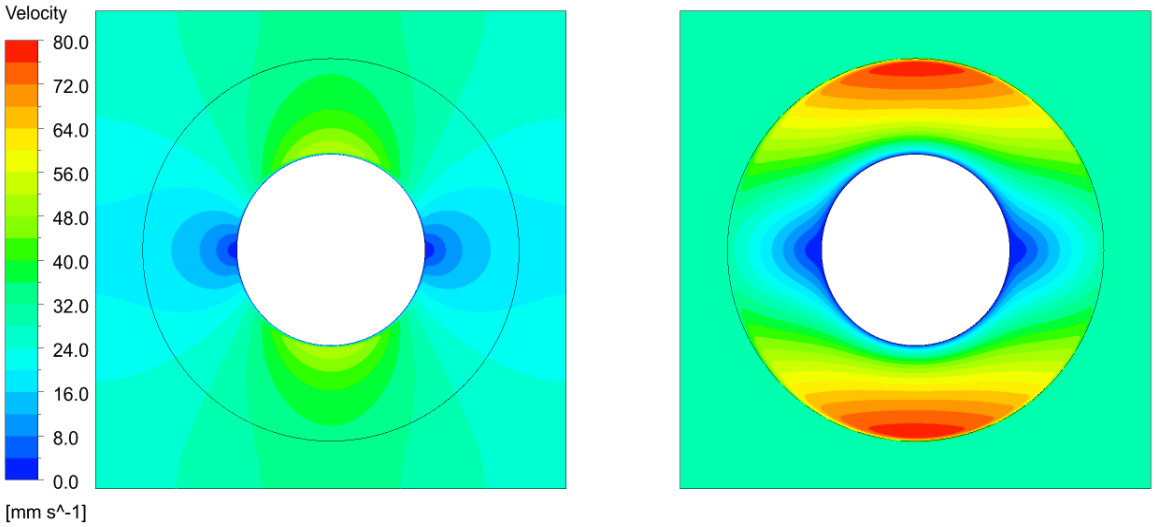

(a) The case without cloak (left) and the case with cloak (right) at Re=1.5

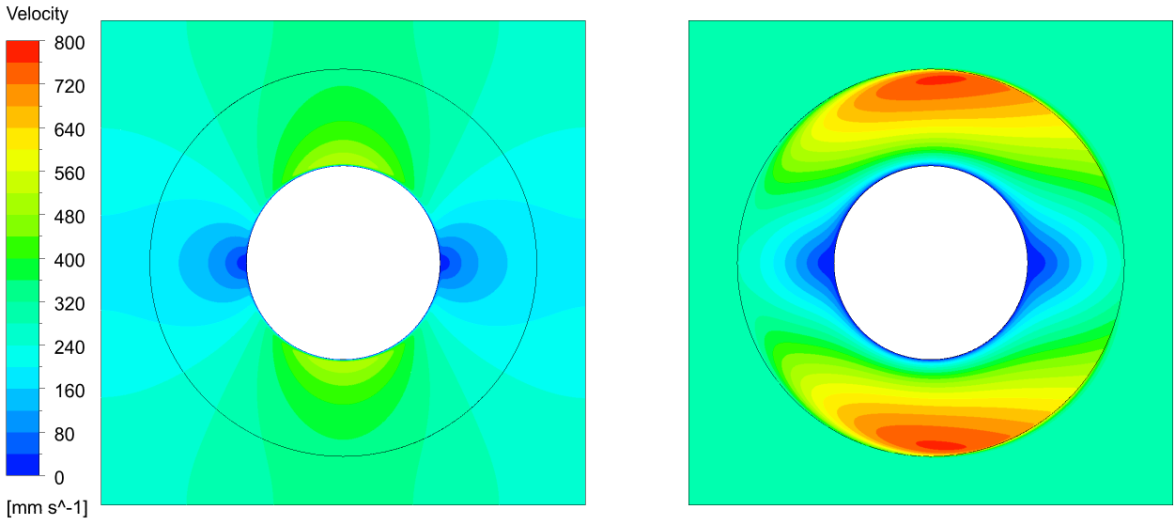

(b) The case without cloak (left) and the case with cloak (right) at Re=15

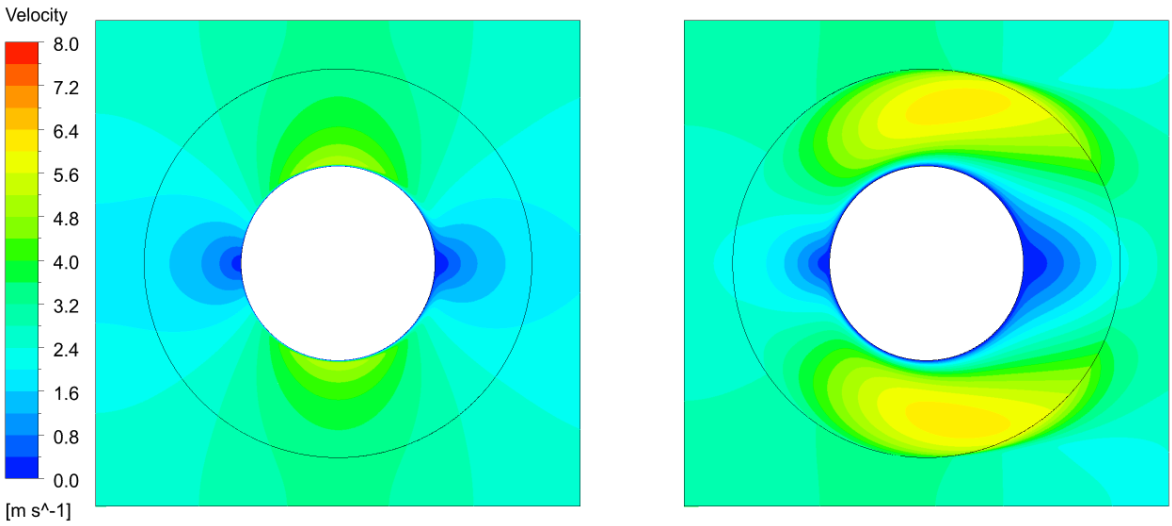

(c) The case without cloak (left) and the case with cloak (right) at Re=150

Figure 5. Velocity fields around the circular cylinder without cloak and with cloak at various Reynolds numbers

Figure 6 shows the velocity fields in the region outside the cloak for the circular cylinder. The velocity distribution varies from 18mm/s to 42mm/s without cloak and varies from 30.75mm/s to 31.75mm/s with cloak which is highly uniform in the region outside the cloak at Re=1.5 as shown in Figure 6(a). This range of velocity is very close to the theoretical velocity in

the bare channel (31.25mm/s). When Re increases to 15 and 150, the velocity distribution changes significantly in the cases with cloak as shown in Figure 6(b) and Figure 6(c) for Re=15 and Re=150 respectively.

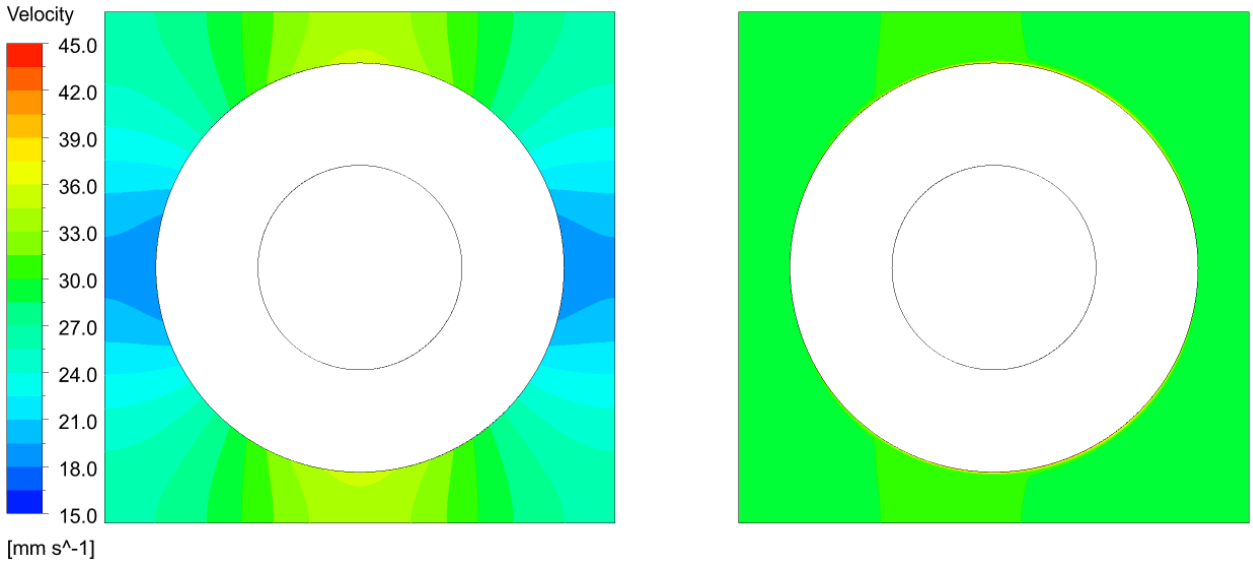

(a) The case without cloak (left) and the case with cloak (right) at Re=1.5

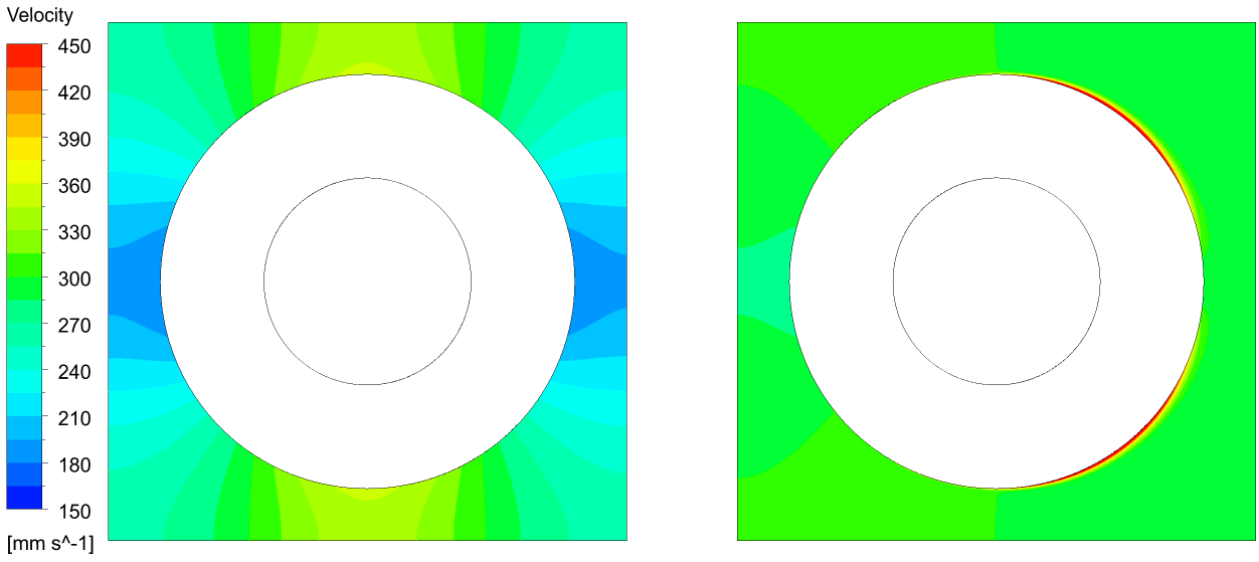

(b) The case without cloak (left) and the case with cloak (right) at Re=15

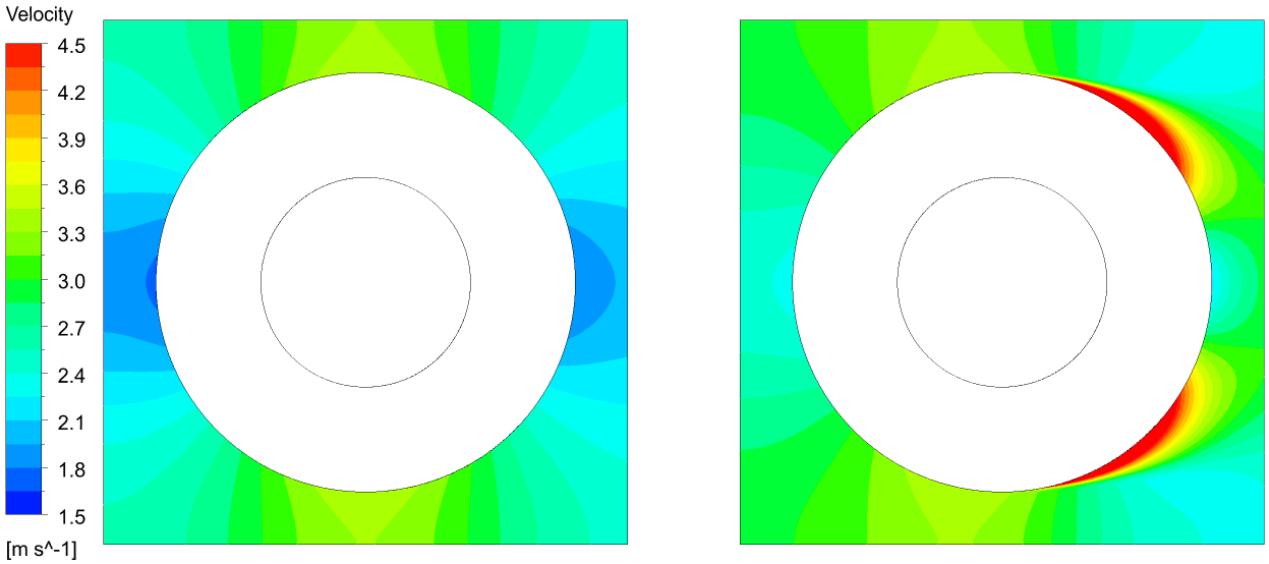

(c) The case without cloak (left) and the case with cloak (right) at Re=150

Figure 6. Velocity fields in the region outside the cloak for the circular cylinder without cloak and with cloak at various Reynolds numbers

Figure 7 shows the outlet velocity profiles for the circular cylinder cases. The cloak reduces the change in velocity caused by the cylinder compared to that without cloak, however the difference between the V_{bare} and velocity with cloak increases with the Reynolds number. In the cases without cloak, the velocity difference with V_{bare} is larger near the center line. In the cases with cloak, the outlet velocity is more uniform and is close to V_{bare} at Re=1.5 as shown in Figure 7(a). When Re increases, the outlet velocity is higher near the center line at Re=15 as shown in Figure 7(b) and shows a W-shaped curve at Re=150 as shown in Figure 7(c).

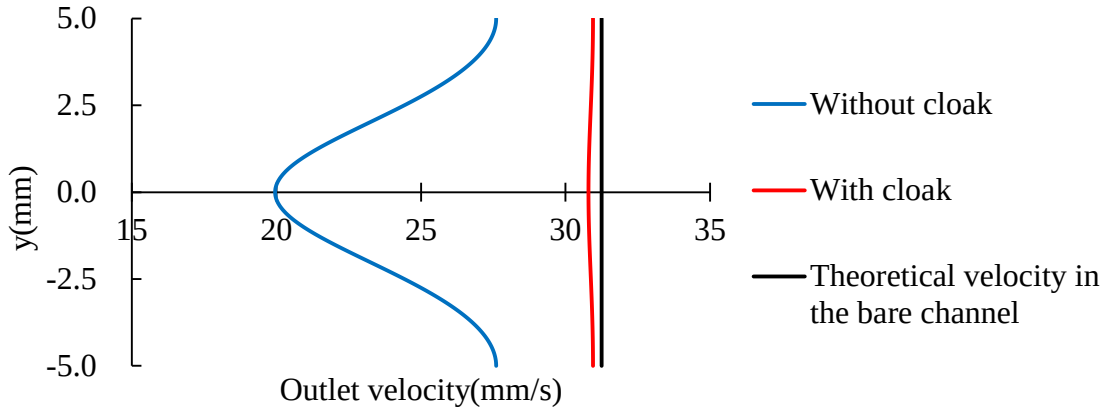

(a) Re=1.5

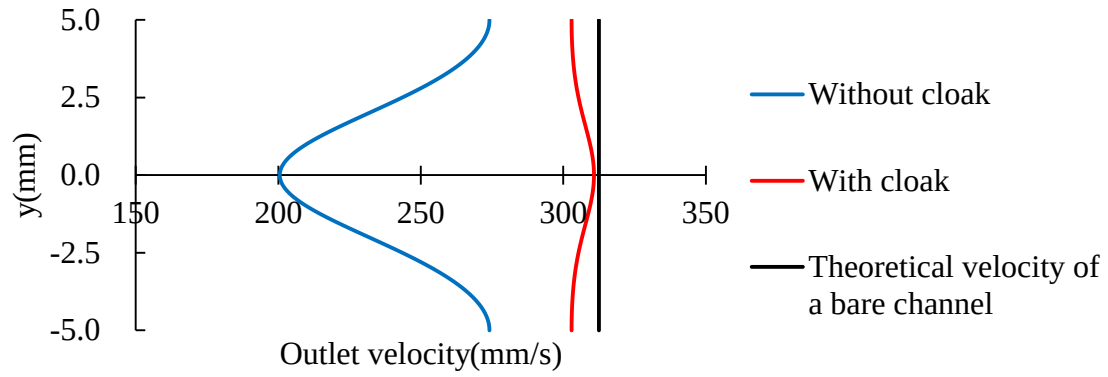

(b) Re=15

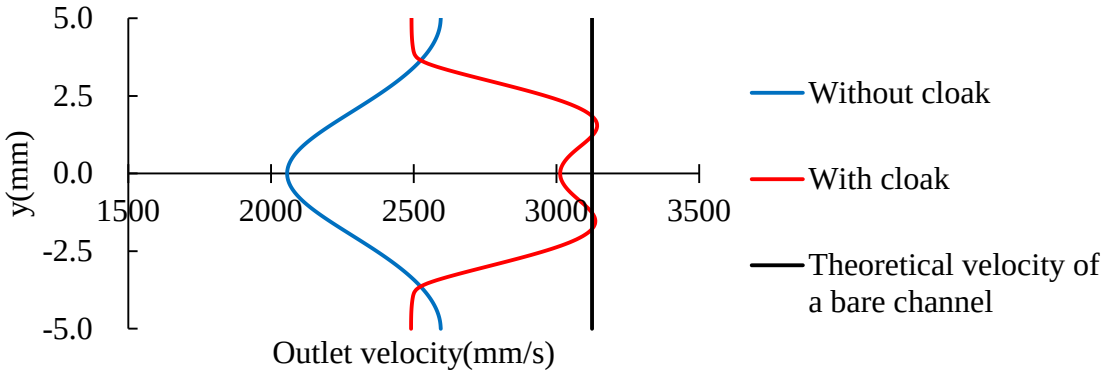

(c) Re=150

Figure 7. Comparison of outlet velocity profiles for circular cylinder without cloak and with cloak at various Reynolds numbers

The deviations in the outlet velocity (V_i) without cloak and with cloak relative to the theoretical velocity in the bare channel (V_{bare}) are calculated by Eqs. (31) respectively and the results are shown in Table 2.

$$Devation = \sqrt{\frac{\sum_{i=1}^{n}(V_i - V_{bare})^2}{N}} \tag{31}$$

where N is the number of grid points on the outlet. The deviation is reduced in all cases with cloak. But when Re increases from 1.5 to 150, the ratio of the reduction in deviation decreases from 20 to 2.

Table 2. Deviation in the outlet velocity without cloak and with cloak relative to the theoretical velocity in the bare channel for the circular cylinder at various Reynolds numbers

Re	V_{bare} (mm/s)	Deviation in Velocity with V_{bare} (mm/s)	
		Without Cloak	With Cloak
1.5	31.25	7.61	0.38
15	312.5	76.32	7.03
150	3125	797.32	389.41

Figure 8 shows the streamlines around the circular cylinder without cloak and with cloak at various Reynolds numbers. Affected by the cloak, the streamlines in the region outside the cloak become straighter in the cases of Re=1.5 and Re=15 as shown in Figure 8(a) and Figure 8(b) respectively. In the case of Re=150 with cloak, the streamlines are bent in the area x>0 as Figure 8(c).

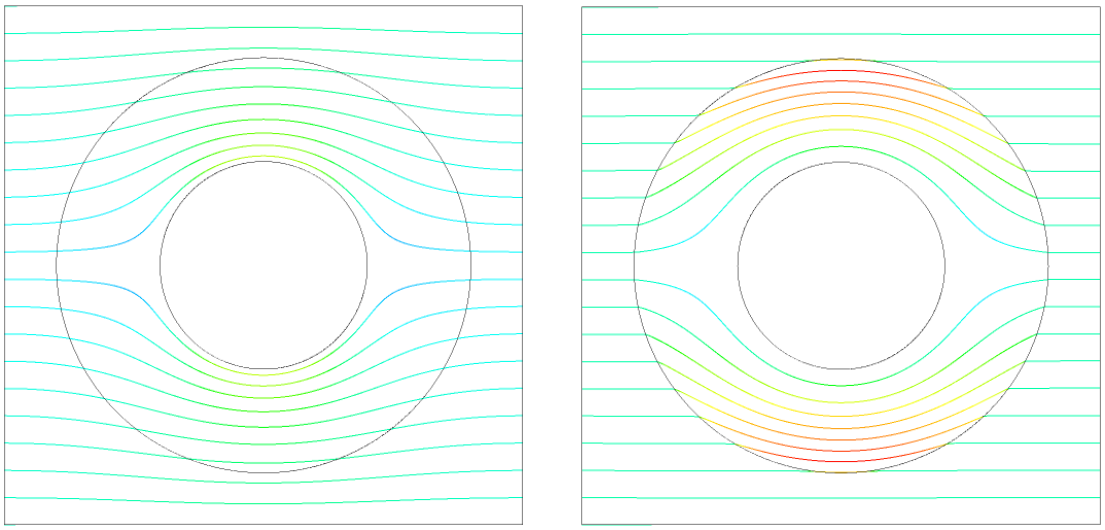

(a) The case without cloak (left) and the case with cloak (right) at Re=1.5

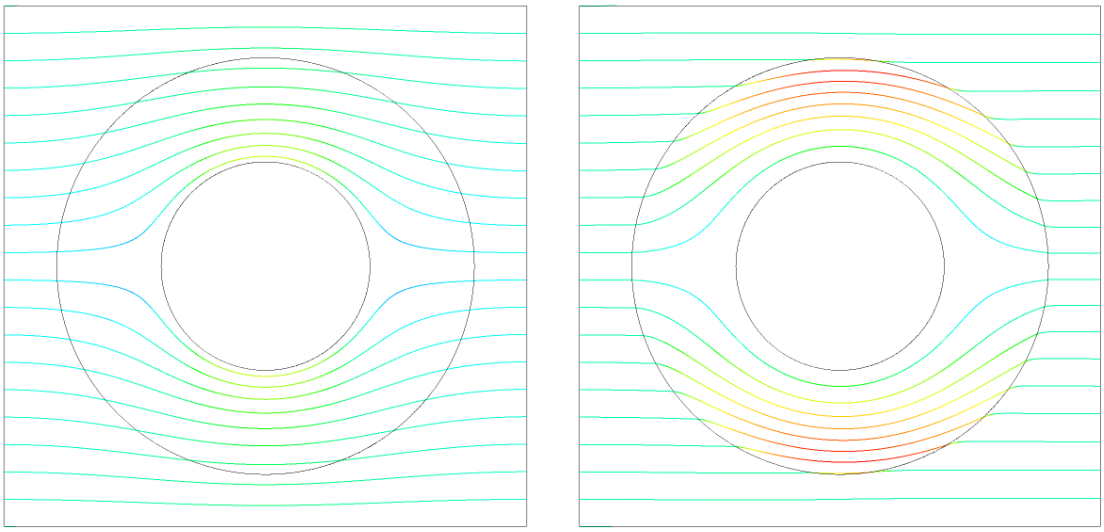

(b) The case without cloak (left) and the case with cloak (right) at Re=15

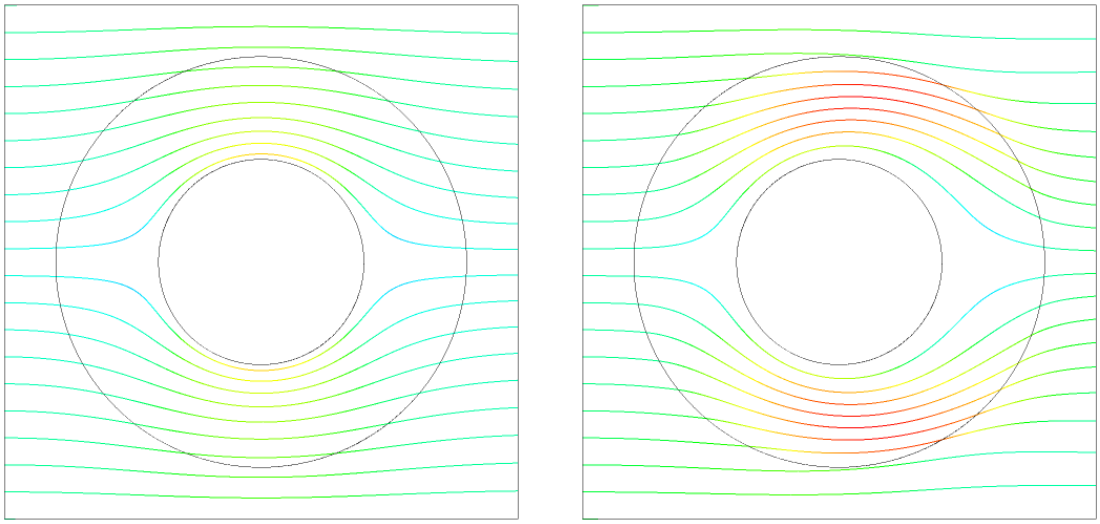

(c) The case without cloak (left) and the case with cloak (right) at Re=150

Figure 8. Streamlines around the circular cylinder without cloak and with cloak at various Reynolds numbers

Thus, the HDMM cloak has hydrodynamic hiding effect at Re from 1.5 to 150 by distorting the velocity fields, but this effect reduces with increase in Re significantly. The reason is that the viscosity tensor is derived from the simplified Navier-Stokes equations at low Reynolds number (Stokes equations). When Re is high, the effect of inertia force term in the momentum equation weakens the effect of the cloak.

2.3.2 Evaluation of Drag Reduction Effect

Figure 9 shows the pressure fields around the circular cylinder without cloak and with cloak at various Reynolds numbers. In the case of Re=1.5 without cloak, the pressure decreases from 0.85kPa at the leading edge to 0.15kPa at the trailing edge as shown in Figure 9(a). In the case with cloak, the pressure is about 0.5kPa at both the leading edge and the trailing edge. Thus, the pressure difference between the leading edge and the trailing edge is reduced significantly by the cloak. This reduction effect decreases at higher Re as shown in Figure 9(b) and Figure 9(c).

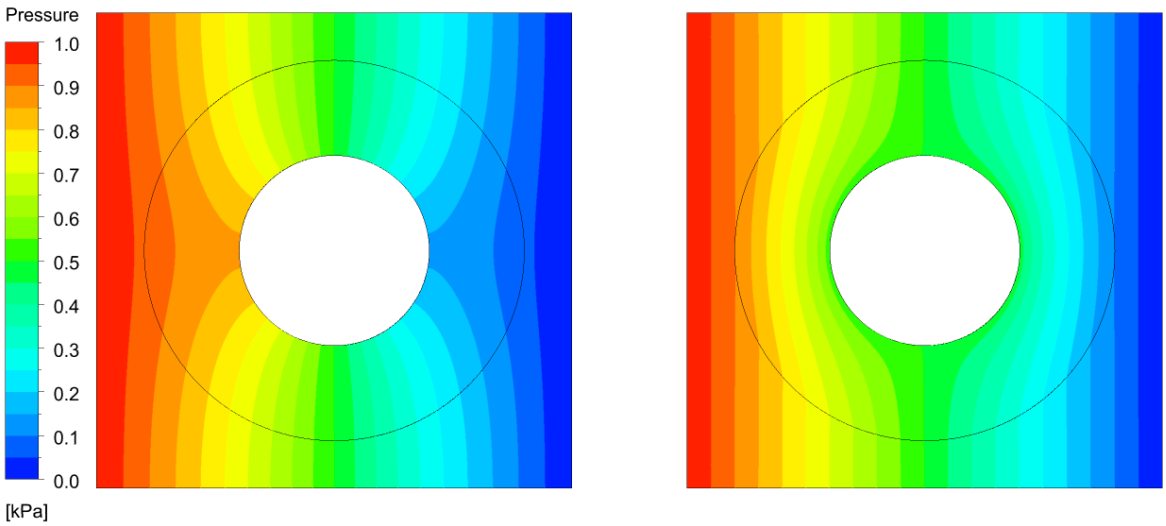

(a) The case without cloak (left) and the case with cloak (right) at Re=1.5

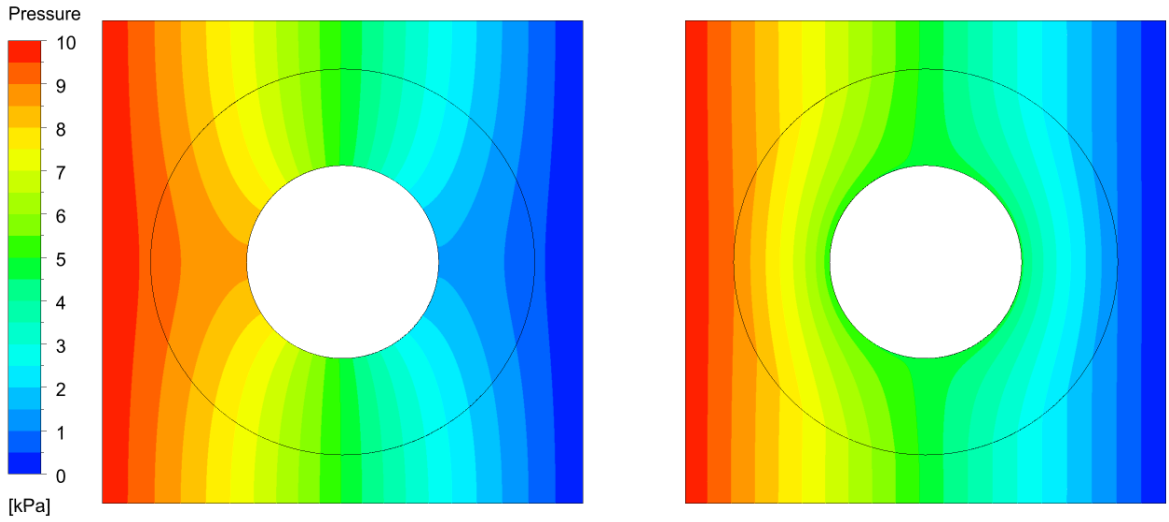

(b) The case without cloak (left) and the case with cloak (right) at Re=15

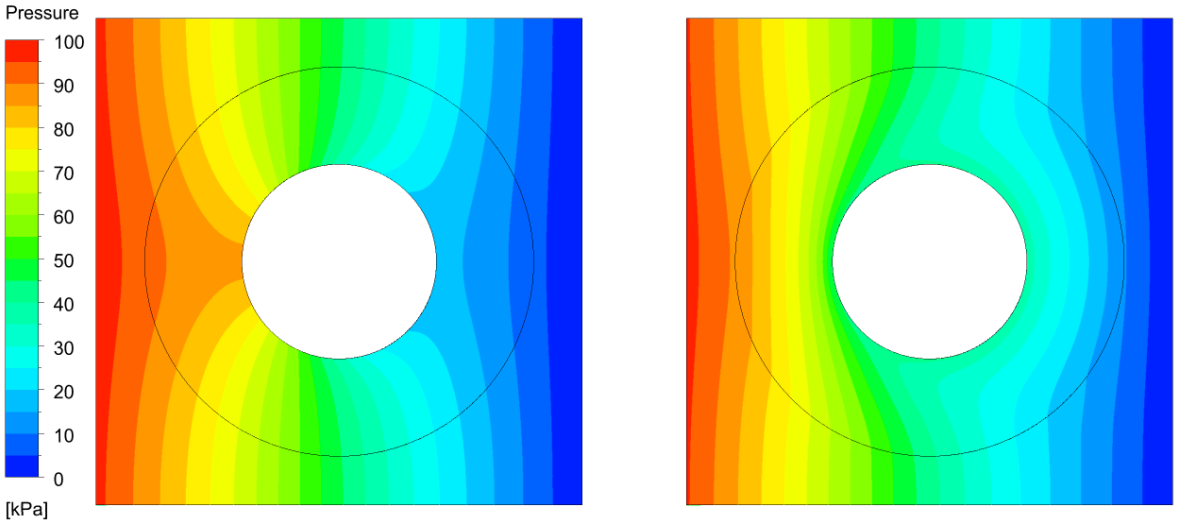

(c) The case without cloak (left) and the case with cloak (right) at Re=150

Figure 9. Pressure fields around the circular cylinder without cloak and with cloak at various Reynolds number

Figure 10 shows the wall skin friction coefficient (C_f) on the surface of the cylinder. The value of C_f on the upper surface and the lower surface are equal and overlapped in Figure 10. In all cases with cloak, C_f is about 20 times smaller than that in the cases without cloak and is almost 0 in the area near the upstream and downstream locations on the cylinder along the *x*-axis. There is asymmetry in the C_f distribution on the cylinder without cloak as the Reynolds number increases.

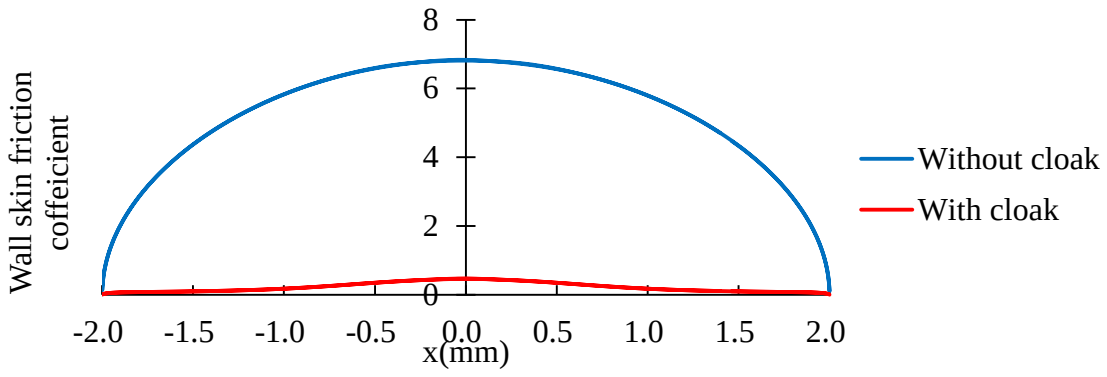

(a) Re=1.5

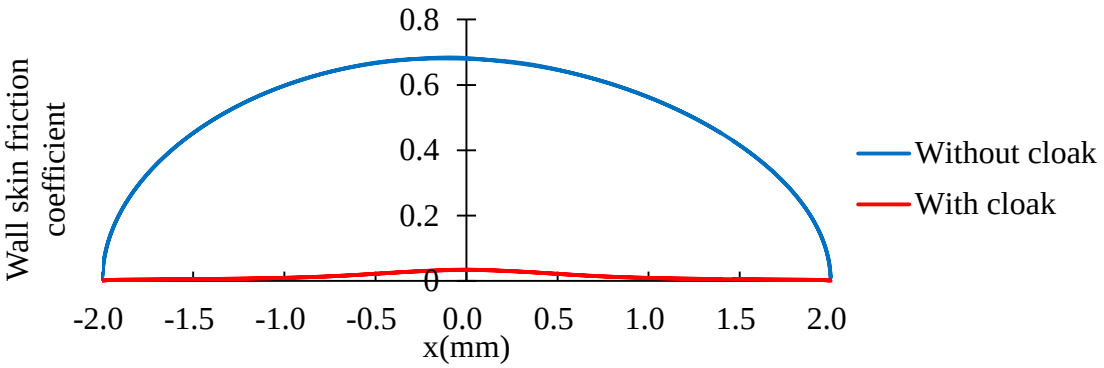

(b) Re=15

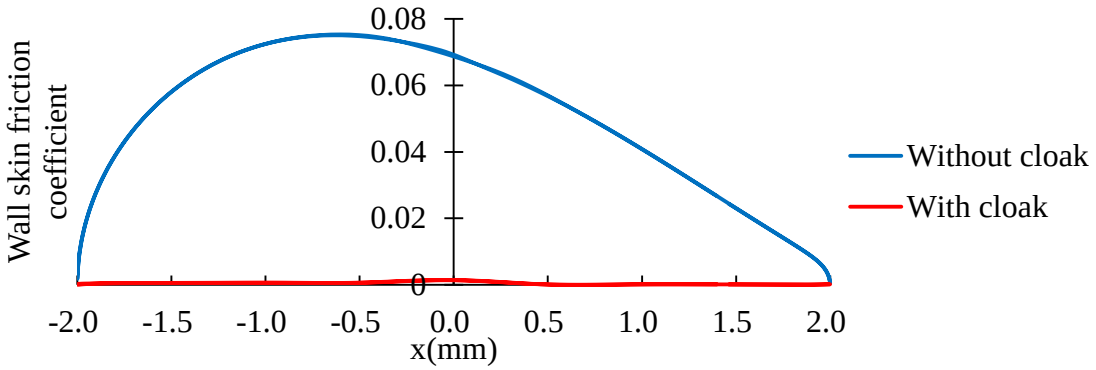

(c) Re=150

Figure 10. Wall skin friction coefficient on the surface of the cylinder without cloak and with cloak at various Reynolds numbers

Table 3 shows the drag force on the circular cylinder without cloak and with cloak at various Reynolds numbers. The majority of the drag force is the pressure force. The viscous force contributes only less than 0.8%. Affected by the cloak, the pressure force is reduced by 15 to 9 times and the viscous force is reduced by 25 to 107 times compared to that without cloak. As the Reynolds number increases in the cases with cloak, the pressure force increases 12 to 13 times, but the viscous force increases only 4 to 6 times. The smaller reduction of the pressure force is caused by the increase in the pressure difference between the leading edge and the trailing edge as shown in Figure 9. The larger reduction in the viscous force is due to the smaller

proportional increase in the velocity in the cloak region compared to that in Re and the larger low velocity area near the trailing edge as shown in Figure 5. Therefore, the pressure force increases faster than increase in the Reynolds number, but the viscous force increases slower.

Table 3. Drag force on the circular cylinder without and with cloak at various Reynolds numbers

Re	Pressure Force(μN)		Viscous Force(μN)		Total Drag Force(μN)	
	Without Cloak	With cloak	Without Cloak	With Cloak	Without Cloak	With Cloak
1.5	117.00	7.75	0.991	0.042	117.99	7.79
15	1167.4	92.1	9.89	0.26	1177.3	92.4
150	11456	1263	97	0.9	11553	1264

Thus, the HDMM distorts the pressure fields to reduce the pressure force and distorts the velocity fields to reduce the viscous force. The reduction in drag force due to cloak is obvious but reduces at higher Re. The reason for the reduction is also the effect of the neglected terms in the Navier-Stokes equations in the derivation of the viscosity tensor.

Chapter 3: HDMM Cloak for an Elliptic-Cylinder and a Vertical Flat Plate

3.1 Modeling of HDMM Cloak for an Elliptic-Cylinder

3.1.1 Viscosity Tensor for an Elliptic-Cylinder Cloak

Based on the analysis of the cloak for a circular cylinder, the HDMM cloaks for objects with other shapes are created. The first attempt is to develop a cloak for an elliptic-cylinder because of the similarity between an ellipse and a circle. To obtain the viscosity tensor for an elliptic cloak, the coordinate transformation process is modified. An orthogonal coordinate system is used in the coordinate transformation from virtual space to physical space. The relationship between all concentric circles can be expressed in a polar coordinate system as the ratio between the radii. However, the orthogonal coordinate system around an ellipse consists of a series of conformal ellipses and hyperbolas as shown in Figure 11. Use of the elliptical coordinate systems to derive the viscosity tensor generates a complex Jacobian matrix. Therefore, a simple method to obtain the viscosity tensor for an elliptic cloak is proposed.

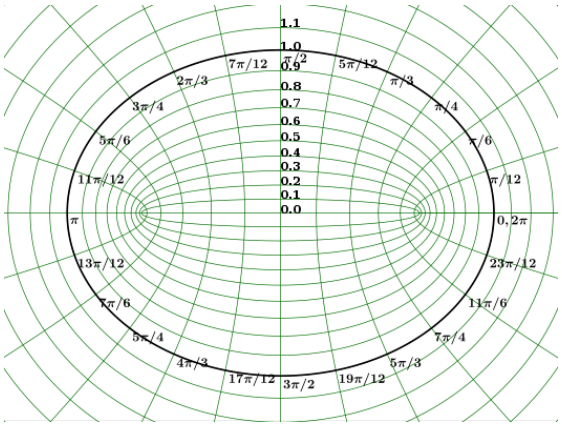

Figure 11. An elliptical orthogonal coordinate system

A circular cloak is shown in Figure 12(a). The inner boundary radius is a and the outer boundary radius is b. This cloak can be considered as a series of concentric cylinders. Every point in the cloak region is on a certain cylinder ($r = na,\ n \in [1, b/a]$). An elliptic cloak stretched k times along x-axis from the circular cloak is shown in Figure 12(b). The elliptic cloak can also be considered as a series of geometrically similar ellipses and any point P in the cloak region is on a certain ellipse. The viscosity tensor is transformed from that of the cylinder cloak as follows.

$$\tilde{\tilde{\mu}}'' = \begin{bmatrix} \mu''_{rr} & \mu''_{r\theta} \\ \mu''_{\theta r} & \mu''_{\theta\theta} \end{bmatrix} = c \begin{bmatrix} \left(\frac{b-a}{b}\right)^2 \left(\frac{r'_{ellipse}}{r'_{ellipse}-a}\right)^2 & 0 \\ 0 & \left(\frac{b-a}{b}\right)^2 \end{bmatrix} \mu \tag{32}$$

where $r'_{ellipse} = \sqrt{\left(\frac{x}{k}\right)^2 + y^2}$. The direction of μ_r and μ_θ is defined by the normal vector on the ellipse at point P, which is $\left(\frac{x}{k^2}i, yj\right)$.

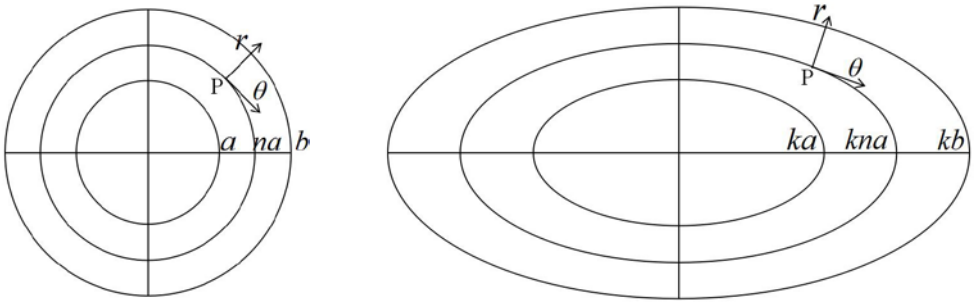

(a) Cylinder cloak (b) Elliptic cloak

Figure 12. Transformation from a cylinder cloak to an elliptic cloak

3.1.2 Simulation Model for an Elliptic-Cylinder Cloak

The simulation model considered is a 40mm*10mm*50μm channel with an elliptic-cylinder as shown in Figure 13. The half-length of the minor axis of the elliptic-cylinder (a) is 2mm. The

stretched ratio (k) is 4 and the half-length of the major axis of the elliptic-cylinder (ka) is 8mm. The cloak is the twice size of the object ($b/a = 2$).

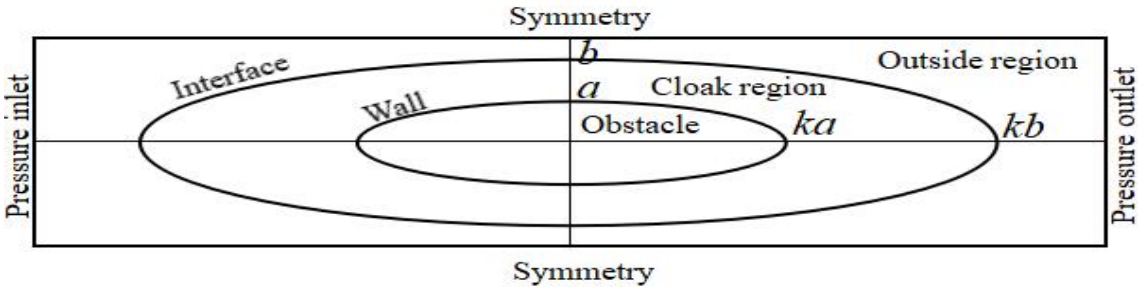

Figure 13. Simulation model and boundary conditions of the elliptic-cylinder cloak

The mesh for the simulation model of Figure 13 is generated in ICEM. The mesh in the cloak region and the region outside the cloak are generated separately and are merged. The outer boundary of the cloak region and the inner boundary of the region outside the cloak are defined as interface and are matched automatically in ANSYS FLUENT. The number of total cells is 90000. The fluid material is water ($\rho = 998.2kg/m^3$ and $\mu = 0.001003kg/(m \cdot s)$). The surface of the object is set as a no-slip stationary wall. The outlet pressure is 0. The gauge pressure at pressure inlet (P) is 4kPa, 40kPa and 400kPa for three cases considered. The relationship among inlet pressure, the theoretical velocity in the bare channel (V_{bare}) calculated by Poiseuille equation and the Reynolds numbers upstream in the channel are shown in Table 4.

Table 4 Inlet pressure, theoretical velocity in the bare channel and Reynolds numbers for the elliptic-cylinder cloak

Inlet Pressure(kPa)	V_{bare} (mm/s)	Re
4	31.25	1.5
40	312.5	15
400	3125	150

The region outside the cloak is modeled as a porous zone ($1/\alpha = 3.2 \times 10^9 [1/m^2]$, $C_2 = 0$). In the cloak region, the porous zone properties are as follows.

$$\frac{1}{\alpha_r} = 3.2 \times 10^9 \times \frac{1}{4} c \left(\frac{r'_{elliptic}}{r'_{elliptic} - 2mm} \right)^2 \left[\frac{1}{m^2} \right]$$

$$\frac{1}{\alpha_\theta} = 3.2 \times 10^9 \times \frac{1}{4} c \left[\frac{1}{m^2} \right]$$

$$C_2 = 0$$

Because the viscosity tensor for the elliptic cloak is not completely derived from the coordinate transformation, the factor c should be determined to find its best value for the elliptic cloak. For this elliptic-cylinder cloak, the factor c is examined at Re=1.5. The deviation in the outlet velocity relative to the theoretical velocity in the bare channel is used to evaluate the effect of c as shown in Table 5. Smaller deviation means that the calculated outlet velocity is closer to that in the bare channel, therefore the hydrodynamic hiding effect of the cloak with c=2.00 is best.

Table 5. Deviation in the outlet velocity with cloak relative to the theoretical velocity in the bare channel for different values of factor c

c	1.50	1.75	2.00	2.25
Deviation (mm/s)	5.54	2.75	0.54	1.30

3.2 Evaluation of the Effect of the HDMM Cloak on an Elliptic-Cylinder

3.2.1 Evaluation of Hydrodynamic Hiding Effect

To evaluate the hydrodynamic hiding effect of the HDMM cloak around the elliptical object, the velocity distribution and streamlines are analyzed. Similar to the circular cylinder

cases, the high velocity areas near both upper and lower surfaces of the objects are enlarged as Figure 14. The low velocity areas near the leading edge and the trailing edge of the ellipse are expanded. When Re increases, the high velocity areas move to downstream and cross the interface between the cloak and the outside region. In the case of Re=1.5, the range of velocity in the outside region is reduced by the cloak from 25mm/s ~ 41mm/s to 30mm/s ~ 33mm/s. Compared to the circular cylinder cloak, the reduction of the range of velocity is weaker; however it still proves the hydrodynamic hiding effect of the elliptic cloak. At Re=150, the velocity in the outside region velocity becomes not uniform in the downstream area of the object.

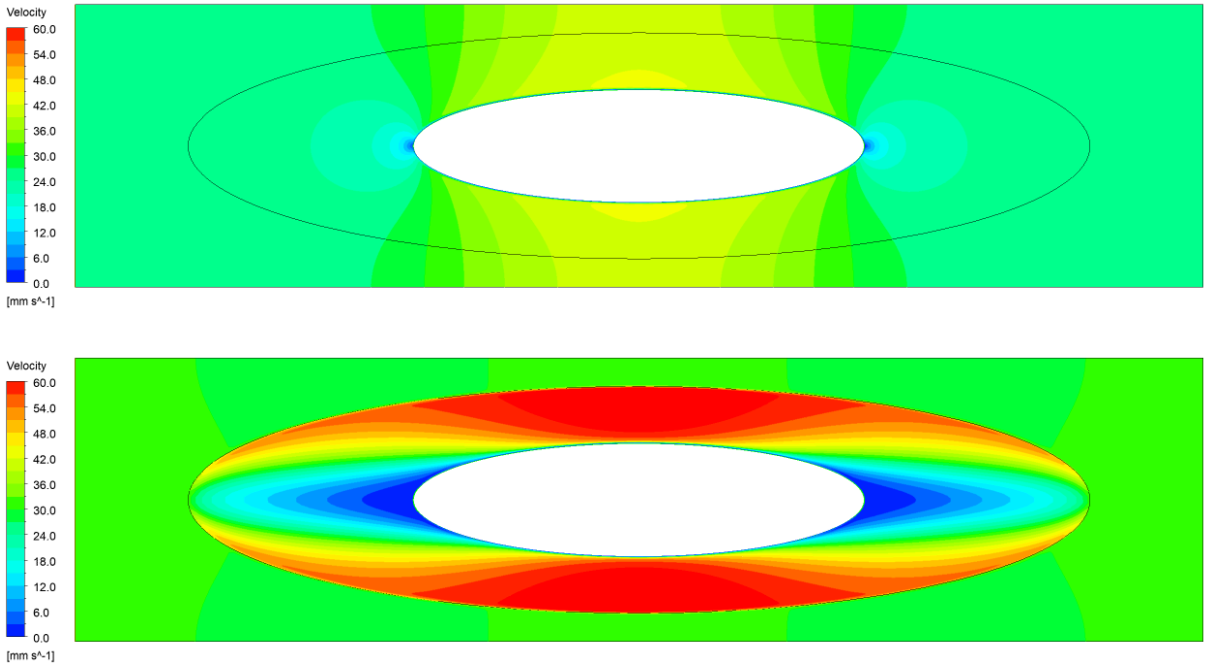

(a) The case without cloak (up) and the case with cloak (down) at Re=1.5

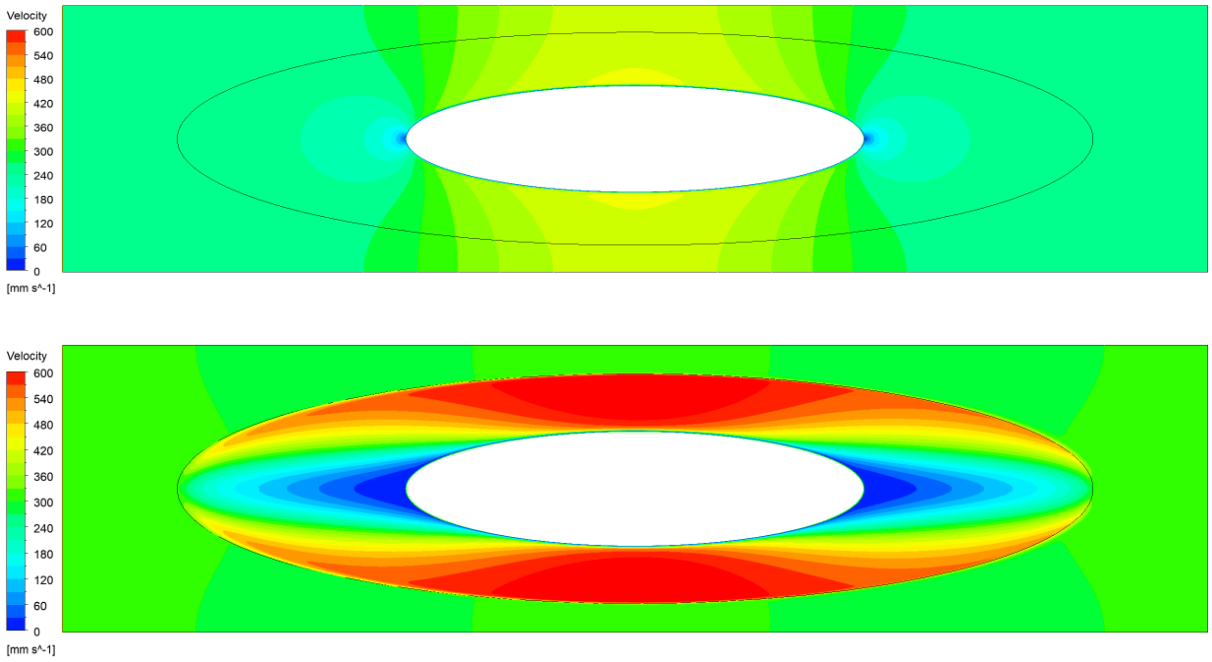

(b) The case without cloak (up) and the case with cloak (down) at Re=15

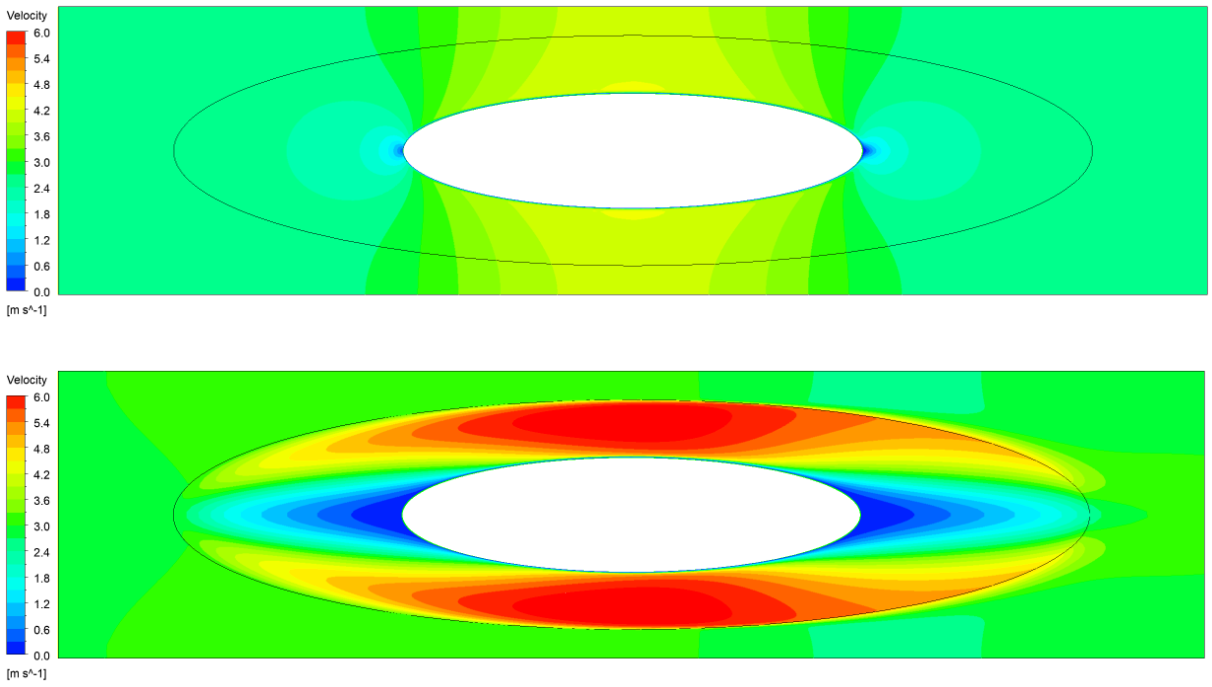

(c) The case without cloak (up) and the case with cloak (down) at Re=150

Figure 14. Velocity fields around the elliptic-cylinder without cloak and with cloak at different Reynolds numbers

Figure 15 shows the outlet velocity profiles for the elliptic-cylinder cases. The cloak reduces the difference between the outlet velocity with cloak and V_{bare} compared that without cloak at all Reynolds number. In the cases with cloak, the velocity difference is slightly smaller near the center line ($|y| < 2mm$). When Re increases, the difference increases in both cases without or with cloak as shown in Figure 15(b) and Figure 15(c). At Re=150, the outlet velocity profile in the case with cloak shows a W-shaped curve.

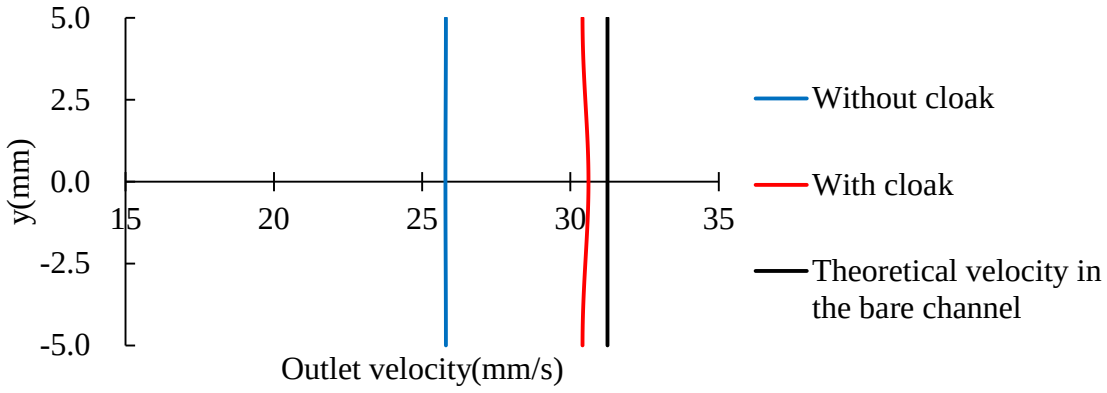

(a) Re=1.5

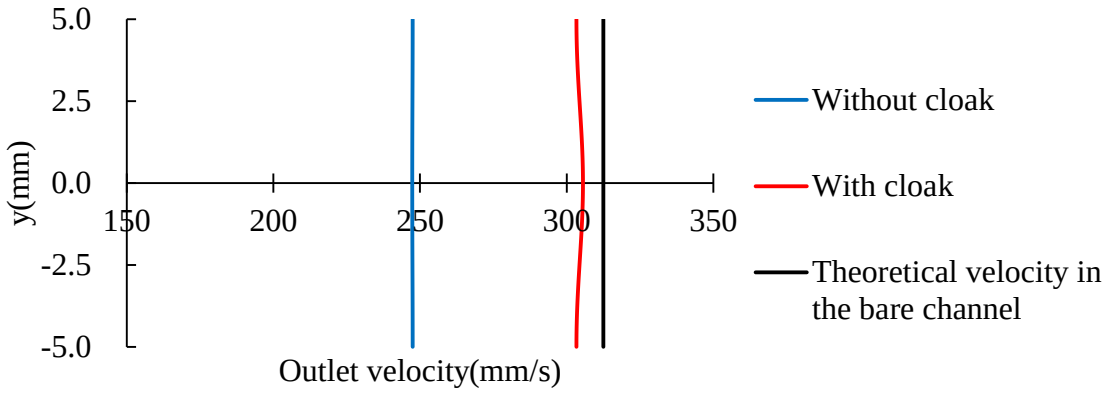

(b) Re=15

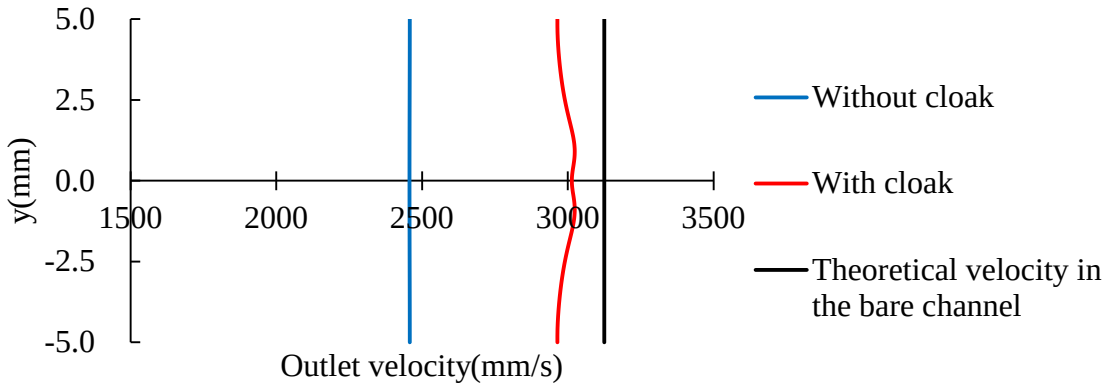

(c) Re=150

Figure 15. Comparison of outlet velocity profiles for elliptic-cylinder without cloak and with cloak at various Reynolds numbers

Table 6 shows the deviation in the outlet velocity without and with cloak relative to V_{bare}. In all cases, the deviation is reduced by the cloak. But the reduction ratio decreases from about 7 to 4 when Re increases from 1.5 to 150.

Table 6 Deviation in the outlet velocity without and with cloak relative to the theoretical velocity in the bare channel for the elliptic-cylinder at various Reynolds numbers

Re	V_{bare} (mm/s)	Deviation(mm/s)	
		Without Cloak	With Cloak
1.5	31.25	5.46	0.75
15	312.5	56.98	8.15
150	3125	535.49	134.58

Figure 16 shows the streamlines around the elliptic-cylinder without and with cloak at various Reynolds numbers. The streamlines become straighter in both upper and lower surfaces of the object in the region outside the cloak.

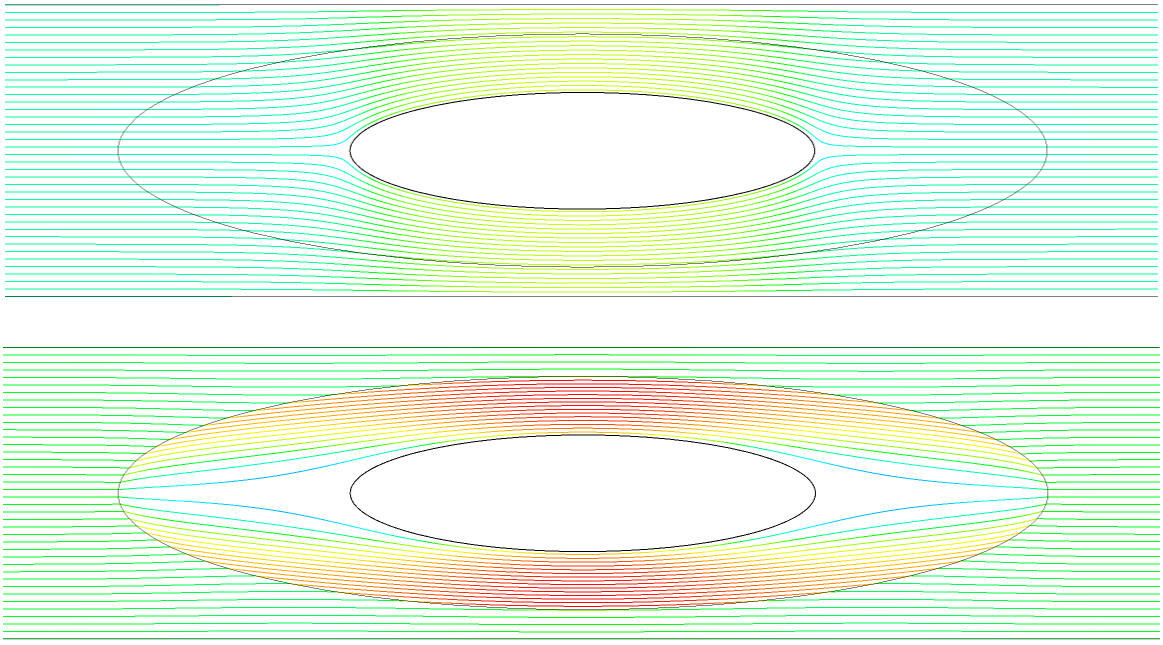

(a) The case without cloak (up) and the case with cloak (down) at Re=1.5

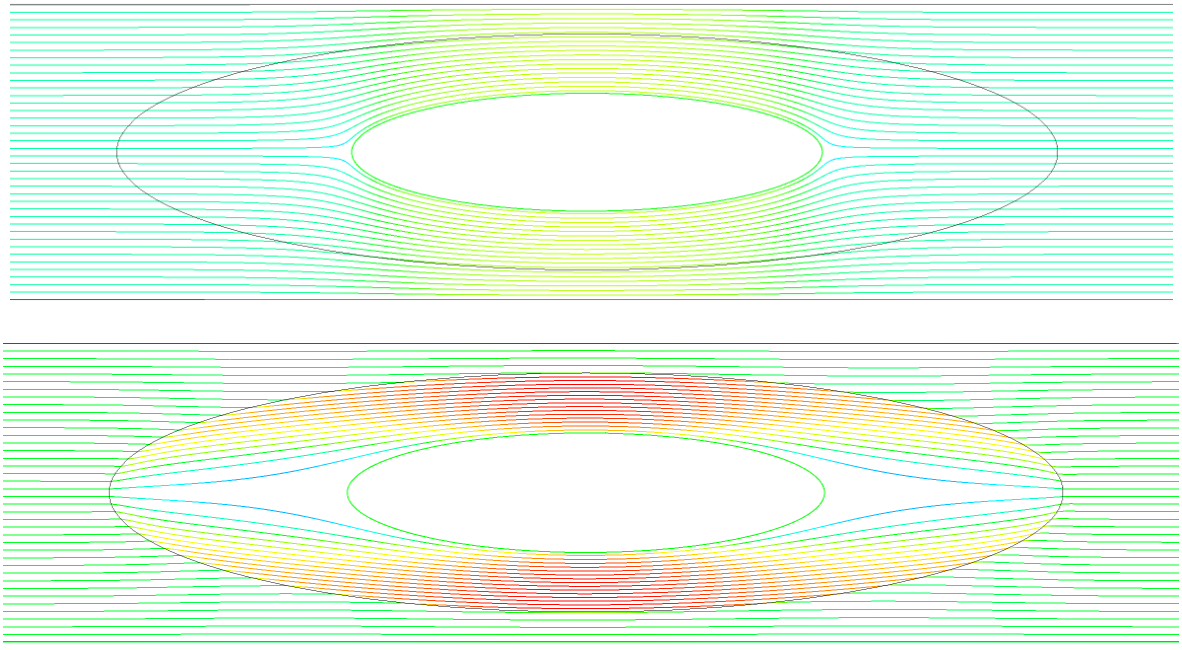

(b) The case without cloak (up) and the case with cloak (down) at Re=15

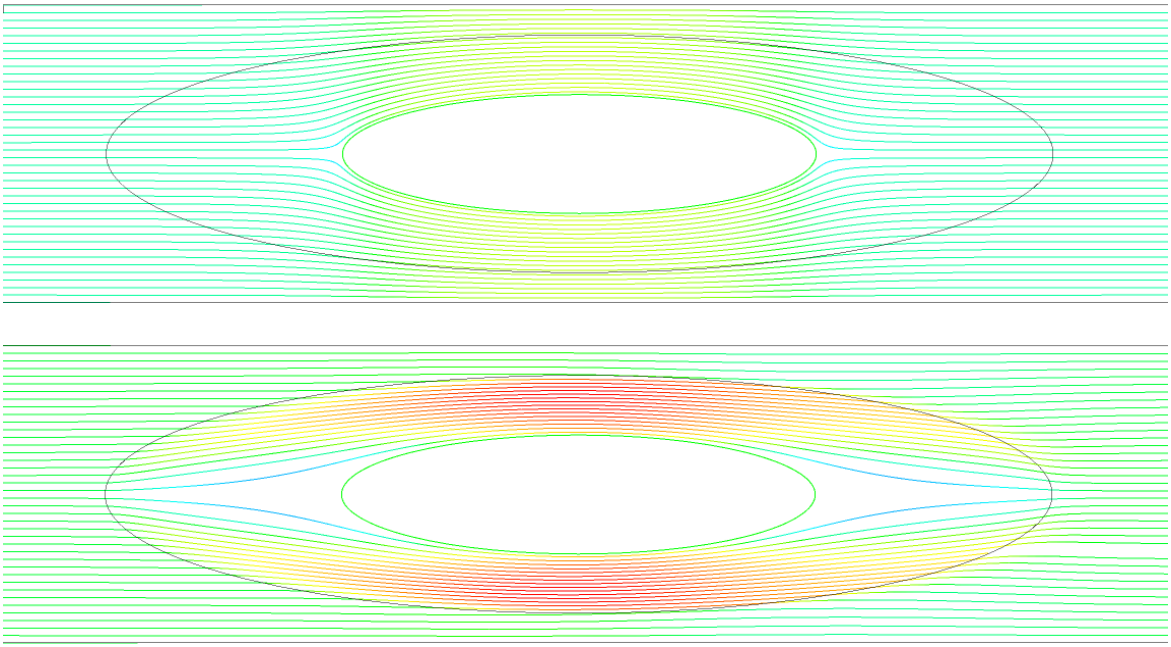

(c) The case without cloak (up) and the case with cloak (down) at Re=150

Figure 16. Streamlines around the elliptic-cylinder without and with cloak at various Reynolds numbers

Thus, the hydrodynamic hiding effect of the elliptic HDMM cloak on the elliptic-cylinder object is similar to the case of the circular HDMM cloak, but the effect is less pronounced because (a) the influence of an elliptical object with the major axis along the free stream is smaller than that of a circular cylinder, and (b) the viscosity tensor in the elliptic cloak region is not exactly generated from the coordinate transformation. The reduction in cloak effect at increasing Re is similar to that in the cases of the circular cylinder cloak.

3.2.2 Evaluation of Drag Reduction Effect

Figure 17 shows the pressure fields around the elliptic-cylinder without and with cloak at various Reynolds numbers. The cloak distorts the pressure fields and reduces the pressure difference between the leading edge and the trailing edge in a manner similar to that for the

circular cylindrical cloak. Also, the increasing Re does not affect the distribution of pressure field significantly.

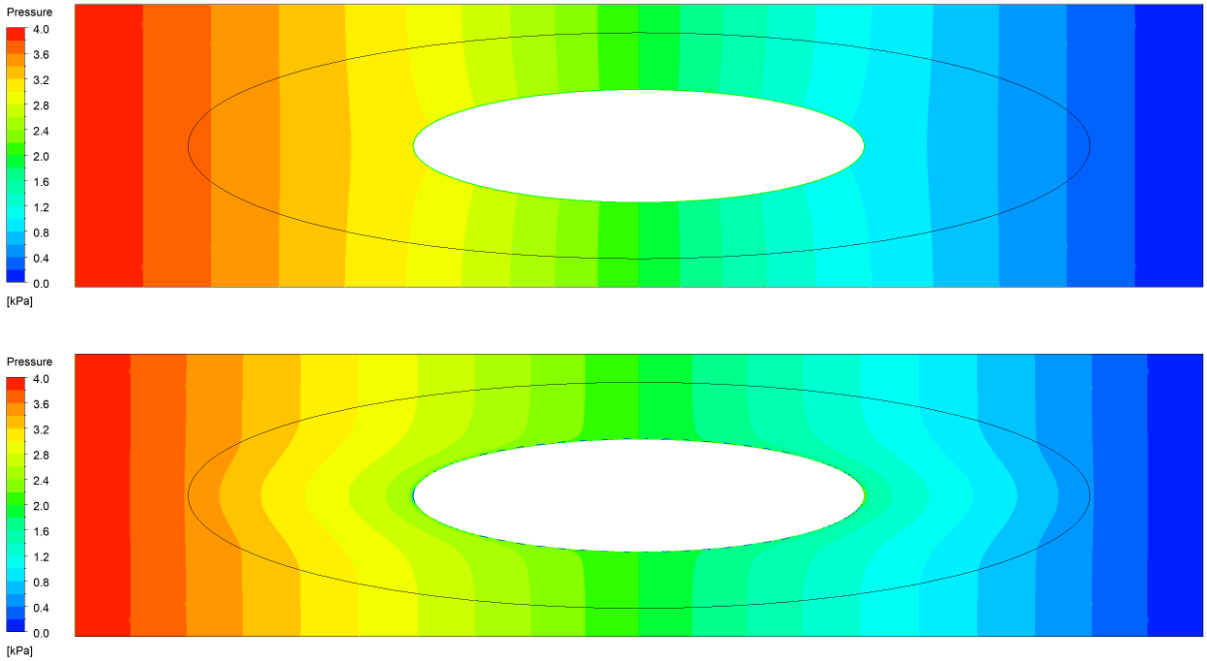

(a) The case without cloak (up) and the case with cloak (down) at Re=1.5

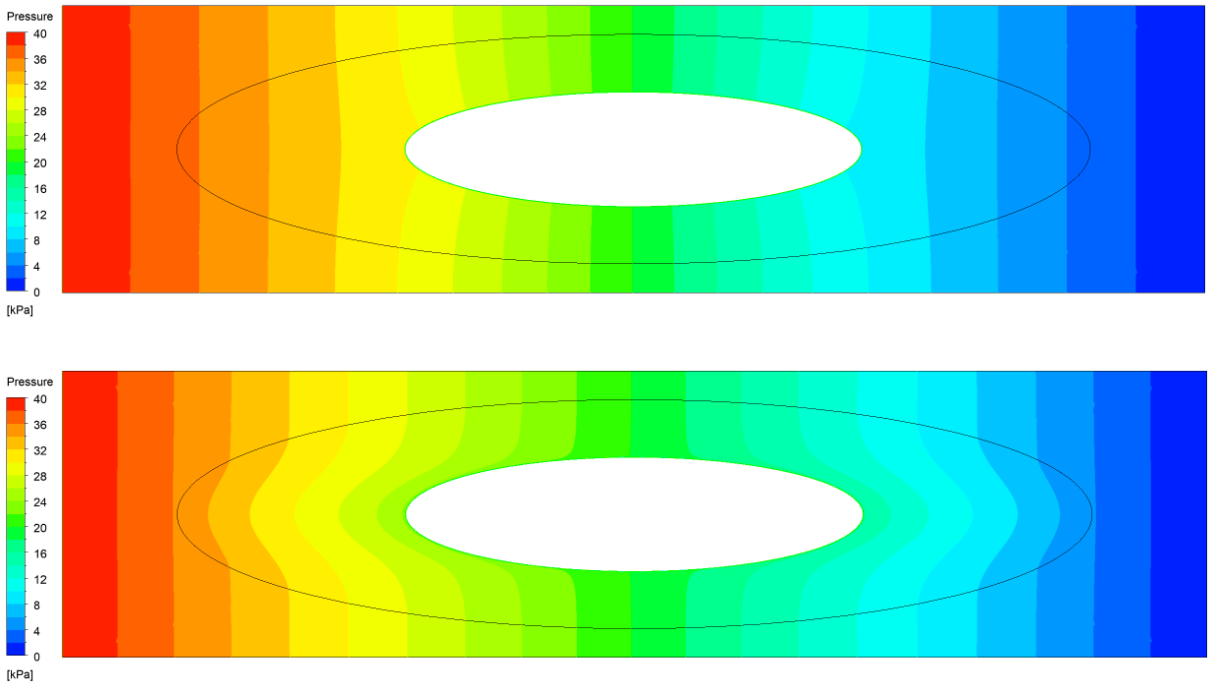

(b) The case without cloak (up) and the case with cloak (down) at Re=15

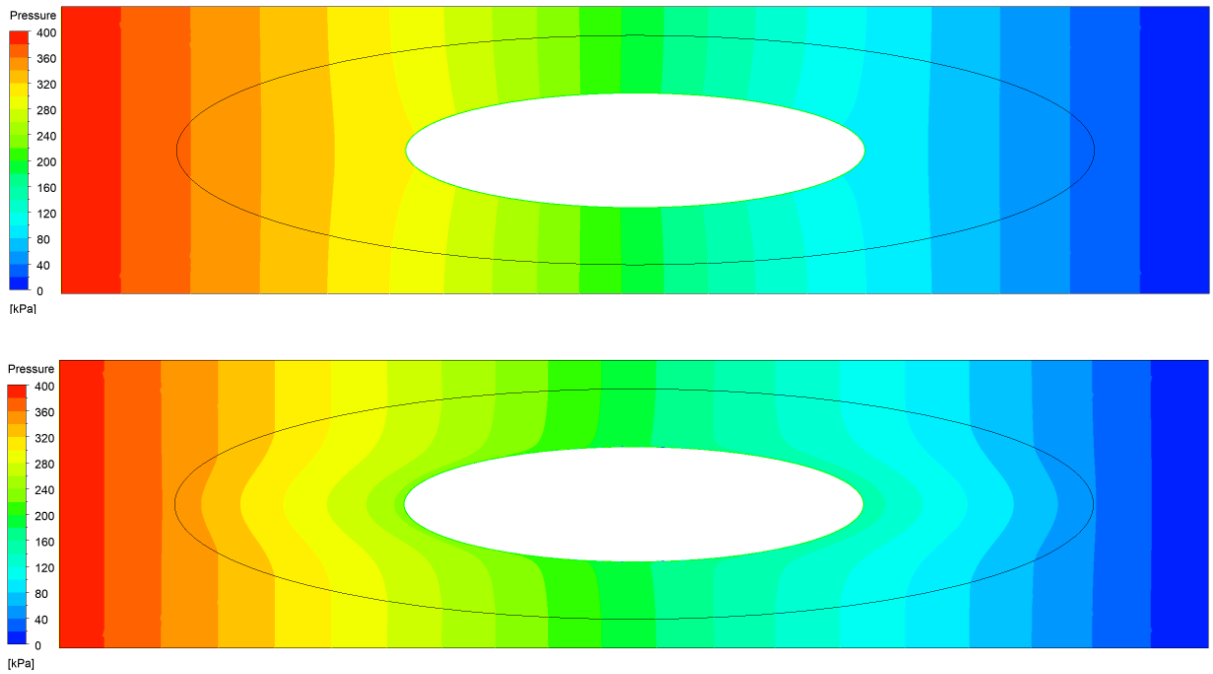

(c) The case without cloak (up) and the case with cloak (down) at Re=150

Figure 17. Pressure fields around the elliptic-cylinder without and with cloak at various Reynolds numbers

Figure 18 shows the wall skin friction coefficient (C_f) on the surface of the elliptic-cylinder at various Reynolds numbers. In the cases without cloak, the wall skin friction coefficient changes rapidly near the leading edge and the trailing edge but gently in the center part. In the cases with cloak, the wall skin friction coefficient is reduced significantly in the area ($|x| > 6.5mm$). In the center area ($|x| < 2mm$), C_f is about 5 times smaller than that in the cases without cloak.

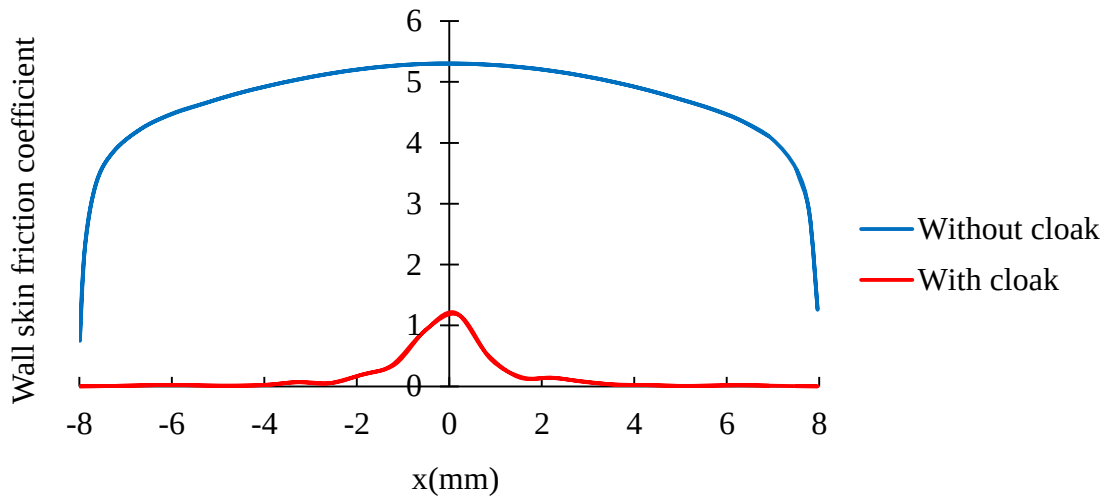
Wall skin friction coefficient
6
5
4
3
2
1
0
-8
-6
-4
-2
0
2
4
6
8
x(mm)
Without cloak
With cloak

(a) Re=1.5

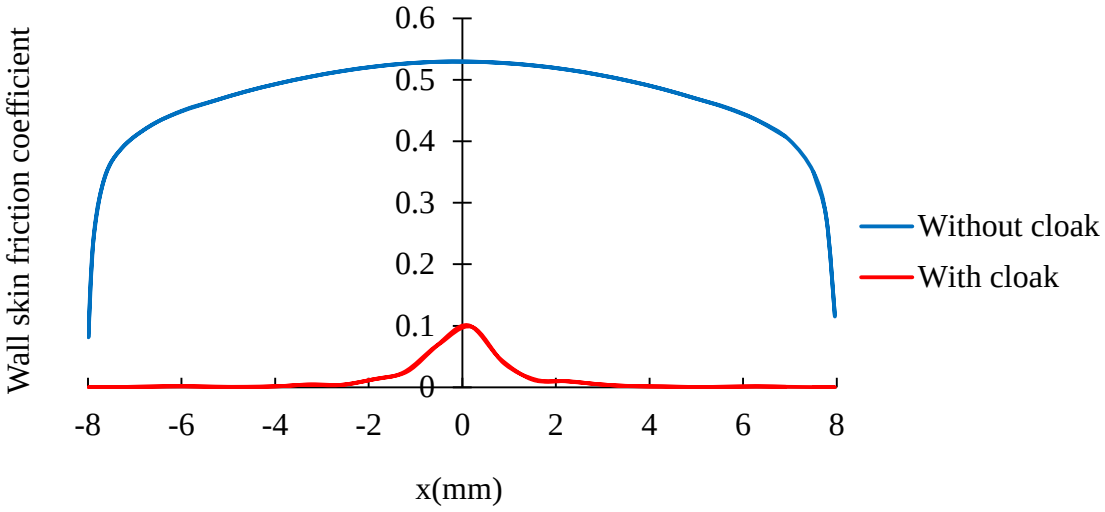
Wall skin friction coefficient
0.6
0.5
0.4
0.3
0.2
0.1
0
-8
-6
-4
-2
0
2
4
6
8
x(mm)
Without cloak
With cloak

(b) Re=15

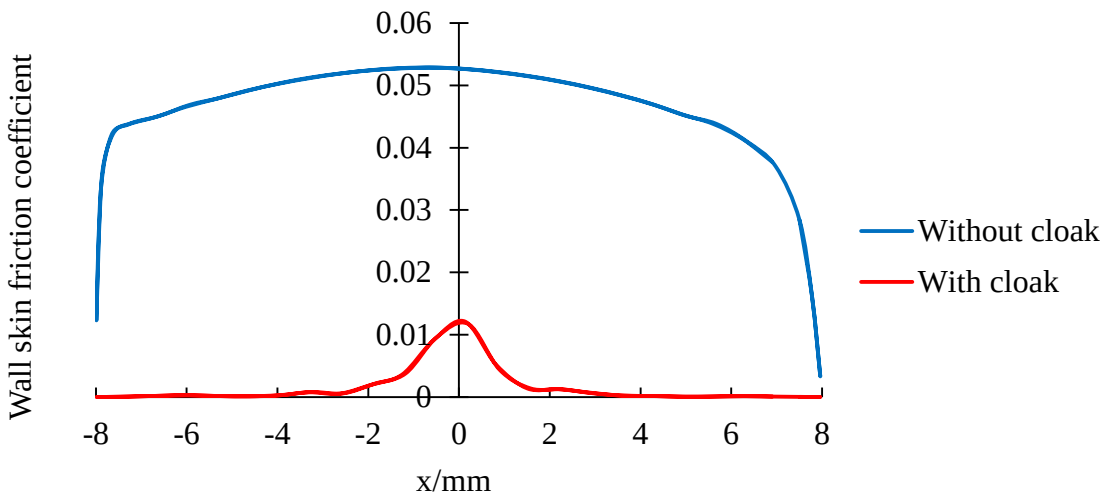

(c) Re=150

Figure 18. Wall skin friction coefficient on the surface of the elliptic-cylinder without and with cloak at various Reynolds numbers

Table 7 shows the drag force on the elliptic-cylinder at various Reynolds numbers. Affected by the cloak, the pressure force is reduced by about 2.5 times and the viscosity force is reduced by about 28 times compared to that without cloak. The total drag force is reduced by about 2.5 times since it is mainly dominated by the pressure force. The relationship between the reduction in drag vs. Re is not obvious.

Table 7. Drag force on the elliptic-cylinder without and with cloak at various Reynolds numbers

Re	Pressure Force(μN)		Viscous Force(μN)		Total Drag Force(μN)	
	Without Cloak	With cloak	Without Cloak	With Cloak	Without Cloak	With Cloak
1.5	355	135	3.535	0.125	358.54	135.13
15	3549	1408	35.00	1.24	3584.0	1409.2
150	35263	13655	352.0	12.3	35615	13667

Thus, the drag reduction effect of the HDMM cloak on the elliptic-cylinder is significant but is weaker compared to that for the circular cylinder cloak. The main reason is the viscosity tensor which is not exactly derived from the coordinate transformation.

3.3 Modeling of the Hydrodynamic Cloak for a Thin Vertical Elliptic-cylinder (Vertical Flat Plate)

The HDMM cloak for a vertical flat plate is created based on the cloak for the elliptic-cylinder described in Section 3.2. To simplify the problem, the plate is modeled as a vertical thin elliptic-cylinder. Figure 19 shows the simulation model and the boundary conditions for the vertical thin elliptic-cylinder. The model is a 40mm*40mm*50μm channel with an elliptic-cylinder object. The half-length of the major axis of the plate (a) is 5mm. The ratio between minor and major axes (k) is 0.1 and the half-length of the minor axis of the object (ka) is 0.6mm. The cloak is twice the size of the object ($b/a = 2$).

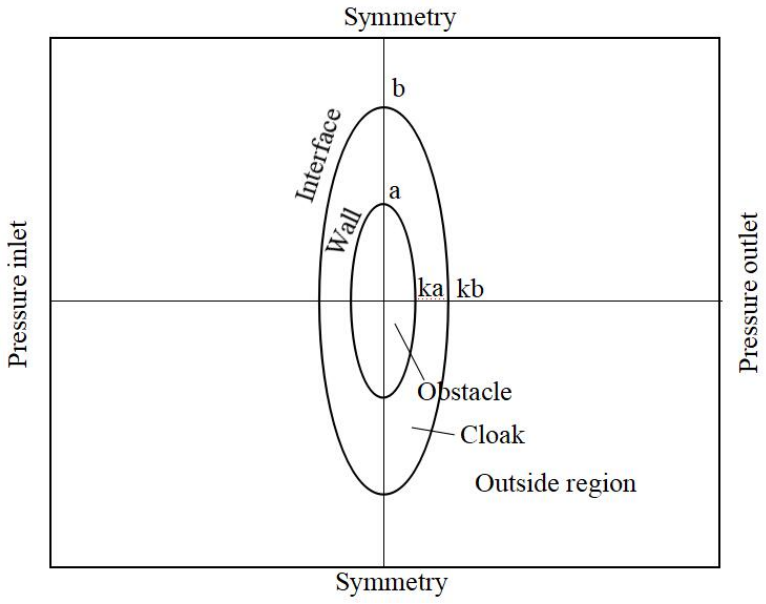

Figure 19. Simulation model and boundary conditions of the flat plate cases

The mesh for the simulation model is generated in ICEM. The total number of cells is 38000. The fluid material is air ($\rho = 1.225kg/m^3$ and $\mu = 1.7894 \times 10^{-5}kg/(m \cdot s)$). The surface of the object is set as a no-slip stationary wall. The outlet pressure is 0. The gauge pressure at pressure inlet (P) is 0.669kPa, 6.69kPa and 66.9kPa for three cases considered. The relationships among inlet pressure, V_{bare} and Re are shown in Table 8. The properties of the porous zone are set in the same way as for the elliptic-cylinder described in Section 3.2.

Table 8. Inlet pressure, theoretical velocity in the bare Channel and Reynolds numbers for the vertical flat plate

Inlet Pressure (kPa)	V_{bare} (mm/s)	Re
0.669	0.2921	1
6.69	2.921	10
66.9	29.21	100

3.4 Evaluation of the Effect of the HDMM on a Flat Plate

In the vertical flat plate cases, the plate does not have obvious influence on the fluid in the region outside the cloak, therefore the hydrodynamic hiding effect of the cloak is unimportant. The velocity fields around the vertical flat plate cases are shown in Figure 19. The cloak changes the velocity distribution near both upward and downward edges of the plate. The high velocity areas near the upward and downward edges are divided into two parts respectively. The influence of Re is significant near the back surface of the plate. Low velocity areas are larger at higher Re.

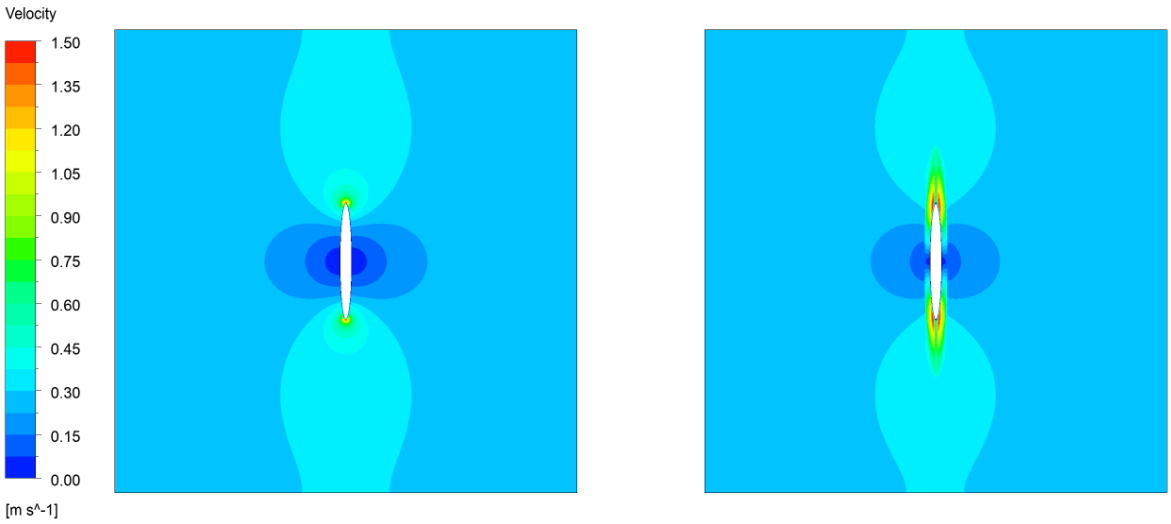

(a) The case without cloak (left) and the case with cloak (right) at Re=1

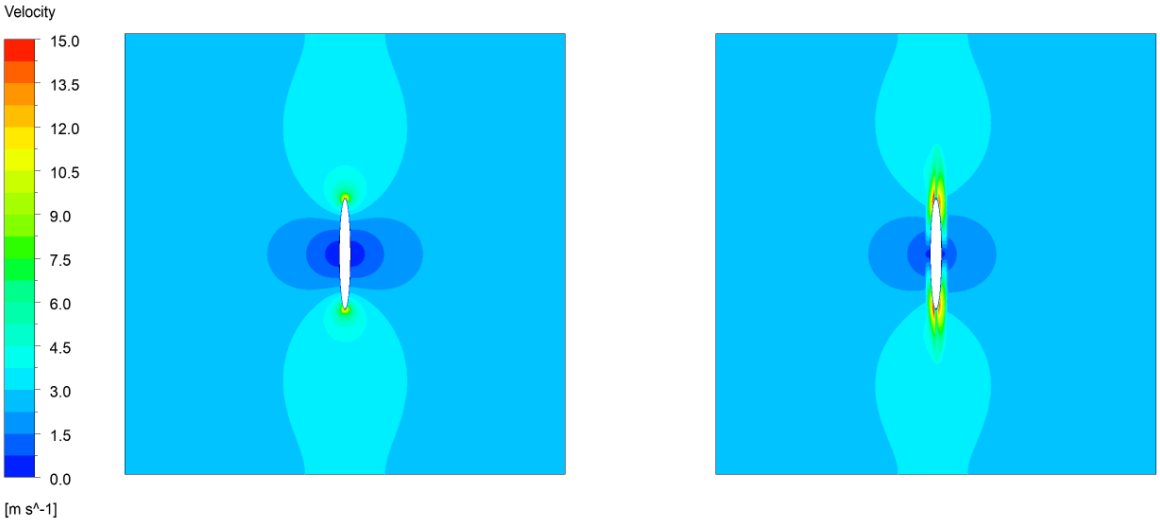

(b) The case without cloak (left) and the case with cloak (right) at Re=10

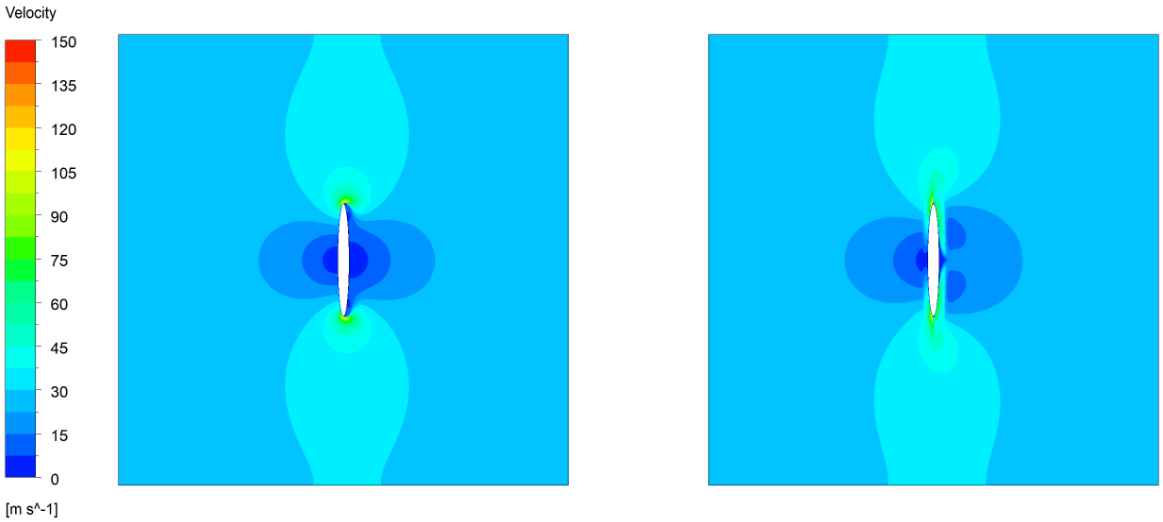

(c) The case without cloak (left) and the case with cloak (right) at Re=100

Figure 20. Velocity fields around the vertical flat plate without and with cloak at various Reynolds numbers

Figure 21 shows the pressure fields around the vertical flat plate at various Reynolds numbers. Compared to the elliptic-cylinder cloak described in Section 3.2, the change in the pressure contours is much weaker. Also, the influence of Re is small.

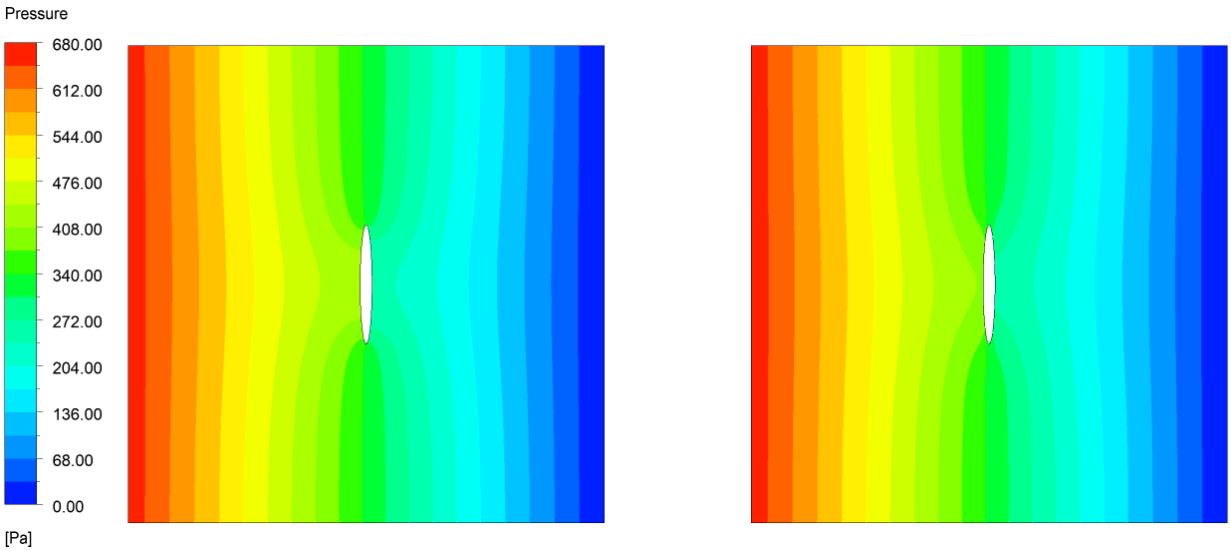

(a) The case without cloak (left) and the case with cloak (right) at Re=1

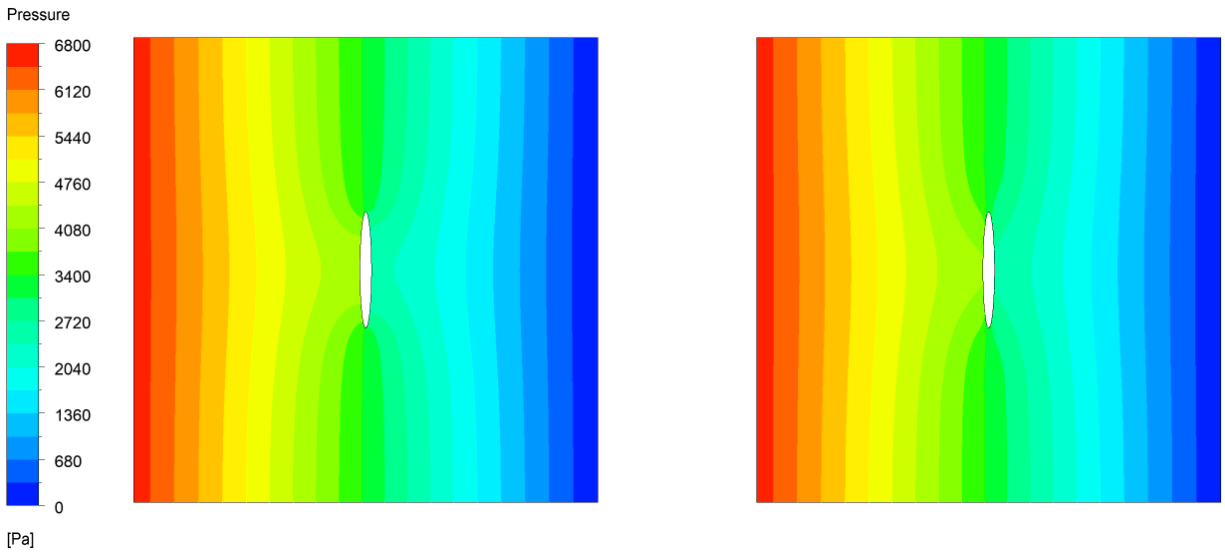

(b) The case without cloak (left) and the case with cloak (right) at Re=10

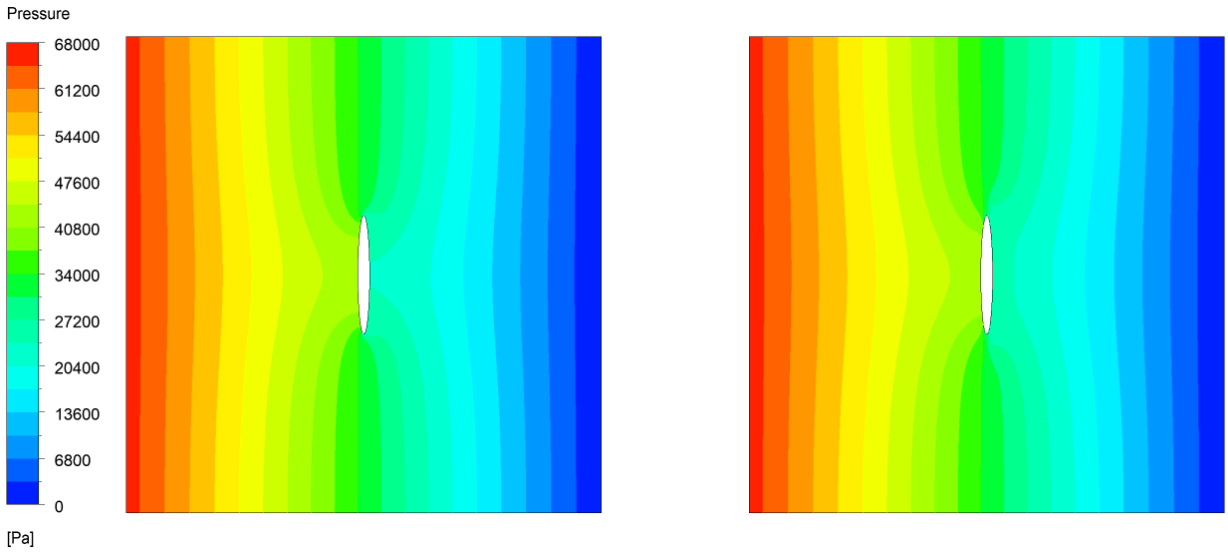

(c) The case without cloak (left) and the case with cloak (right) at Re=100

Figure 21. Pressure fields around the vertical flat plate without and with cloak at various Reynolds numbers

Figure 22 shows the wall skin friction (C_f) on the surface of the plate. Affected by the cloak, C_f is reduced significantly near the upward and downward edges (|y|=5mm). The

distribution of C_f is symmetric about *y*-axis at Re=1 in both cases without and with cloak. When Re increase, C_f on the front surface (towards the flow) is larger than C_f on the back surface.

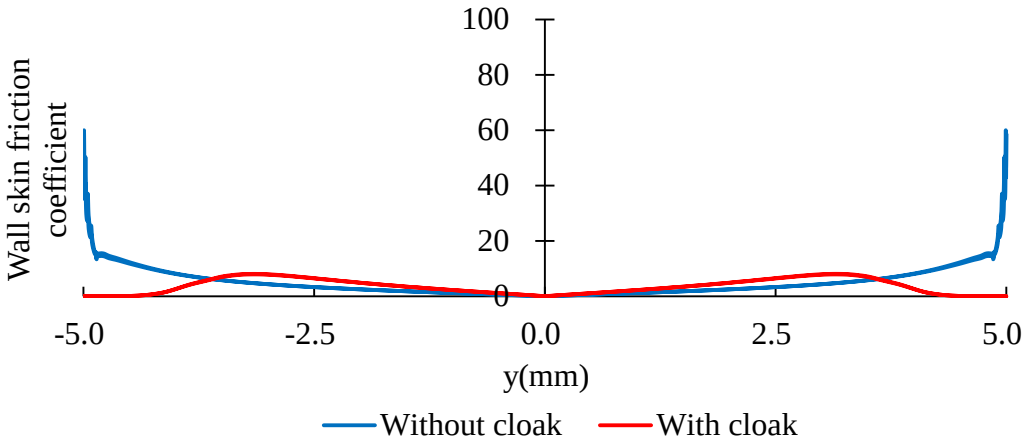

(a) Re=1

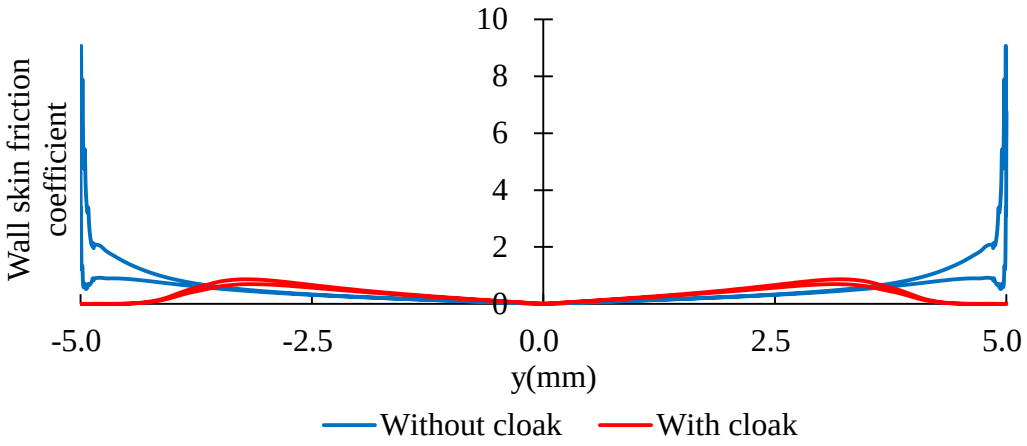

(b) Re=10

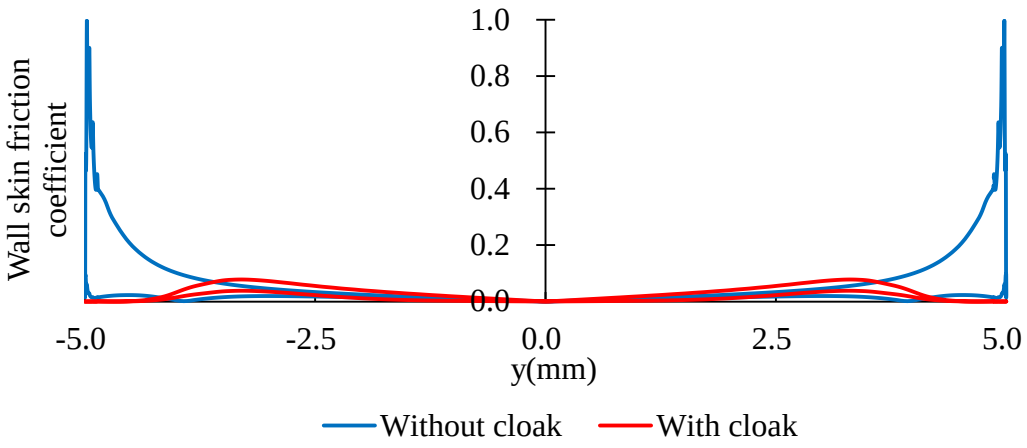

(c) Re=100

Figure 22. Wall skin friction coefficient on the vertical flat plate surface without and with cloak at various Reynolds numbers

Table 9 shows the drag force on the vertical flat plate for various cases. Affected by the cloak, the pressure force is reduced by about 1.5 times and the viscous force is reduced by about 6 times at Re=1 or 10. The total drag force is reduced by about 1.5 times. When Re increases from 10 to 100, the increase in the pressure force is bigger than that at Re=10 but that for the viscous force is smaller. The reduction in the drag force due to the cloak is about 1.3 at Re=100.

Table 9. Drag force on the vertical flat plate without and with cloak at various Reynolds numbers

Re	Pressure Force(μN)		Viscous Force(μN)		Total Drag Force(μN)	
	Without Cloak	With cloak	Without Cloak	With Cloak	Without Cloak	With Cloak
1	71.46	47.64	0.0784	0.0129	71.54	47.650
10	717.1	499.7	0.762	0.127	717.8	499.9
100	8059	6963	5.90	0.92	8065	6964

The evaluation of the hydrodynamic hiding effect and drag reduction effect of the elliptic HDMM cloak on the elliptic-cylinder and the vertical flat plate (thin vertical elliptic-cylinder) shows that the creation of a cloak for an object of different shapes by stretching a circular cloak

is feasible. The shape of the cloak which is designed based on the shape of the object affects its performance. Although the effect of the stretched cloak is less than the circular cylinder cloak, it is still very significant.

Chapter 4: HDMM Cloak for an Airfoil

4.1 Modeling of the Simplified Airfoil HDMM Cloak for an Airfoil

4.1.1 Viscosity Tensor for the Simplified Airfoil Cloak

Based on the results of the elliptic cloak cases described in Chapter 3, an attempt to create a cloak for an airfoil is conducted. The geometry of the airfoil considered is NACA0015. Its shape equation is given as follows.

$$y_t = 5t\left[0.2969\sqrt{x'} - 0.1260x' - 0.3516x'^2 + 0.2843x'^3 - 0.1015x'^4\right] \tag{33}$$

where $t = 0.15$ and x' is the position along the chord from 0 to 1.00 (0 to 100%). A method in which the airfoil is thought of as some geometrically connected ellipses approximately is proposed to simplify the creation of an airfoil cloak. In the shape equation of NACA0015, the largest thickness is at $x' = 0.3$. The airfoil is divided into two parts, the leading part ($x' < 0.3$) and the trailing part ($x' \geq 0.3$). Each part is approximated as a semi-ellipse. The expressions of these two semi-ellipses are as follows.

$$\begin{cases} y = \pm 0.95 \times 0.075 \times \sqrt{1 - \left(\dfrac{x' - 0.3}{0.3}\right)^2}, & 0 < x' \leq 0.3 \\ y = \pm 0.95 \times 0.075 \times \sqrt{1 - \left(\dfrac{x' - 0.3}{0.5}\right)^2}, & 0.3 < x' \leq 0.8 \end{cases}$$

Figure 23 shows the relation between the simplified airfoil and the original airfoil. Because the viscosity tensor is defined in the cloak region which consists of the region from the simplified airfoil to the interface between the cloak region and the region outside the cloak, the

simplified airfoil must be covered by the original airfoil to ensure the viscosity tensor in the whole area of the cloak region is properly defined as shown in Figure 23.

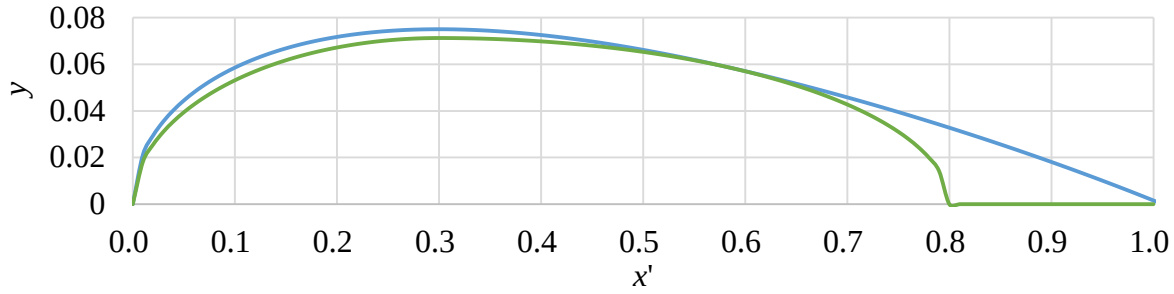

Figure 23. Geometry of NACA0015 airfoil (blue) and the simplified airfoil (green)

4.1.2 Simulation Model of the Simplified Airfoil Cloak

Figure 24 shows the simulation model and the boundary conditions of the simplified airfoil cloak. The simulation model is a 50mm*20mm*50μm channel with an airfoil object of the original airfoil shape. The total length of the airfoil is 20mm. The origin is set at $x' = 0.3$. The simplified airfoil is the blue curve and the simplified airfoil- like cloak is proportional enlarged based on the origin point as shown in Figure 24. The size of the cloak is 2 times the simplified airfoil. The width of the simplified airfoil cloak is 5.7mm. The length of the simplified airfoil cloak is 12mm for the leading part and 20mm for the trailing part.

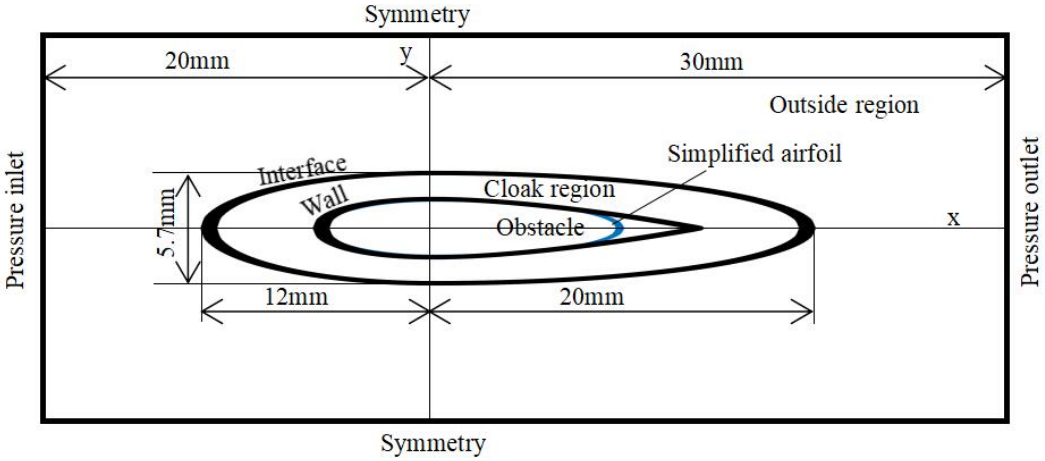

Figure 24. Simulation model and boundary conditions of the simplified airfoil cloak

The fluid material is set as air ($\rho = 1.225kg/m^3$ and $\mu = 1.7894 \times 10^{-5}kg/(m \cdot s)$) for the airfoil cases. The surface of object is set as a no-slip stationary wall. The outlet pressure is 0. The gauge pressure at pressure inlet (P) is 0.836kPa, 8.36kPa and 83.6kPa for three cases. The relationships among the inlet pressure, the velocity in the bare channel calculated by the Poiseuille equation and the Reynolds numbers are shown in Table 10.

Table 10. Inlet pressure, theoretical velocity in the bare channel and Reynolds numbers for the simplified airfoil cloak

Inlet Pressure(kPa)	Theoretical Velocity(m/s)	Re
0.836	0.2921	1
8.36	2.921	10
83.6	29.21	100

The porous zone properties are derived in the same way as for the elliptic-cylinder cases in Chapter 3. The region outside the cloak is modeled as a porous zone ($1/\alpha = 3.2 \times 10^9 [1/m^2]$, $C_2 = 0$). In the cloak region, the porous zone properties are as follows.

$$\frac{1}{\alpha_r} = 3.2 \times 10^9 \times \frac{1}{4} c \left(\frac{r'_{elliptic}}{r'_{elliptic} - 1.425mm} \right)^2 \left[\frac{1}{m^2} \right]$$

$$\frac{1}{\alpha_\theta} = 3.2 \times 10^9 \times \frac{1}{4} c \left[\frac{1}{m^2} \right]$$

$$C_2 = 0$$

where

$$r'_{elliptic} = \begin{cases} \sqrt{\left(\frac{x}{4.21}\right)^2 + y^2}, & x \le 0 \\ \sqrt{\left(\frac{x}{7.07}\right)^2 + y^2}, & x > 0 \end{cases}$$

4.2 Evaluation of the Effect of the Simplified Airfoil HDMM Cloak on an Airfoil

To evaluate the hydrodynamic hiding effect of the simplified airfoil HDMM cloak on the airfoil, the velocity fields and streamlines are analyzed. Figure 25 shows the velocity fields around the airfoil without and with the simplified airfoil cloak at various Reynolds numbers. The velocity distribution is similar to the elliptic-cylinder cloak cases in Chapter 3. The high velocity areas near the upper and lower surfaces of the airfoil are enlarged in the cloak region. The low velocity areas are enlarged near the leading edge and the trailing edge. When Re increases, the velocity field increases in the same proportion in both cases without cloak and cases with cloak. At Re=1, the velocity distribution in the region outside the cloak varies from 0.27m/s to 0.35m/s without cloak and varies from 0.28m/s to 0.32m/s with cloak as shown in Figure 25(a).

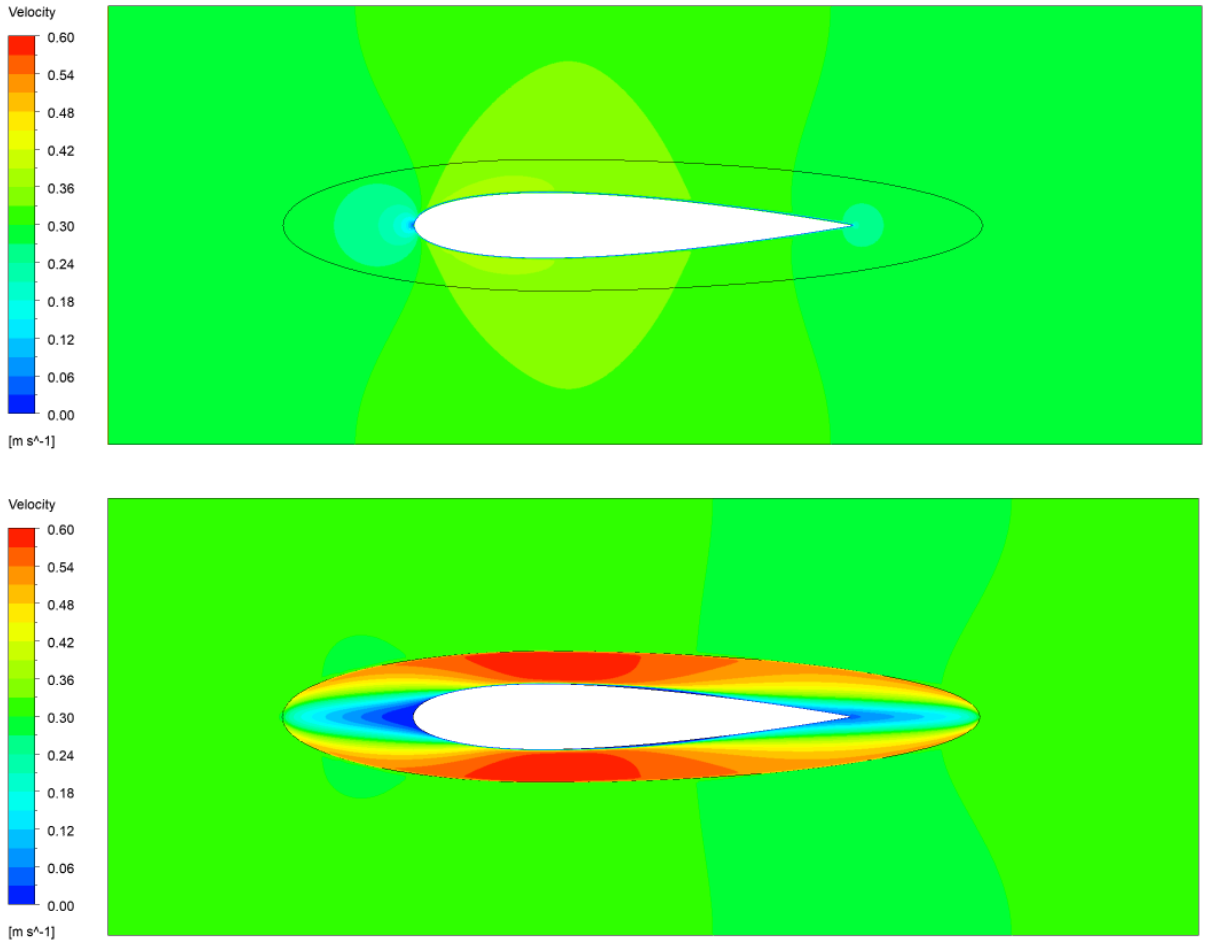

(a) The case without cloak (up) and the case with cloak (down) at Re=1

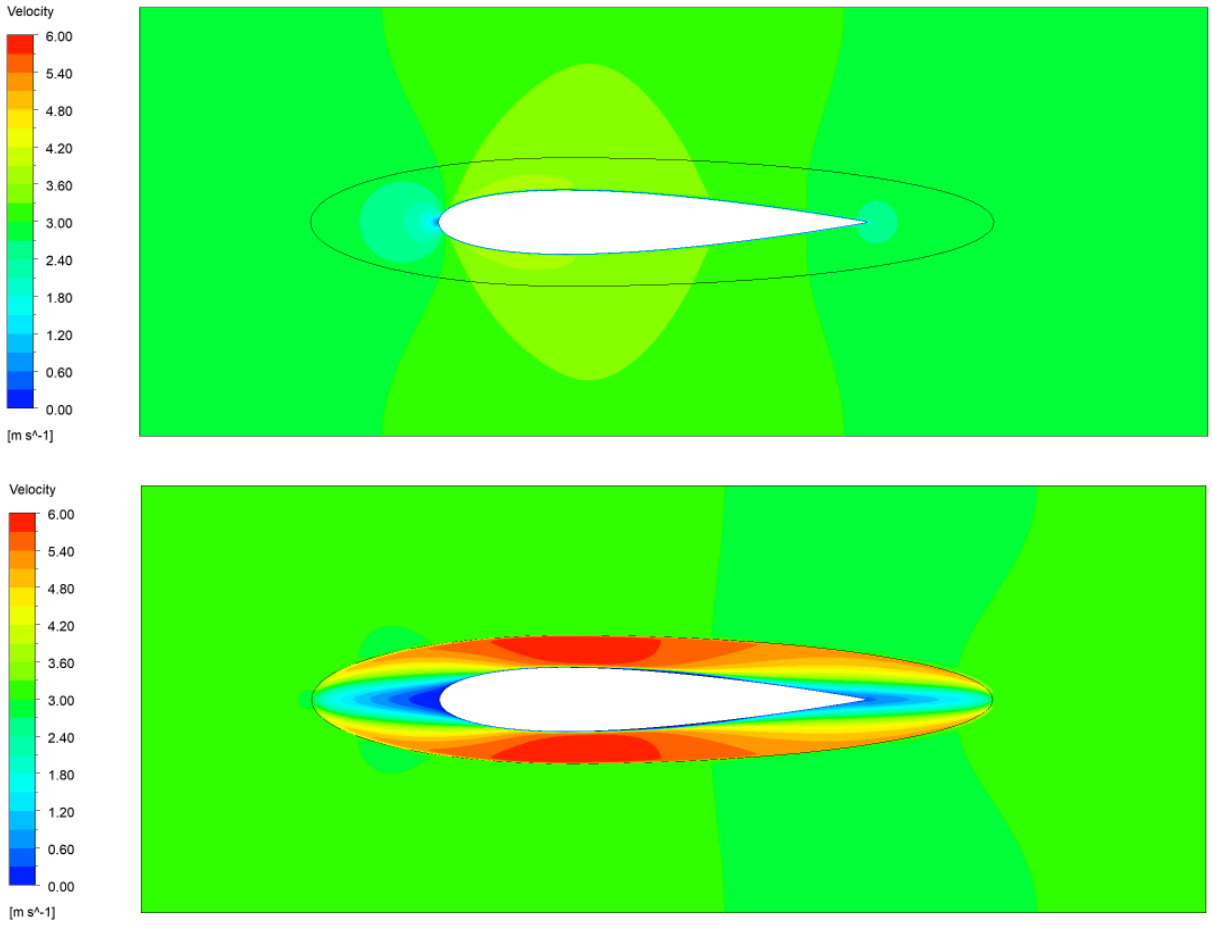

(b) The case without cloak (up) and the case with cloak (down) at Re=10

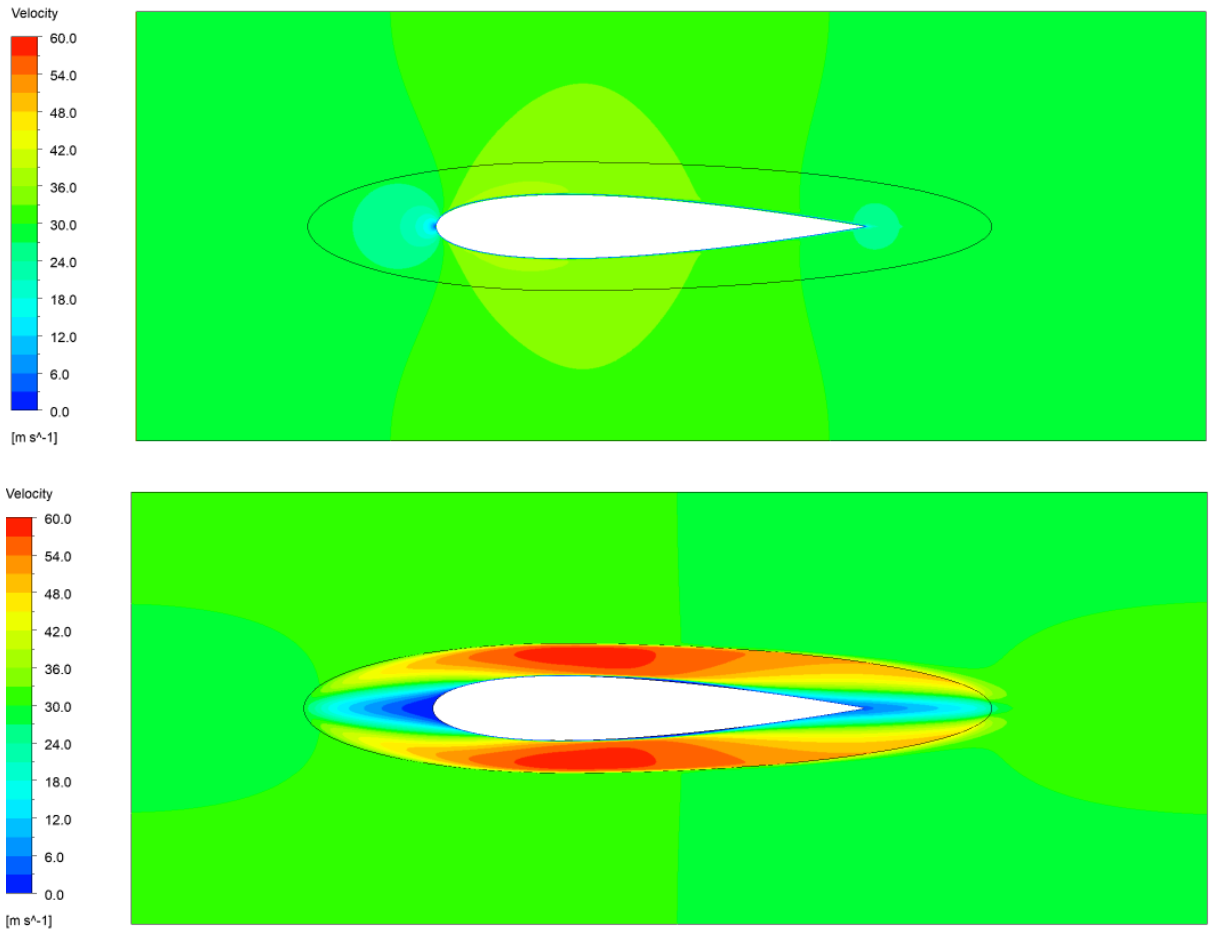

(c) The case without cloak (up) and the case with cloak (down) at Re=100

Figure 25. Velocity fields around the airfoil without and with the simplified airfoil cloak at various Reynolds numbers

Figure 26 shows the streamlines around the airfoil without and with the simplified airfoil cloak at various Reynolds numbers. The streamlines on both upper and lower surfaces of the airfoil in the region outside the cloak are straighter in the cases with cloak compared to those without the cloak.

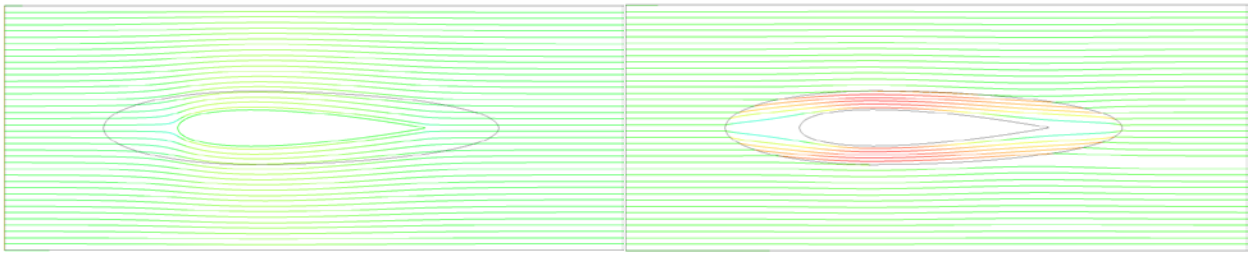

(a) The case without cloak (left) and the case with cloak (right) at Re=1

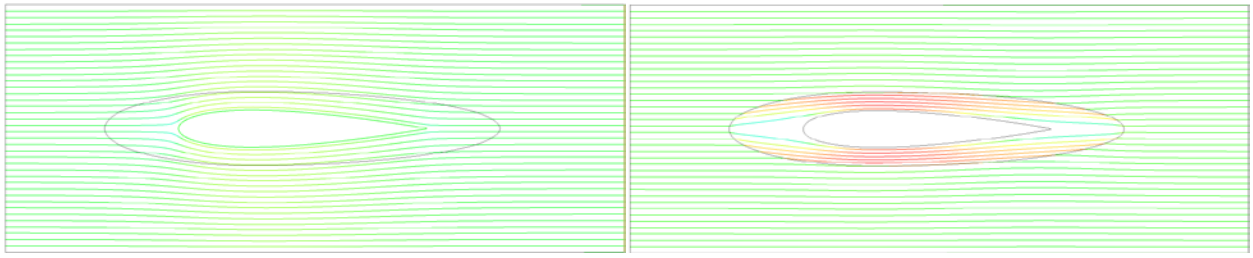

(b) The case without cloak (left) and the case with cloak (right) at Re=10

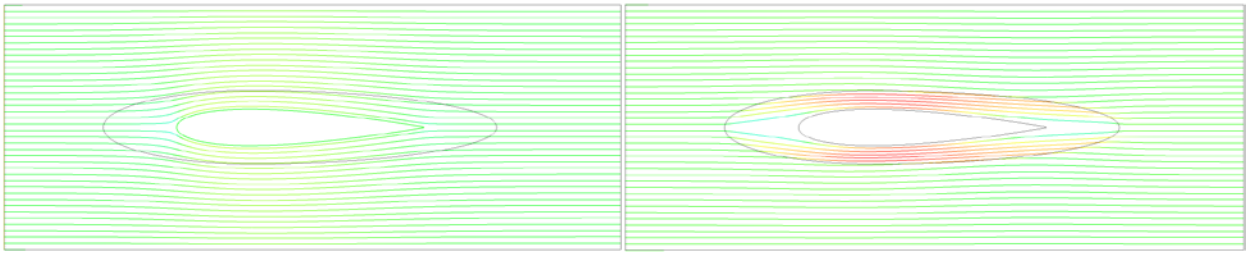

(c) The case without cloak (left) and the case with cloak (right) at Re=100

Figure 26. Streamlines around the airfoil without and with the simplified airfoil cloak at various Reynolds numbers.

Figure 27 shows the pressure fields around the airfoil without and with the simplified airfoil cloak at various Reynolds numbers. The pressure fields change with the inlet pressure proportionally in both cases without cloak and with cloak. The pressure contours in the cloak region are bent by the cloak in a similar fashion as in the cases of the elliptic-cylinder cloak cases described in Chapter 3 to reduce the pressure difference between the leading edge and the trailing edge of the airfoil.

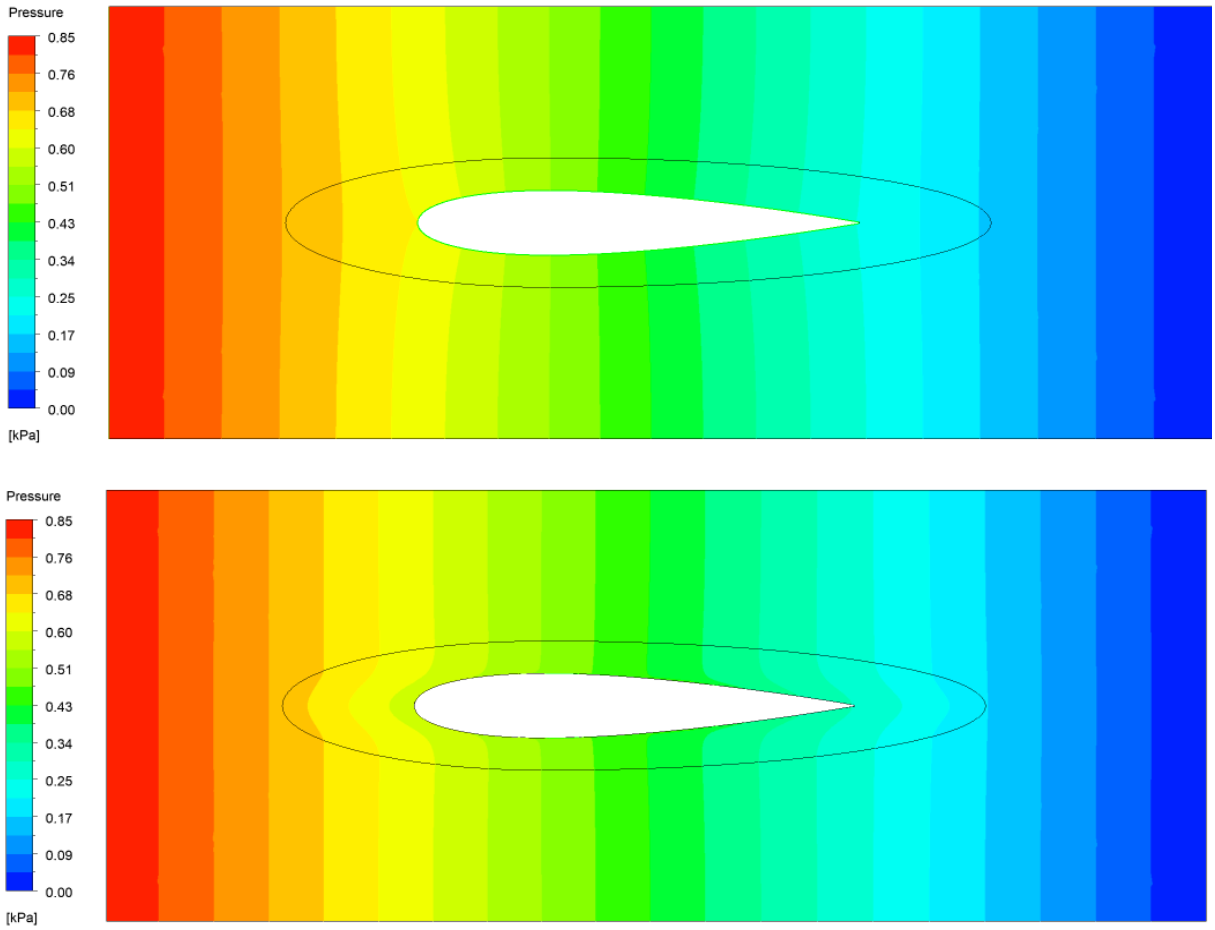

(a) The case without cloak (up) and the case with cloak (down) at Re=1

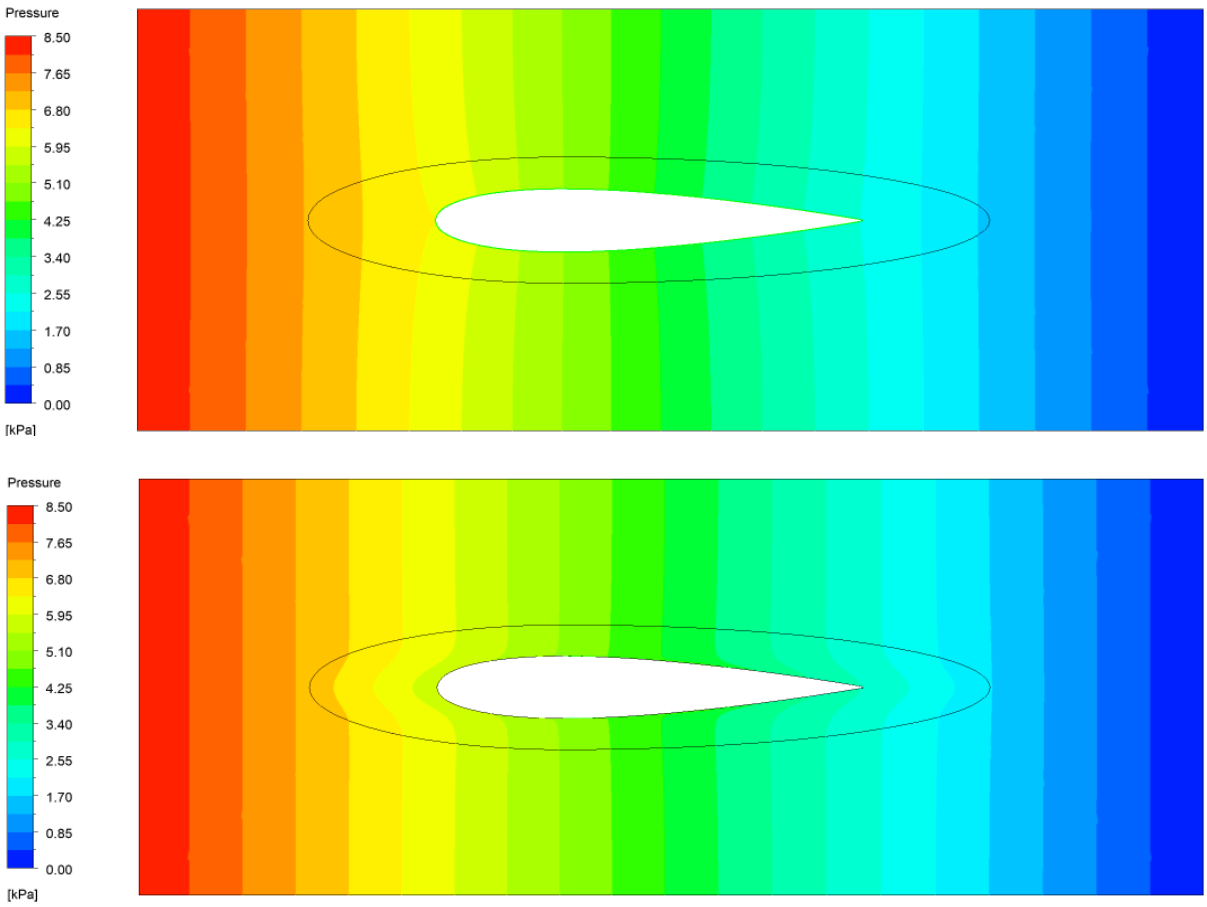

(b) The case without cloak (up) and the case with cloak (down) at Re=10

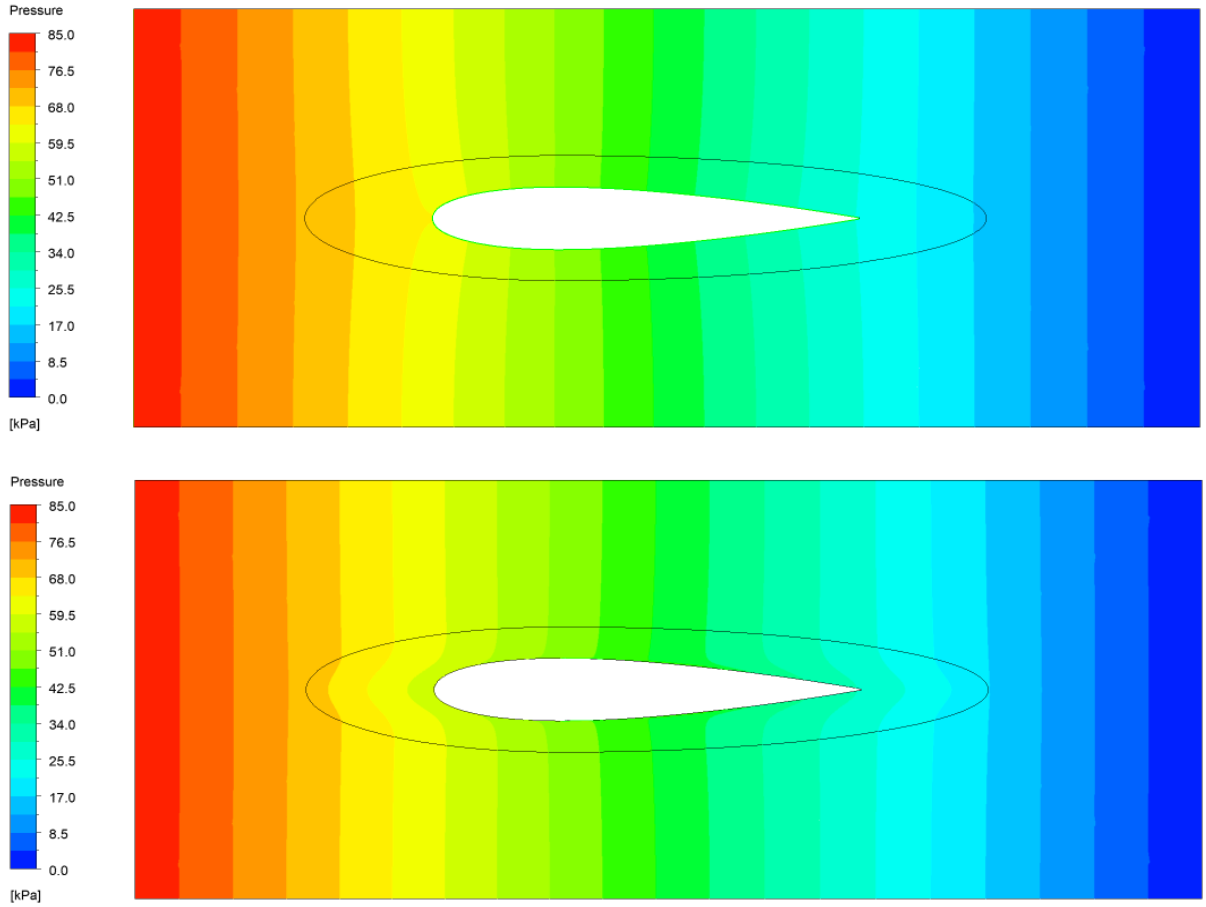

(c) The case without cloak (up) and the case with cloak (down) at Re=100

Figure 27. Pressure fields around the airfoil without and with the simplified airfoil cloak at various Reynolds numbers

Figure 28 shows the wall skin friction coefficient (C_f) on the surface of the airfoil. The C_f curves for the cases without cloak change rapidly near the leading edge and trailing edge but are smooth in the center part. However, C_f curves for the cases with cloak increases to a peak value near x=-2mm and then decreases gradually to zero and then increases again. In the trailing edge region, C_f is significantly reduced by more than 4 times before x=10mm, but only about 1.5 times after x=10mm. This distribution is caused by the geometry difference between the simplified airfoil and the original airfoil. The cloak is created for the simplified airfoil which

ends at x=10mm so the object of the original airfoil shape in the area from x=10mm to x=14mm does not have a good interaction with the cloak.

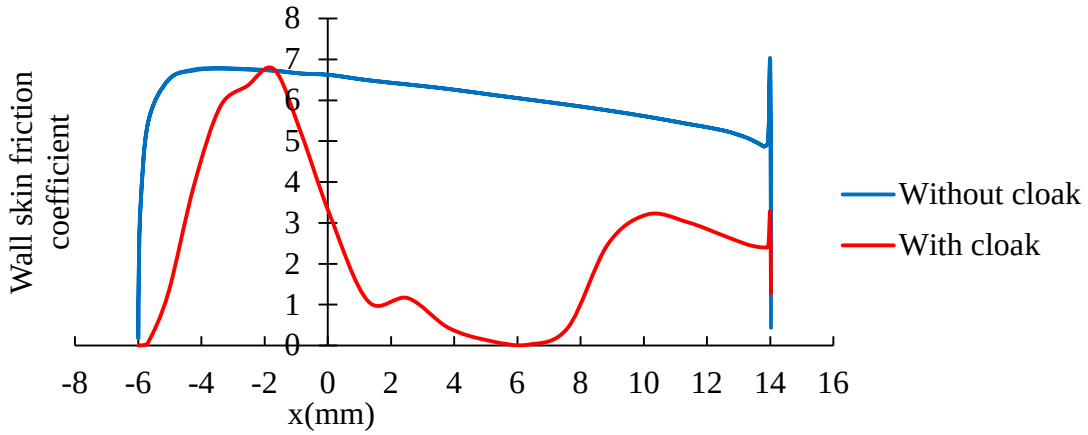

(a) Re=1

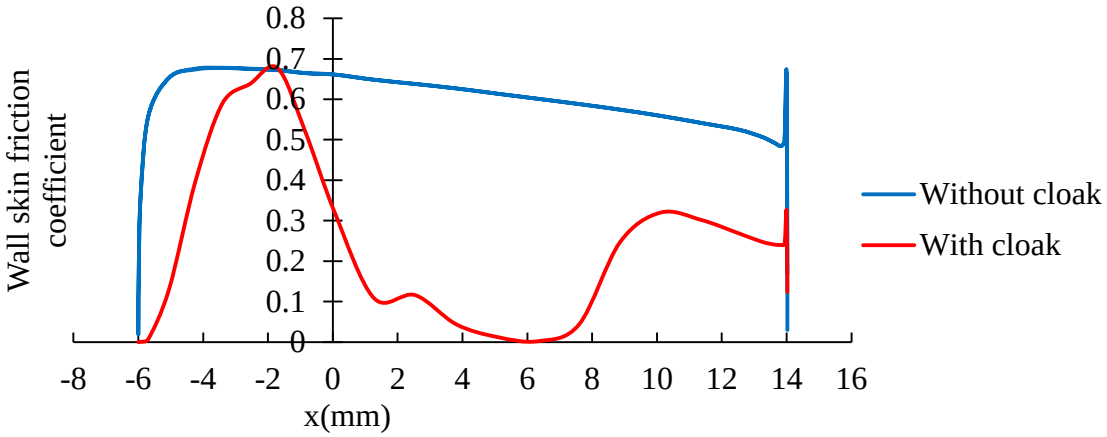

(b) Re=10

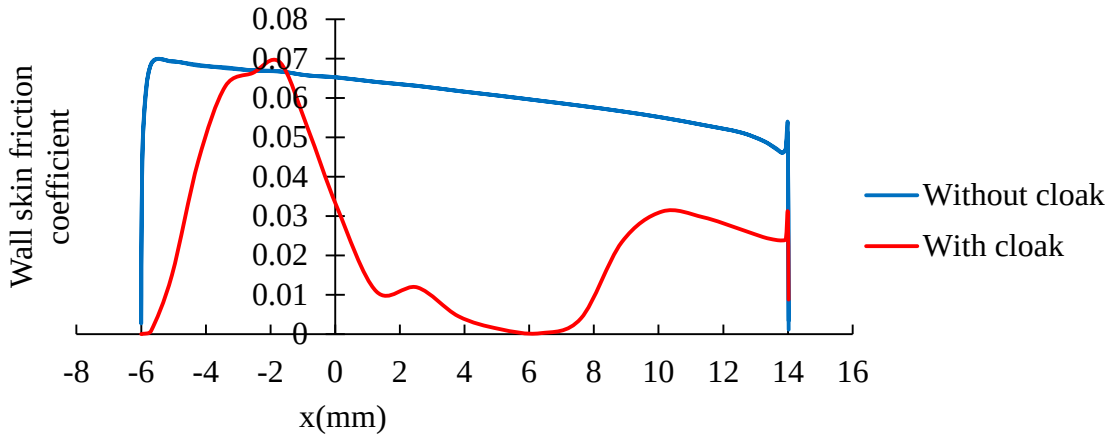

(c) Re=100

Figure 28. Wall skin friction coefficient on the airfoil surface without and with the simplified airfoil cloak at various Reynolds numbers

Table 11 shows the drag force on the airfoil without and with the simplified airfoil cloak at various Reynolds numbers. Affected by the cloak, the pressure force is reduced by about 1.5 times and the viscous force is reduced by about 3 times, and the total drag force is reduced by about 1.5 times compared to those without cloak.

Table 11 Drag force on the airfoil without and with the simplified airfoil cloak at various Reynolds numbers

Re	Pressure Force(μN)		Viscous Force(μN)		Total Drag Force(μN)	
	Without Cloak	With cloak	Without Cloak	With Cloak	Without Cloak	With Cloak
1	40.6	29.07	0.68	0.23	41.28	29.30
10	406	280.7	6.7	2.3	412.7	283.0
100	4040	2812	67	24	4107	2836

Thus, the drag reduction effect of the simplified airfoil cloak is significant but is weaker than elliptic-cylinder cloak described in Chapter 3. The geometric mismatch between the object (the original airfoil) and the cloak (enlarged from the simplified airfoil) reduces the performance

of the cloak. The proposed method that considers the airfoil as a simplified ellipse to derive the viscosity tensor needs to be improved.

4.3 Modeling of the Improved Airfoil HDMM Cloak for an Airfoil

4.3.1 Viscosity Tensor for the Improved Airfoil Cloak

For better performance of the airfoil HDMM cloak, the geometry of the cloak should be modified. Based on the result for the elliptic cloak in Chapter 3 and simplified airfoil cloak in Section 4.2, a method to generate an airfoil cloak is proposed in this section. The origin is set at $x' = 0.3$ ($x/l = x' - 0.3$) where l is the length of the airfoil. Therefore, the airfoil object is from $x/l = -0.3$ to $x/l = 0.7$ and the outer boundary of the cloak is from $x/l = -0.6$ to $x/l = 1.4$. The airfoil cloak is considered as a series of NACA0015 airfoil curves scaled from the origin as shown in Figure 29. The airfoil and the cloak are symmetrical about the *x*-axis.

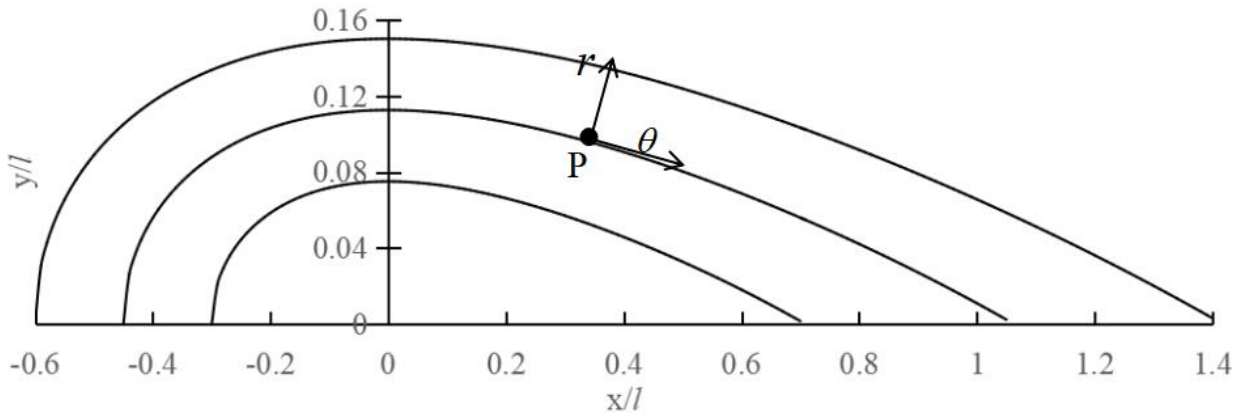

Figure 29. Geometry of NACA0015 airfoil and the airfoil cloak

In the cloak region, every point is on a unique airfoil curve scaled from the original airfoil curve based on the origin point. The direction of r and θ at point P is defined by the normal

vector and tangential vector of the airfoil curve at that point. The normal vector expression is $[y_t{}'i, j]$ where $y_t{}'$ is the first order derivative of the airfoil shape equation given as follows.

$$y_t' = \frac{dy_t}{dx'} = \frac{d5t\left[0.2969\sqrt{x'} - 0.1260x' - 0.3516x'^2 + 0.2843x'^3 - 0.1015x'^4\right]}{dx'}$$

$$= 5t\left[0.2969\frac{0.5}{\sqrt{x'}} - 0.1260 - 0.3516 \times 2x' + 0.2843 \times 3x'^2 - 0.1015 \times 4x'^3\right] \quad (34)$$

For the points on *x*-axis, the normal vector is $[i, 0]$ on the positive *x*-axis and $[-i, 0]$ on the negative *x*-axis. For the points on *y*-axis, the normal vector is $[0, i]$ on the positive *y*-axis and $[0, -1]$ on the negative *y*-axis.

For every airfoil curve in the cloak region, the scale ratio is *n*. The ratio of size of the cloak to that of the object (b/a) is 2. Similar to the viscosity tensor derivation for the elliptic cloak, the viscosity tensor for the airfoil cloak is as follows.

$$\tilde{\tilde{\mu}}'' = \begin{bmatrix} \mu''_{rr} & \mu''_{r\theta} \\ \mu''_{\theta r} & \mu''_{\theta\theta} \end{bmatrix} = c \begin{bmatrix} \left(\frac{b-a}{b}\right)^2 \left(\frac{n}{n-1}\right)^2 & 0 \\ 0 & \left(\frac{b-a}{b}\right)^2 \end{bmatrix} \mu \quad (35)$$

4.3.2 Simulation Model of the Improved Airfoil Cloak

Figure 30 shows the simulation model and the boundary conditions of the improved airfoil cloak. The simulation model is a 50mm*20mm*50μm channel with an airfoil object. The total length of the airfoil is 20mm. The origin is set at $x' = 0.3$. The improved airfoil- like cloak is proportional enlarged from the airfoil shape curve based on the origin point. The size of the cloak is 2 times the airfoil. The width of the improved airfoil cloak is 5.7mm. The length of the improved airfoil cloak is 12mm for the leading part and 20mm for the trailing part. The boundary conditions are the same as those for the simplified airfoil cloak in Section 4.1.

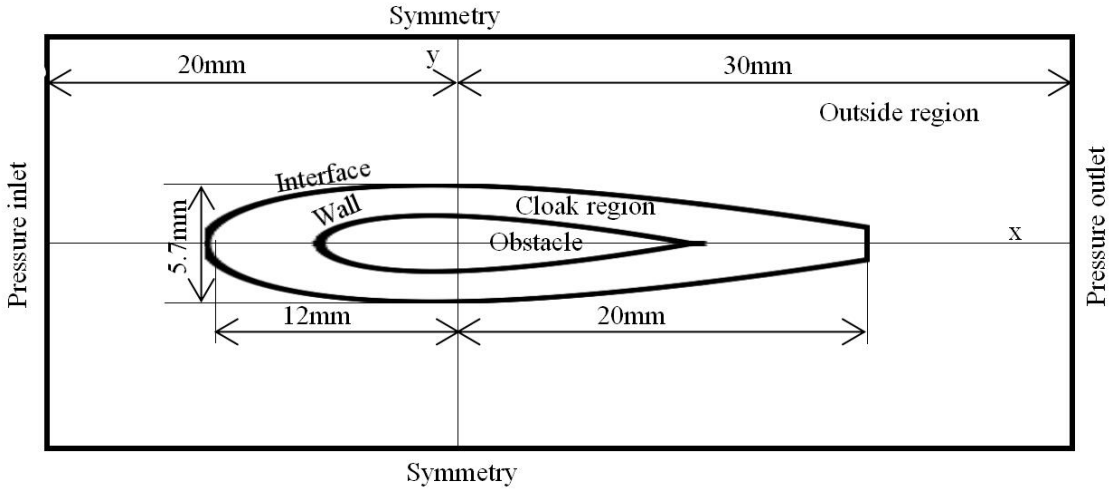

Figure 30. Simulation model for the improved airfoil cloak

The normal vector on a cylinder or elliptical object near the trailing edge has a smaller angle with *x*-axis. But the normal vector on the airfoil creates a large angle with *x*-axis in the whole trailing part region (x>0). The angle of the normal vector at the intersection point of the airfoil and *x*-axis on the positive *x*-axis is 80°. As a result, the tangent velocity of the flow from upper surface and lower surface does not neutralize each other but can merger to produce a large resultant velocity along the *x*-axis as shown in Figure 31. Thus, a high velocity area will appear near the trailing edge and becomes much higher near the end of the cloak. To improve the performance of the airfoil cloak, the part of the cloak at $x > 20mm$ is cut off as shown in Figure 30. Thus, the effect of the angle of the normal vector is reduced.

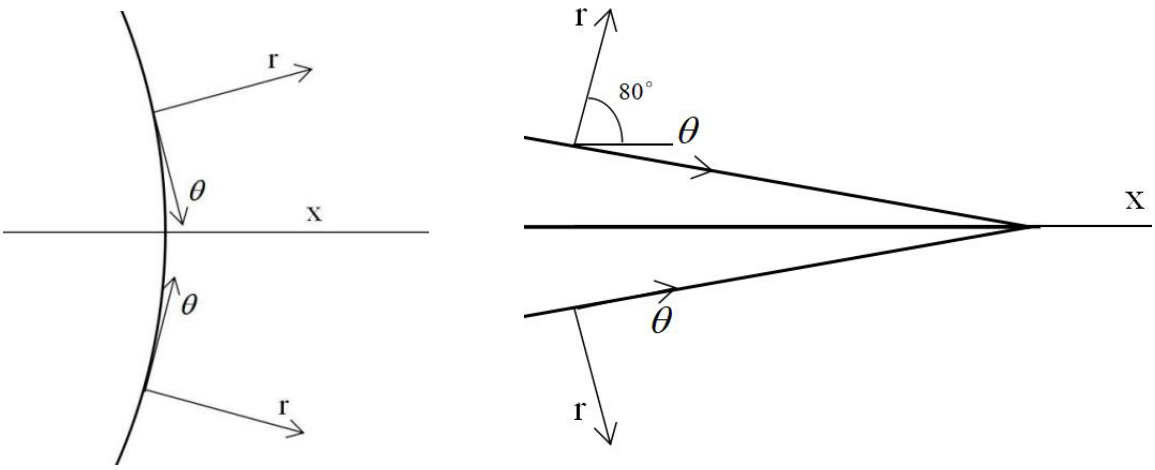

(a) Elliptical object (b) Airfoil

Figure 31. Normal vectors near the trailing edge of the elliptical object and the airfoil

The simulation cases are conducted at Re=1, 10 and 100 with angle of attack of 0, 5° and 10°. The region outside the cloak is modeled as a porous zone with the same properties as for the simplified airfoil cloak in Section 4.2 ($1/\alpha = 3.2 \times 10^9 [1/m^2]$, $C_2 = 0$). In the cloak region, the porous zone properties are as follows.

$$\frac{1}{\alpha_r} = 3.2 \times 10^9 \times \frac{1}{4} c \left(\frac{n}{n-1}\right)^2 \left[\frac{1}{m^2}\right]$$

$$\frac{1}{\alpha_\theta} = 3.2 \times 10^9 \times \frac{1}{4} c \left[\frac{1}{m^2}\right]$$

$$C_2 = 0$$

where *n* is determined by the mesh point position and is calculated by a UDF used in FLUENT.

Factor c is obtained to find the best performance for the improved airfoil cloak at Re=1. Both hydrodynamic hiding effect and drag reduction effect are analyzed to evaluate the influence of factor c. Figure 32 shows the velocity fields around the airfoil with the improved airfoil cloak for various values of c. With higher value of c, the velocity in the region outside the cloak is more uniform.

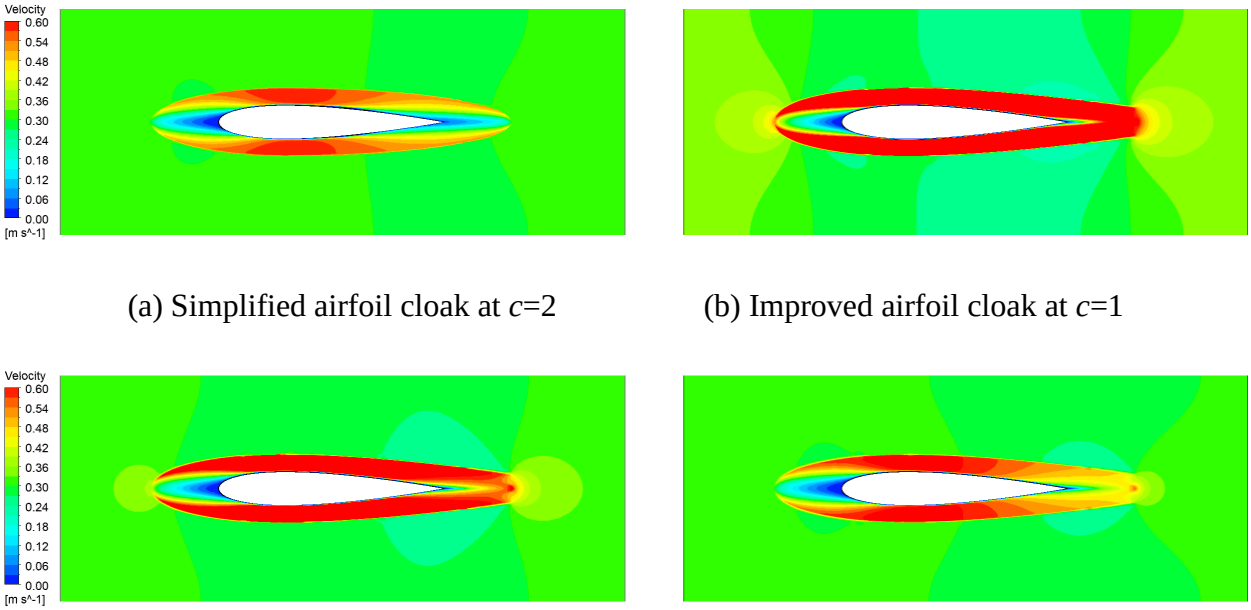

(a) Simplified airfoil cloak at c=2 (b) Improved airfoil cloak at c=1

(c) Improved airfoil cloak at c=1.5 (d) Improved airfoil cloak at c=2

Figure 32. Velocity fields around the airfoil with the improved airfoil cloak for different values of factor c

Figure 33 shows the outlet velocity profiles for the flow with the simplified airfoil cloak and with the improved airfoil cloak for various values of factor c. In the improved airfoil cloak cases with c=1 and c=1.5, the outlet velocity is larger near the center line because the effect of the angle of the normal vector in the trailing edge part still exists. The case with a bigger c value has an outlet velocity profile closer to the theoretical velocity in the bare channel, but the simplified airfoil cloak case provides the best outlet velocity.

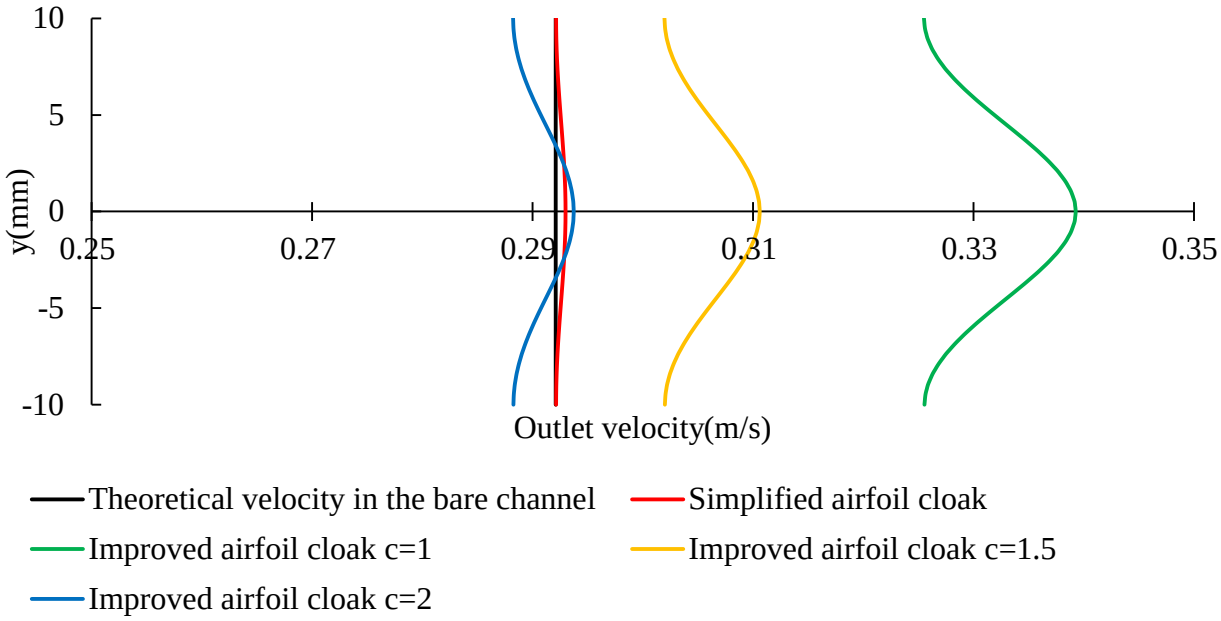

Figure 33. Comparison of outlet velocity profiles for the airfoil with the simplified airfoil cloak and with the improved airfoil cloak for various values of c

Figure 34 shows the wall skin friction coefficient (C_f) on the airfoil surface without cloak, with the simplified airfoil cloak and with the improved airfoil cloak for various values of c. All improved airfoil cloak cases have smaller C_f on the whole surface than the case without cloak and have smaller C_f than the simplified case in the area x>8mm. The peaks of the improved airfoil cloak cases are in the area from 0mm to 3mm, which is farther from the leading edge than the simplified airfoil cloak case. C_f is smaller for the case for larger c value for improved airfoil cloak.

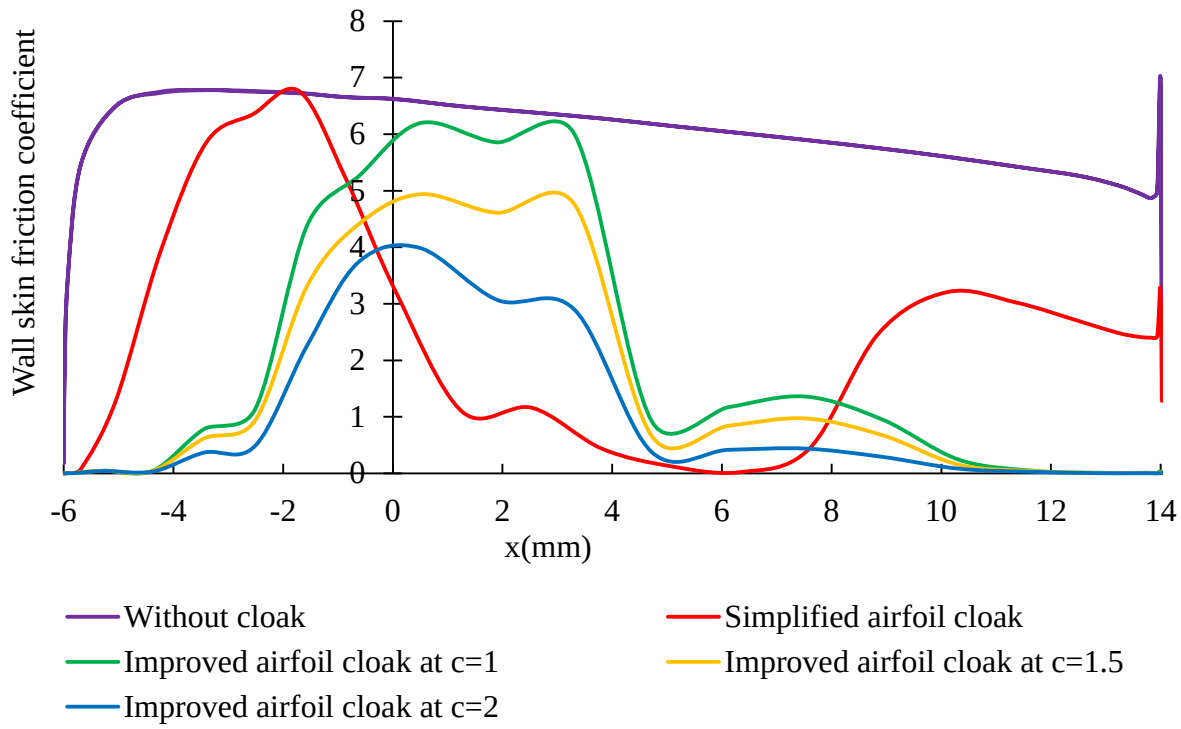

Figure 34. Wall skin friction coefficient on the airfoil surface without cloak, with the simplified airfoil cloak and with the improved airfoil cloak

Table 12 shows the drag force on the airfoil without cloak, with the simplified airfoil cloak and with the improved airfoil cloak for various values of c. The pressure force increases with increase in the value of c, but the viscous force is reduced at higher c.

Table 12 Drag force on the airfoil with the simplified airfoil cloak and with the improved airfoil cloak for various value of factor c

c	Pressure Force(μN)	Viscous Force(μN)	Total Drag Force(μN)
1	25.10	0.22	25.32
1.5	27.25	0.17	27.42
2	28.20	0.12	28.32
Simplified airfoil cloak	29.07	0.23	29.30

The improved airfoil cloak has the hydrodynamic hiding effect closer to the simplified airfoil cloak at c=2 and has worse performance at smaller value of c. It improves the drag reduction effect, and larger value of c has better effect. Considering both effects of the cloak, the factor c is set as 2 in the following airfoil simulation cases.

4.4 Evaluation of the Effect of the Improved Airfoil HDMM Cloak on an Airfoil

4.4.1 Evaluation of Hydrodynamic Hiding Effect

Velocity fields and streamlines are analyzed to evaluate the hydrodynamic hiding effect of the improved airfoil HDMM cloak. Figures 35, 36 and 37 show the velocity fields around the airfoil without and with the improved airfoil cloak cases at 0, 5° and 10° angles of attack respectively at Re=1, 10 and 100. The high velocity areas near both upper and lower surfaces are enlarged by the presence of the cloak. The velocity field changes proportionally with Re. The increase in the angle of attack moves the high velocity areas to upstream on the upper surface and downstream on the lower surface. The velocity in the region outside the cloak becomes less uniform at higher angle of attack.

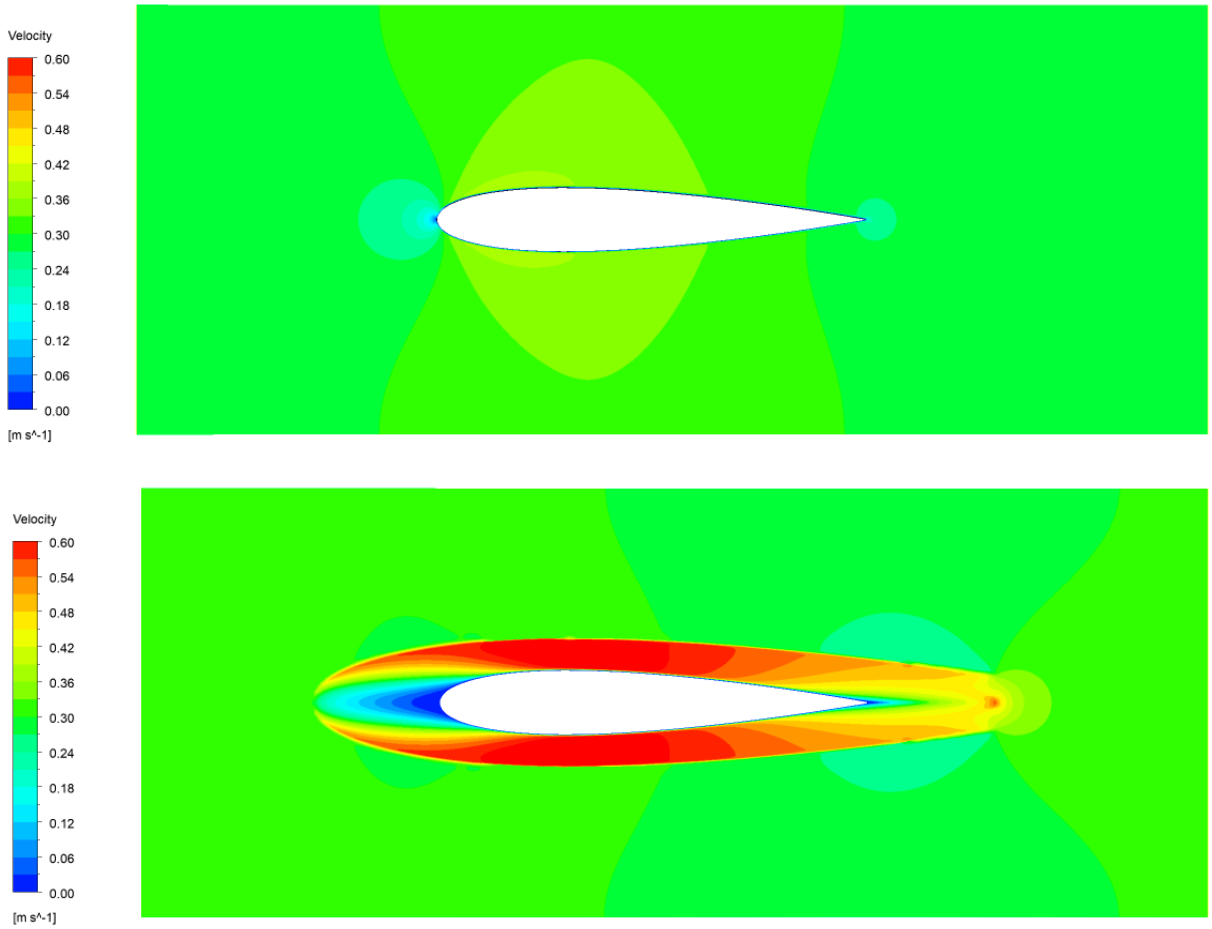

(a) The case without cloak (up) and the case with cloak (down) at Re=1

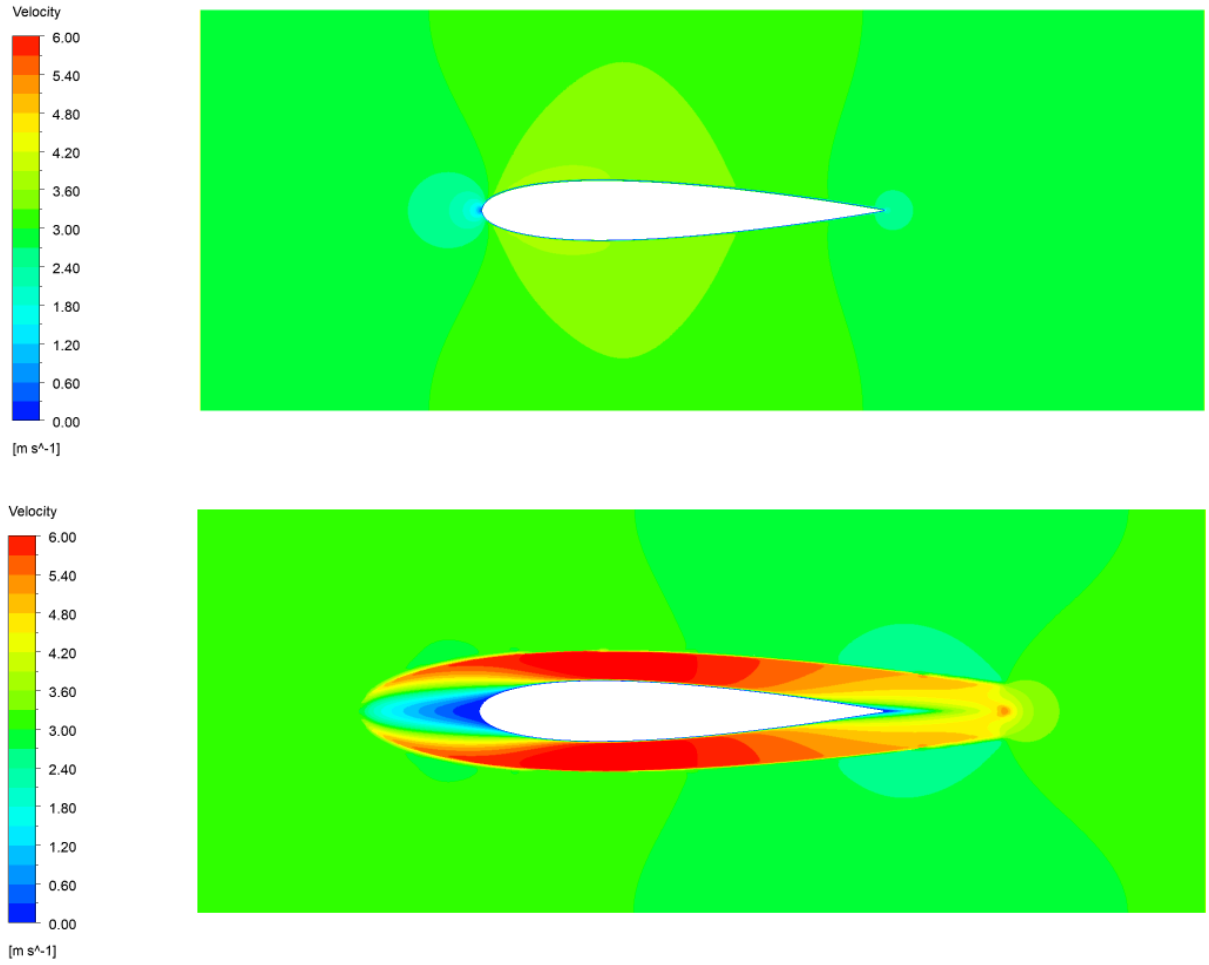

(b) The case without cloak (up) and the case with cloak (down) at Re=10

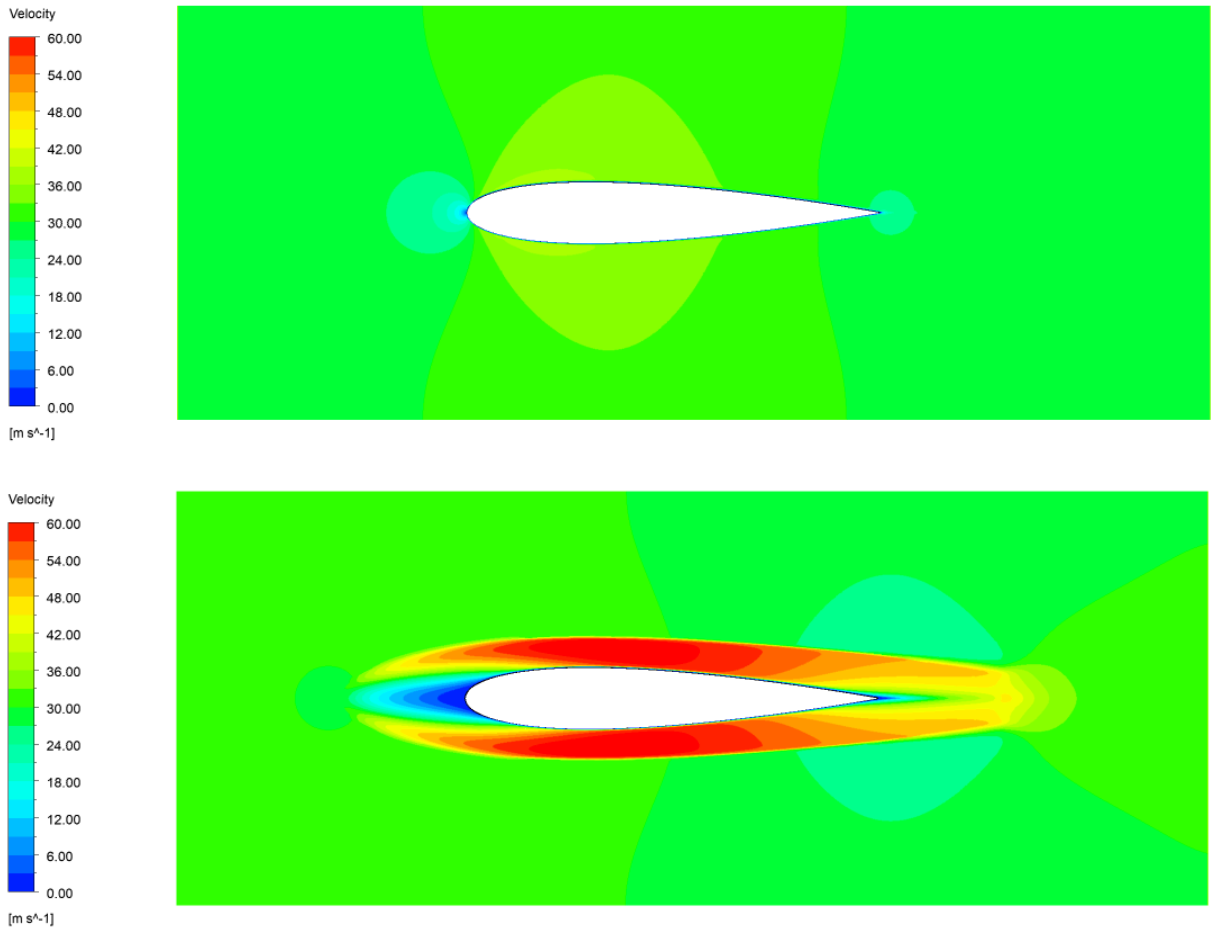

(c) The case without cloak (up) and the case with cloak (down) at Re=100

Figure 35. Velocity fields around the airfoil without and with the improved airfoil cloak at 0° angle of attack for different Reynolds numbers

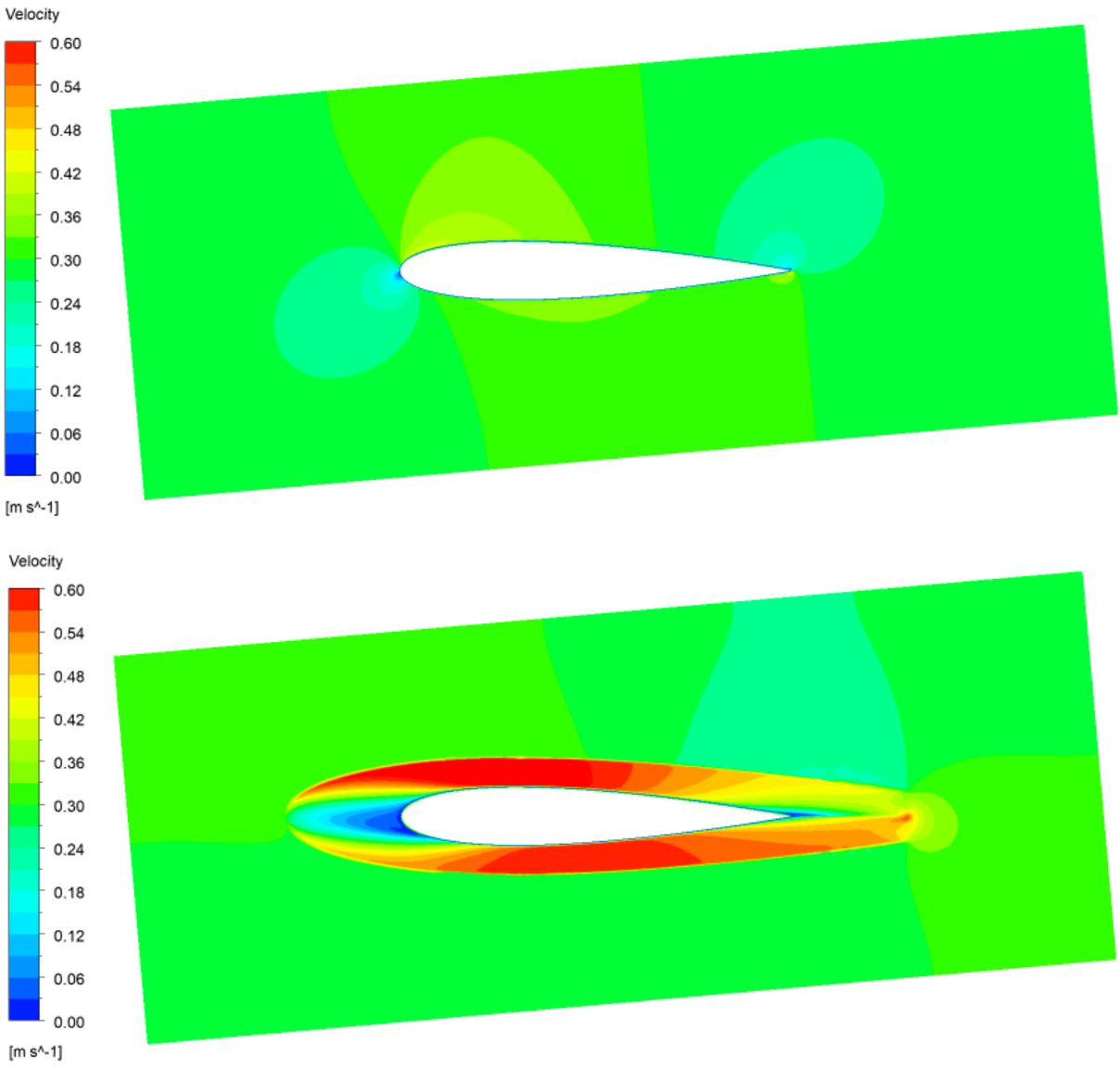

(a) The case without cloak (up) and the case with cloak (down) at Re=1

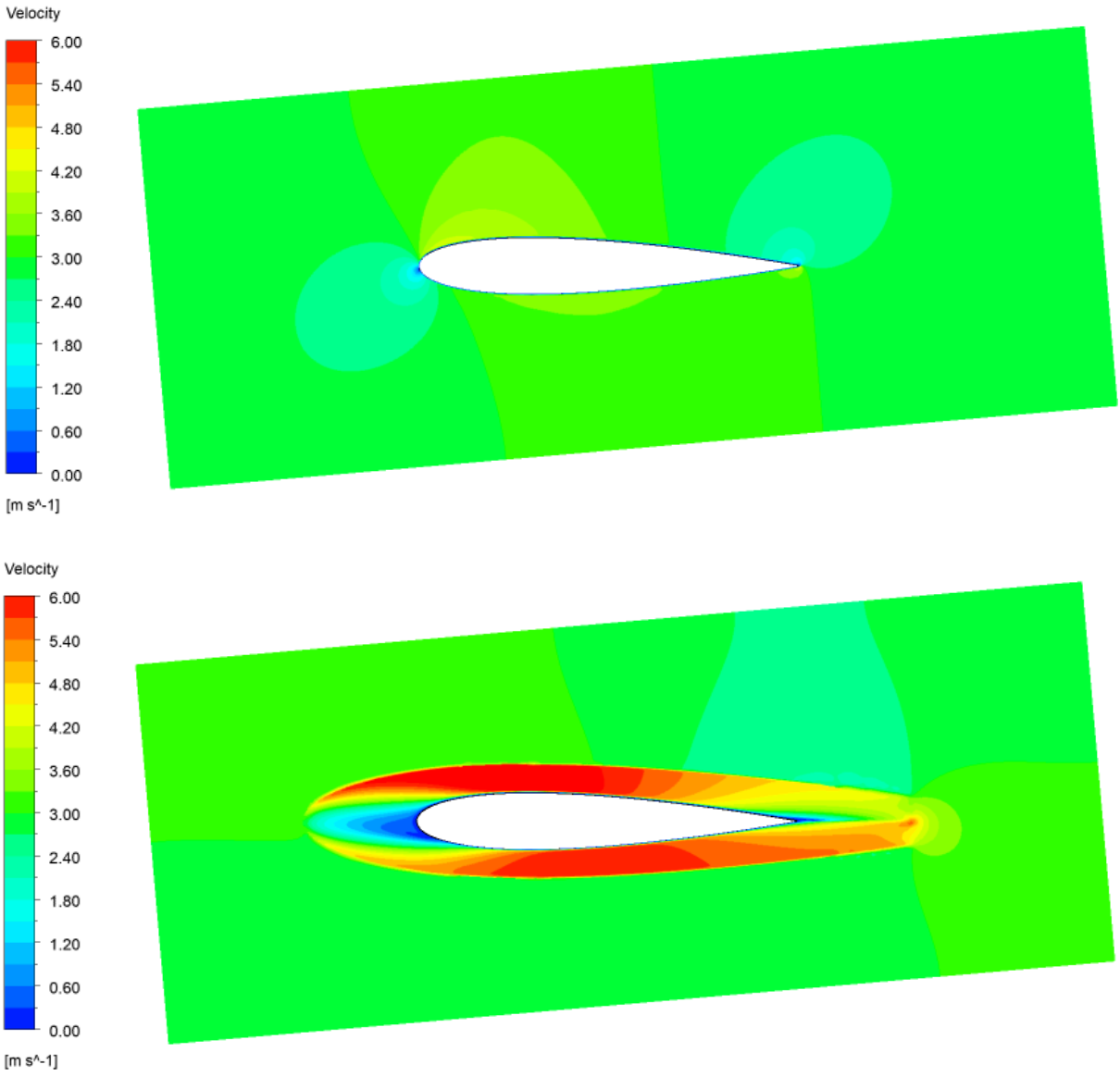

(b) The case without cloak (up) and the case with cloak (down) at Re=10

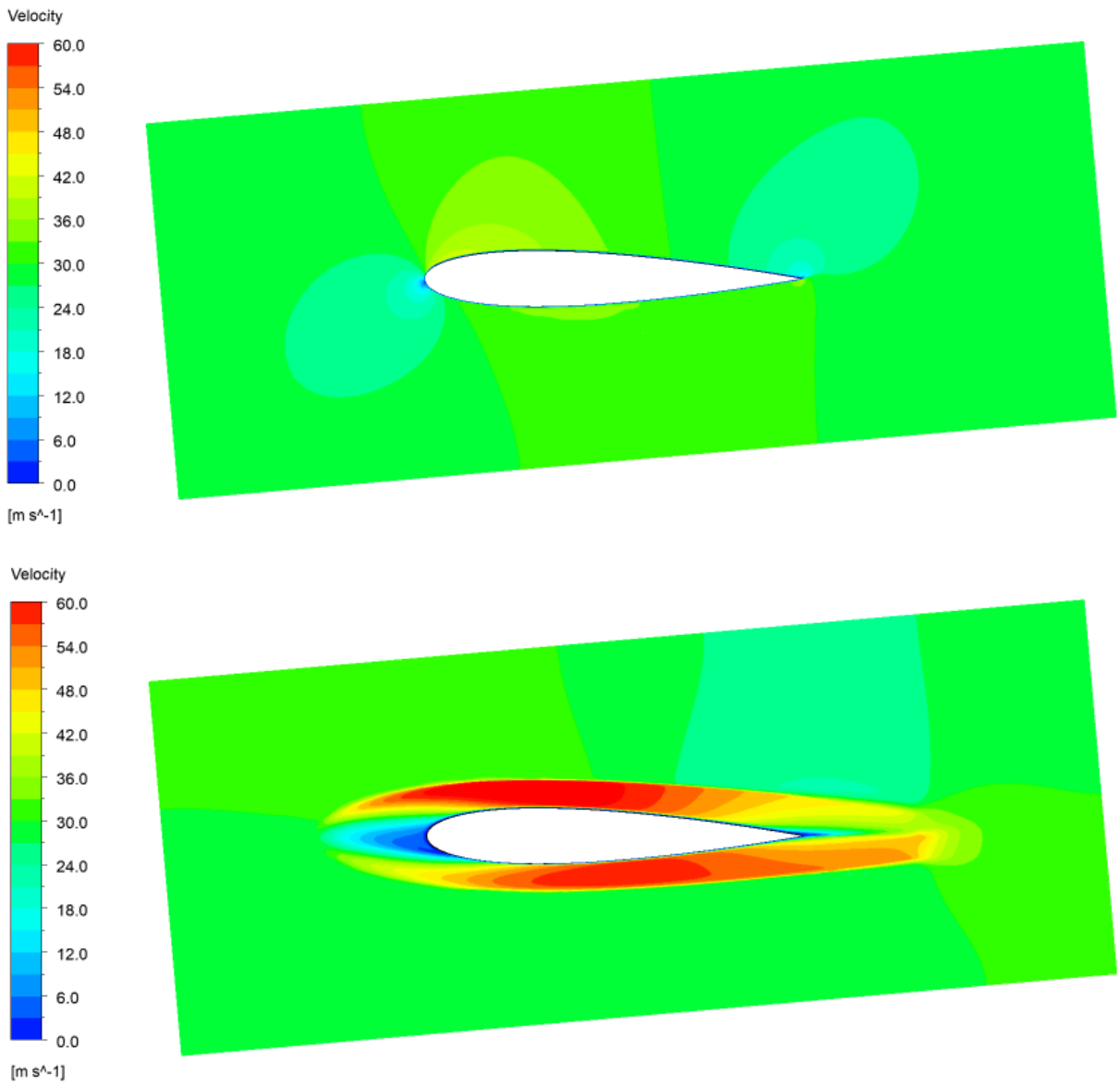

(c) The case without cloak (up) and the case with cloak (down) at Re=100

Figure 36. Velocity fields around the airfoil without and with the improved airfoil cloak at 5° angle of attack for different Reynolds numbers

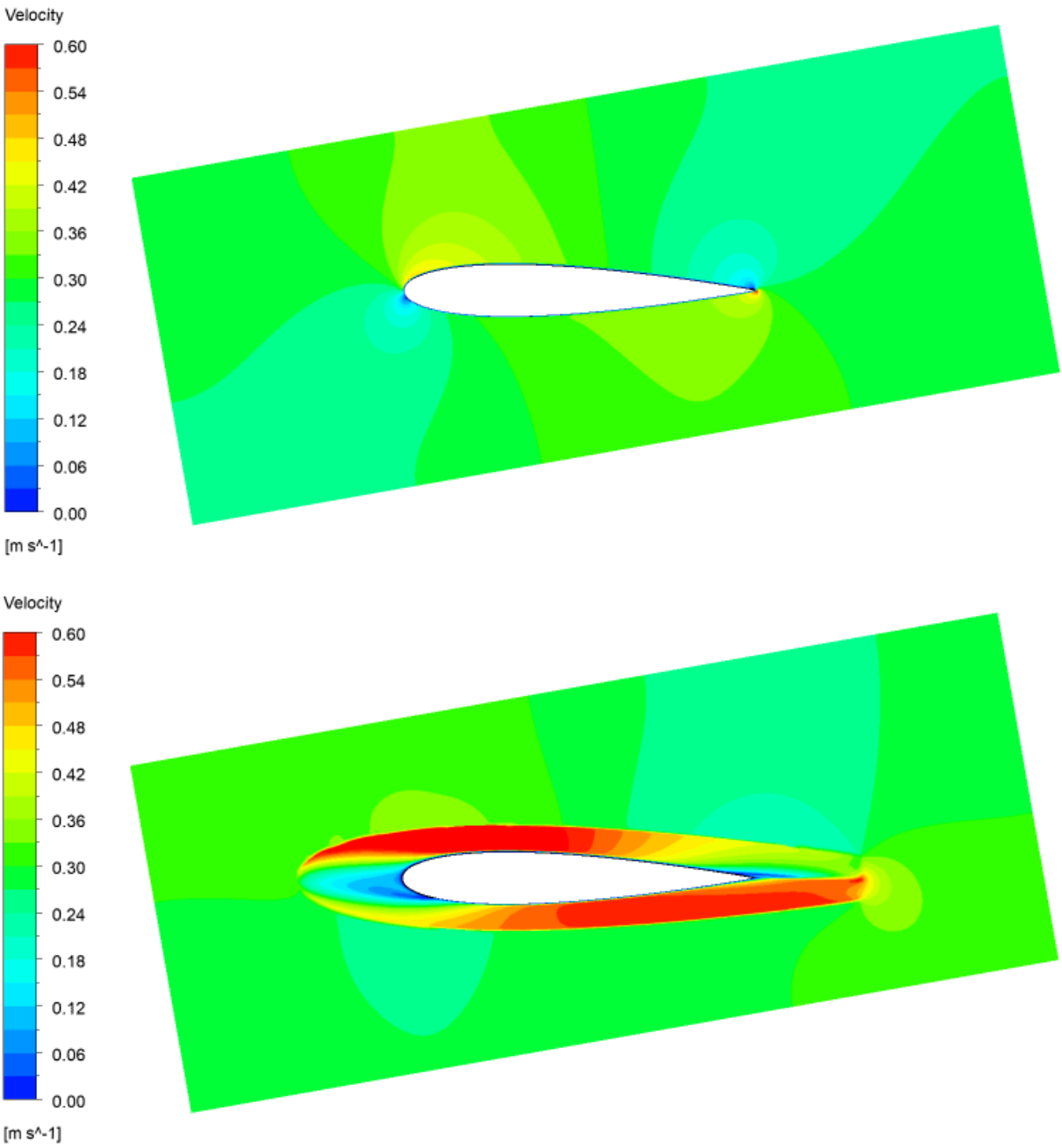

(a) The case without cloak (up) and the case with cloak (down) at Re=1

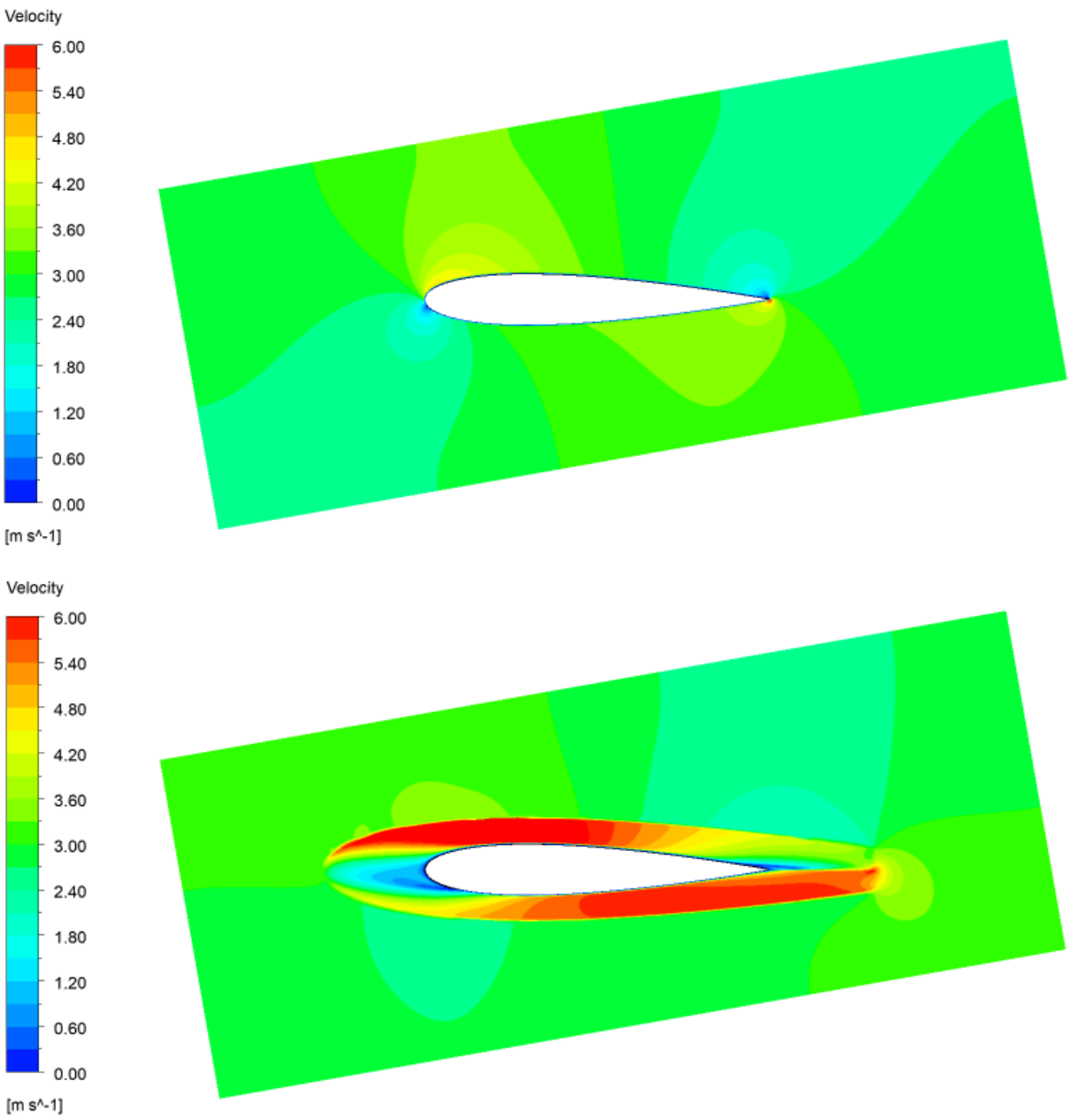

(b) The case without cloak (up) and the case with cloak (down) at Re=10

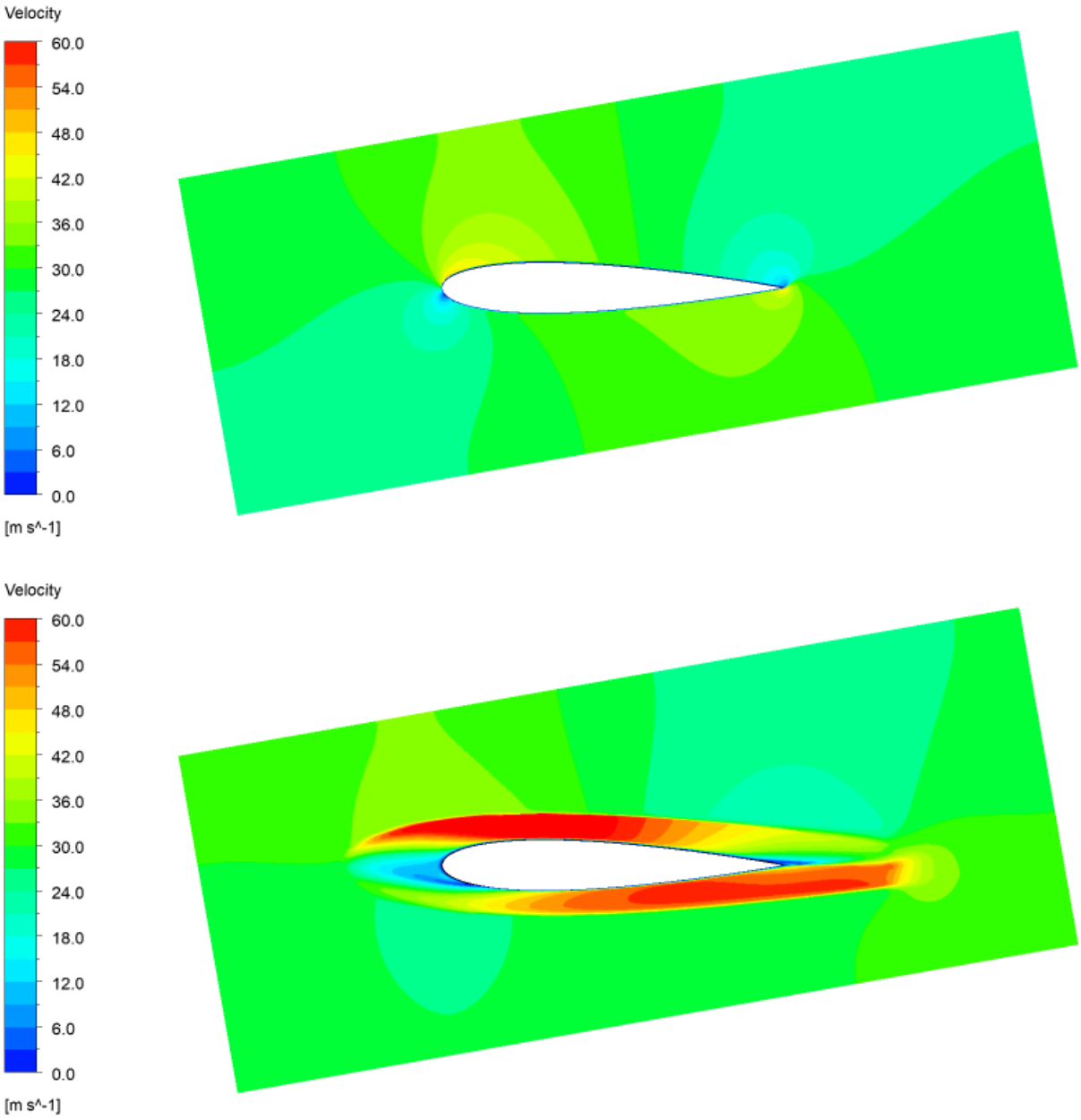

(c) The case without cloak (up) and the case with cloak (down) at Re=100

Figure 37. Velocity fields around the airfoil without and with the improved airfoil cloak at 10° angle of attack for different Reynolds numbers

Figures 38, 39 and 40 show the streamlines around the airfoil without and with the improved airfoil cloak for different Reynolds numbers and angles of attack. Affected by the

cloak, the streamlines on both sides of the airfoil and in the region outside the cloak are straighter but are distorted near the end of the cloak.

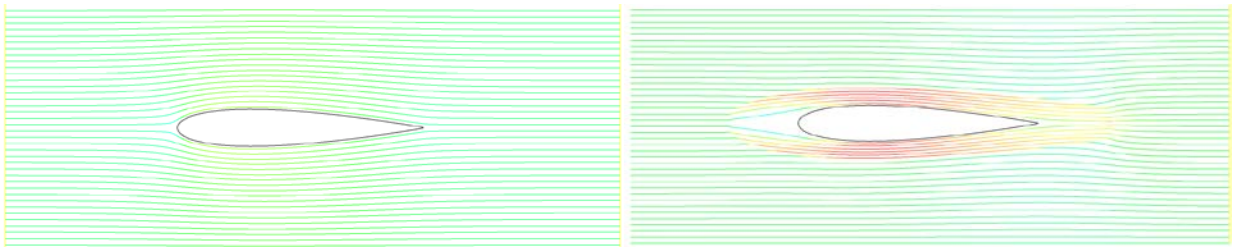

(a) The case without cloak (left) and the case with cloak (right) at Re=1

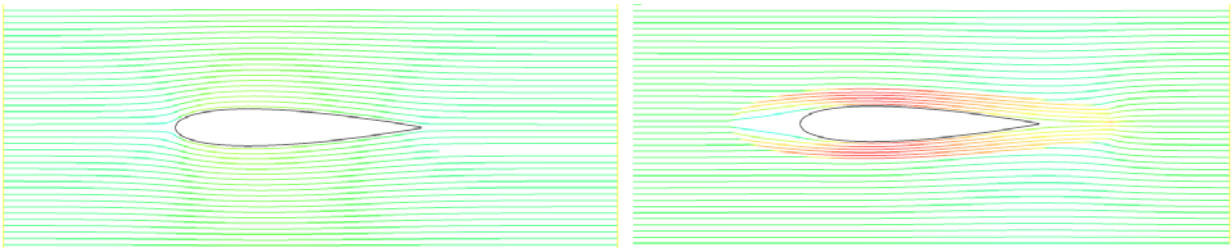

(b) The case without cloak (left) and the case with cloak (right) at Re=10

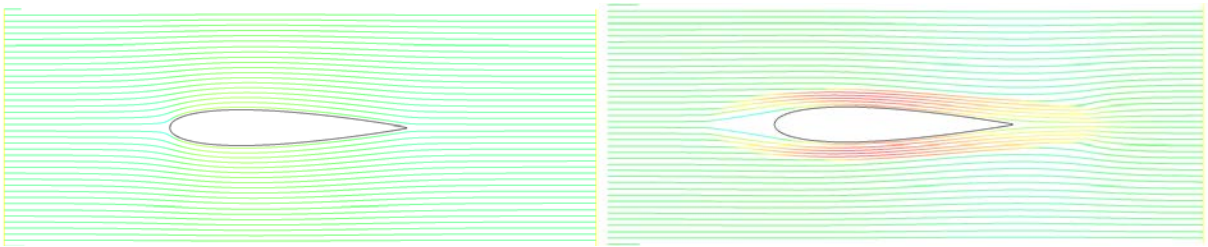

(c) The case without cloak (left) and the case with cloak (right) at Re=100

Figure 38. Streamlines around the airfoil without and with the improved airfoil cloak at 0° angle of attack for different Reynolds numbers

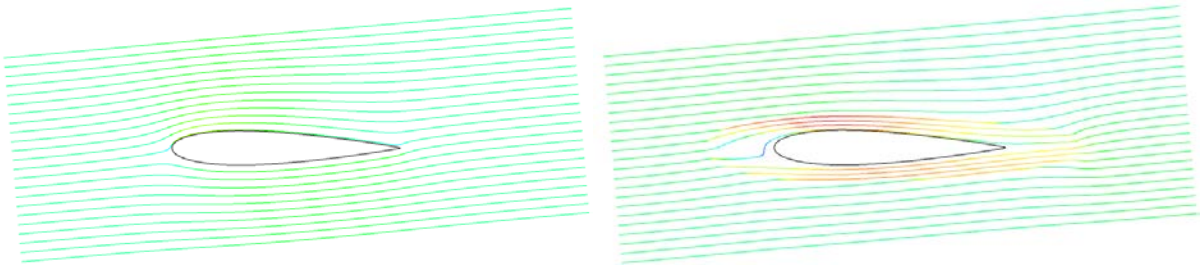

(a) The case without cloak (left) and the case with cloak (right) at Re=1

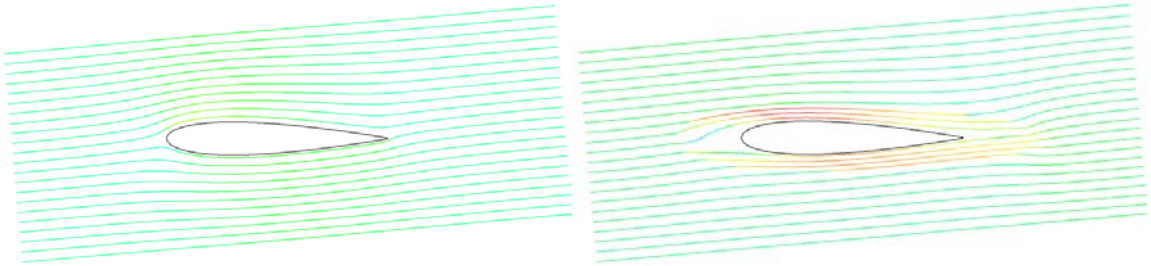

(b) The case without cloak (left) and the case with cloak (right) at Re=10

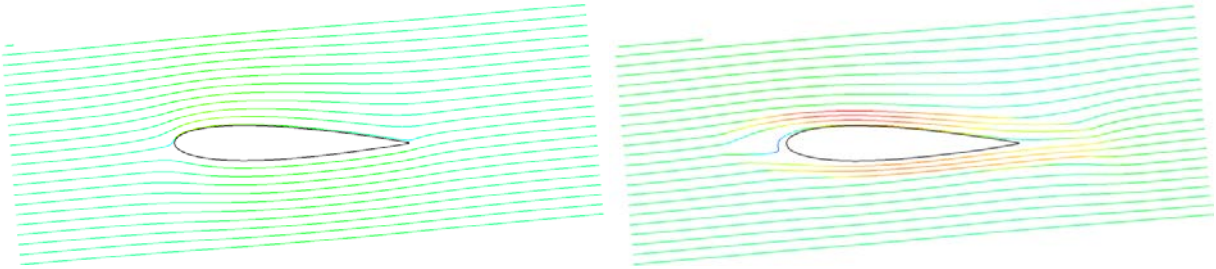

(c) The case without cloak (left) and the case with cloak (right) at Re=100

Figure 39. Streamlines around the airfoil without and with the improved airfoil cloak at 5° angle of attack for different Reynolds numbers

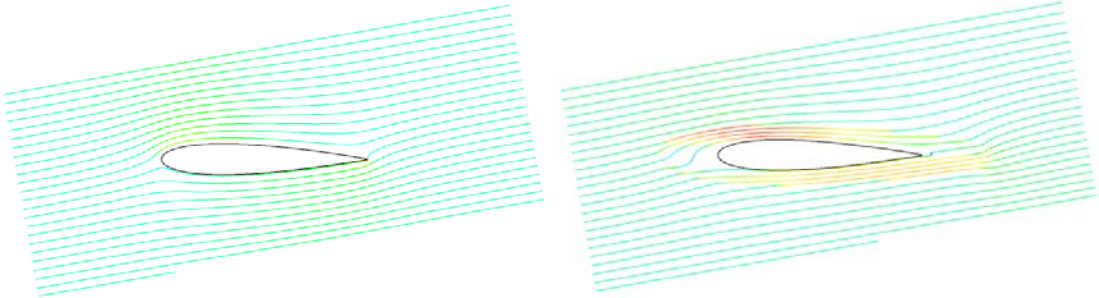

(a) The case without cloak (left) and the case with cloak (right) at Re=1

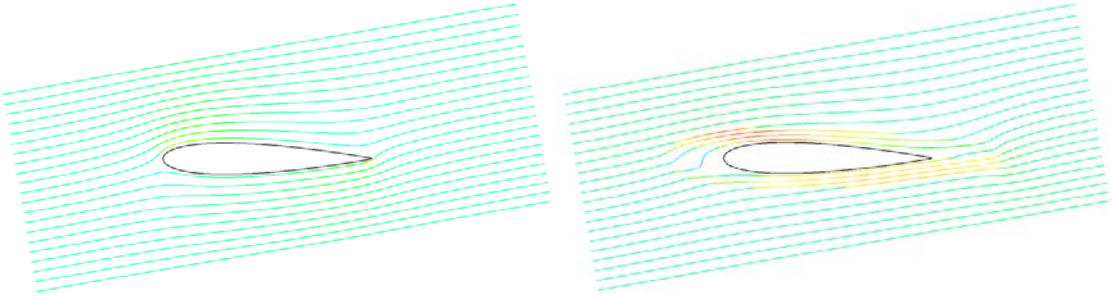

(b) The case without cloak (left) and the case with cloak (right) at Re=10

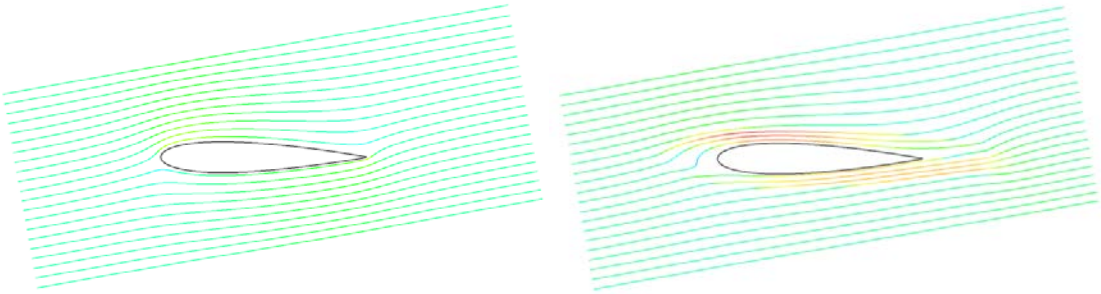

(c) The case without cloak (left) and the case with cloak (right) at Re=100

Figure 40. Streamlines around the airfoil without and with the improved airfoil cloak at 10° angle of attack for different Reynolds numbers

Thus, the improved airfoil cloak has good hydrodynamic hiding effect on both sides of the airfoil but shows poor performance near the end of the cloak. The reason is that the cloak does not provide a smooth transition from the cloak region to the region outside the cloak at the end of the cloak.

4.4.2 Evaluation of Drag Reduction Effect

Figures 41, 42 and 43 show the pressure fields around the airfoil without and with the improved airfoil cloak at different Reynolds numbers at various angles of attack respectively. The pressure difference is reduced by the cloak compared to without cloak in all cases. When the angle of attack increases, the pressure contours become asymmetric about the *x*-axis.

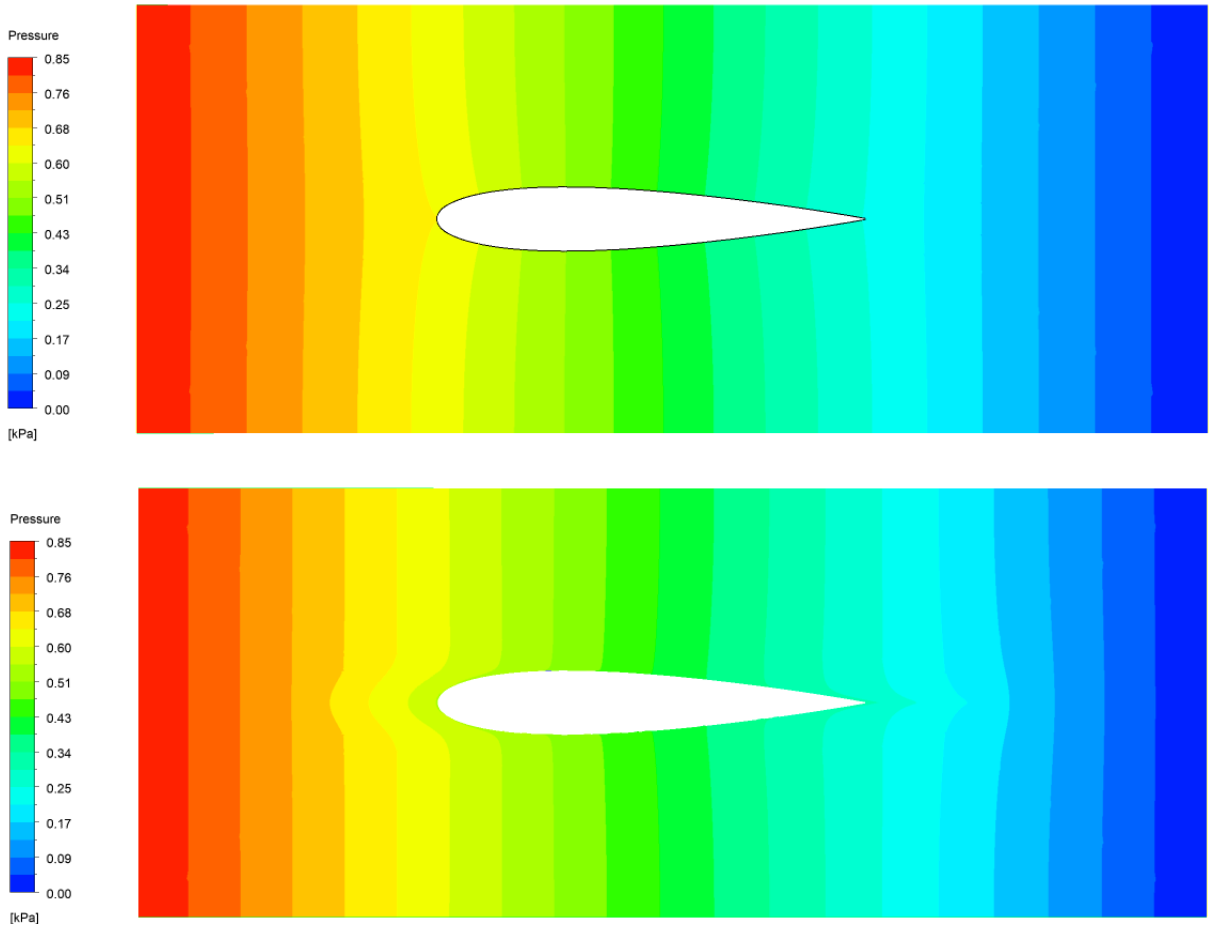

(a) The case without cloak (up) and the case with cloak (down) at Re=1

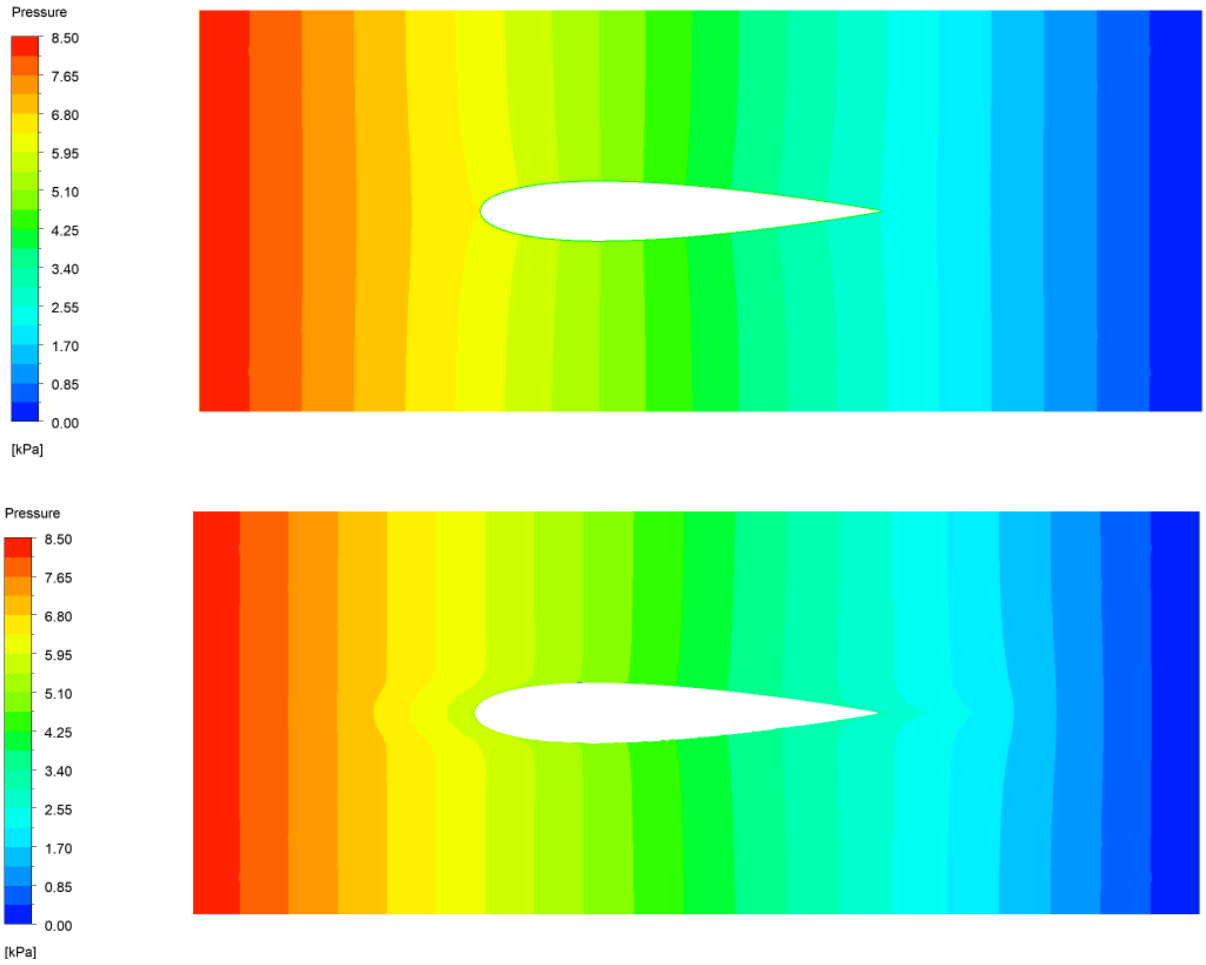

(b) The case without cloak (up) and the case with cloak (down) at Re=10

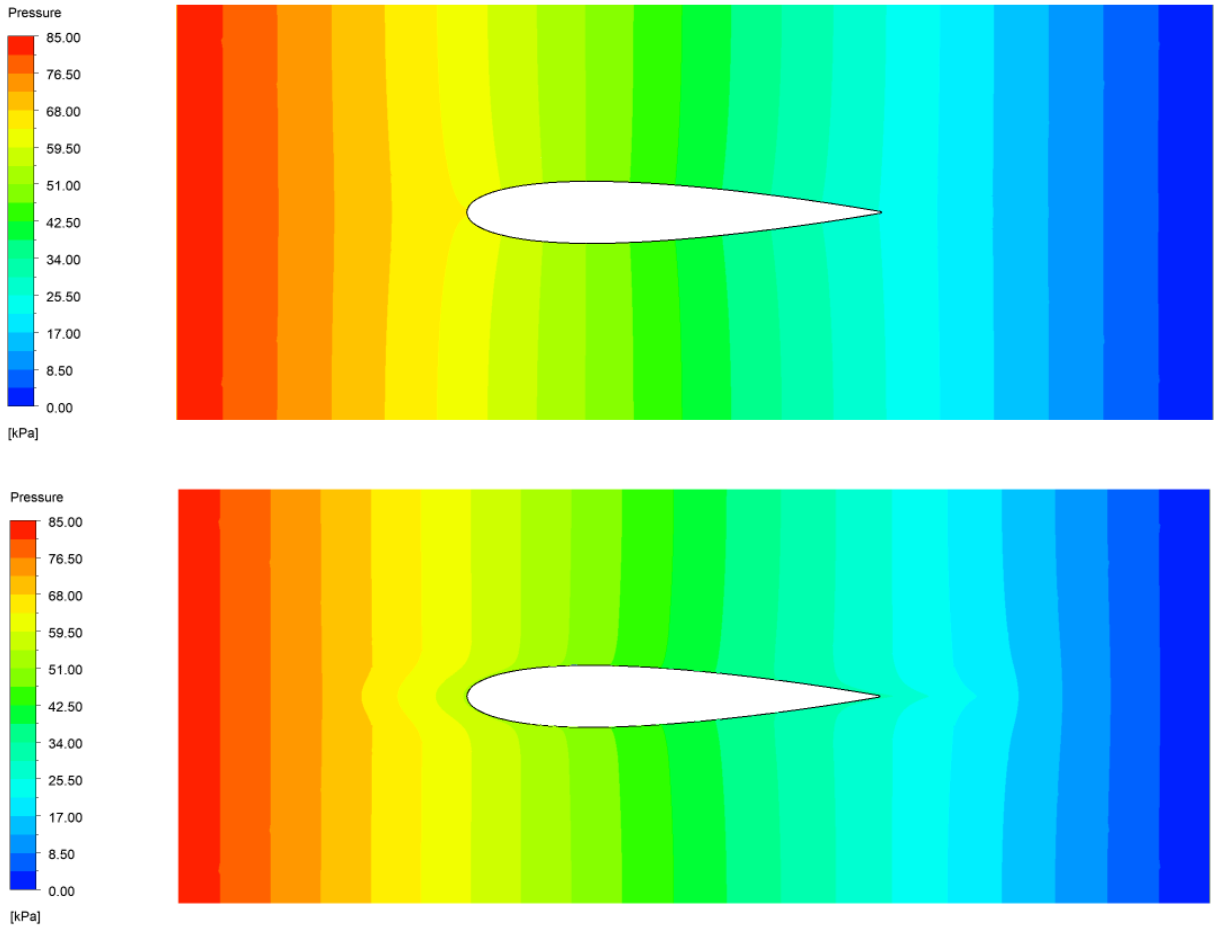

(c) The case without cloak (up) and the case with cloak (down) at Re=100

Figure 41. Pressure fields around the airfoil without and with the improved airfoil cloak cases at 0° angle of attack for different Reynolds numbers

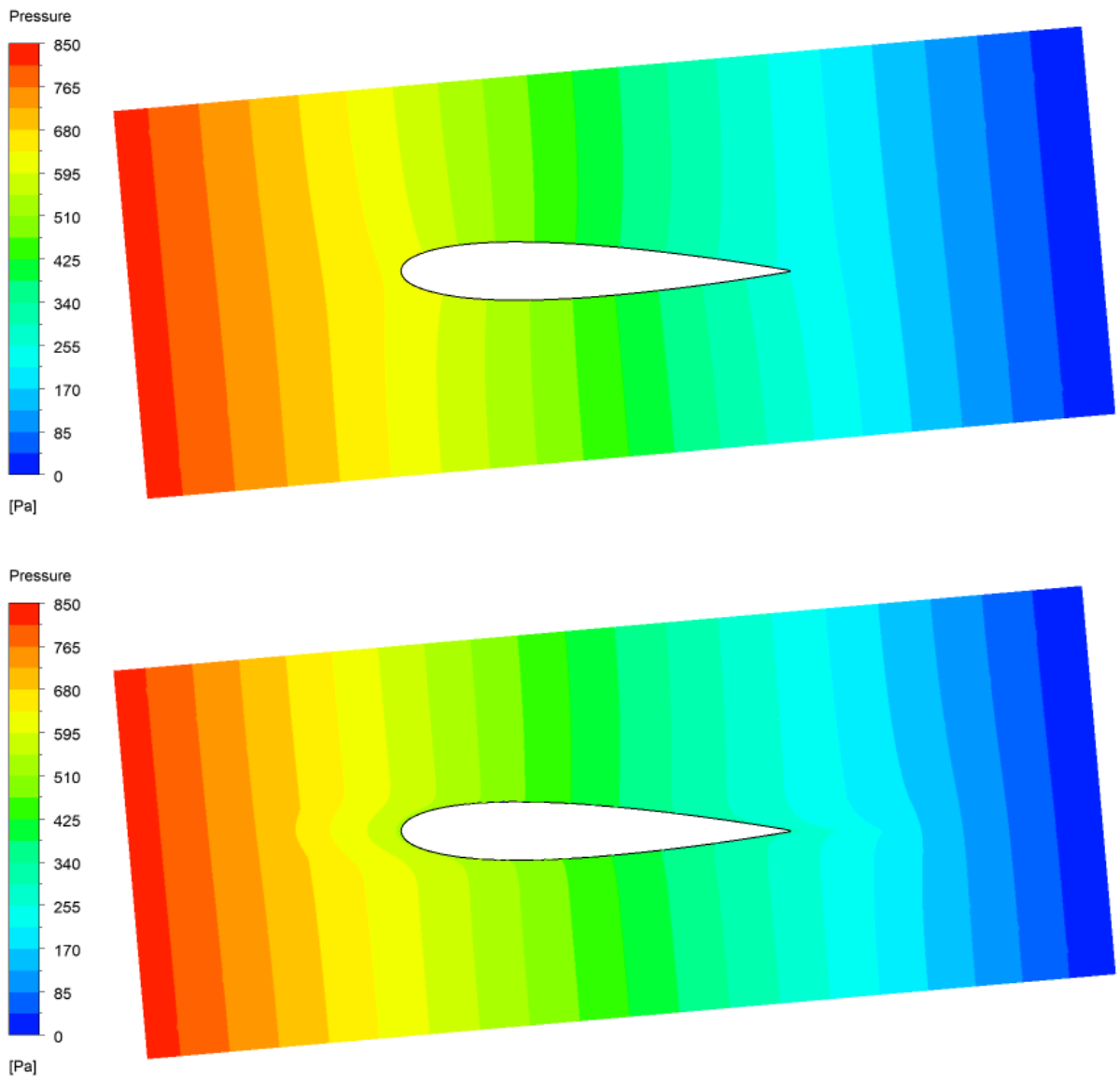

(a) The case without cloak (up) and the case with cloak (down) at Re=1

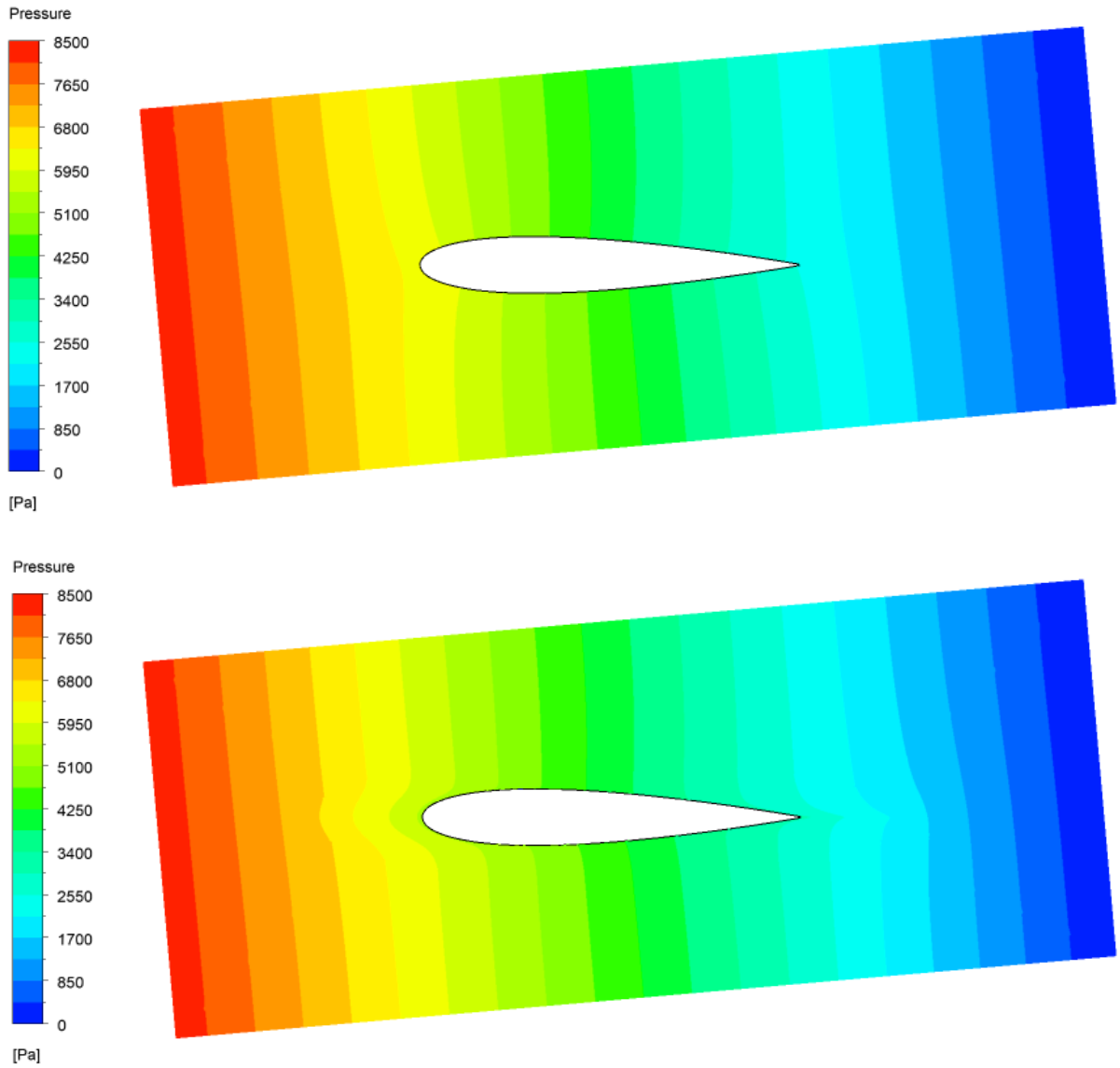

(b) The case without cloak (up) and the case with cloak (down) at Re=10

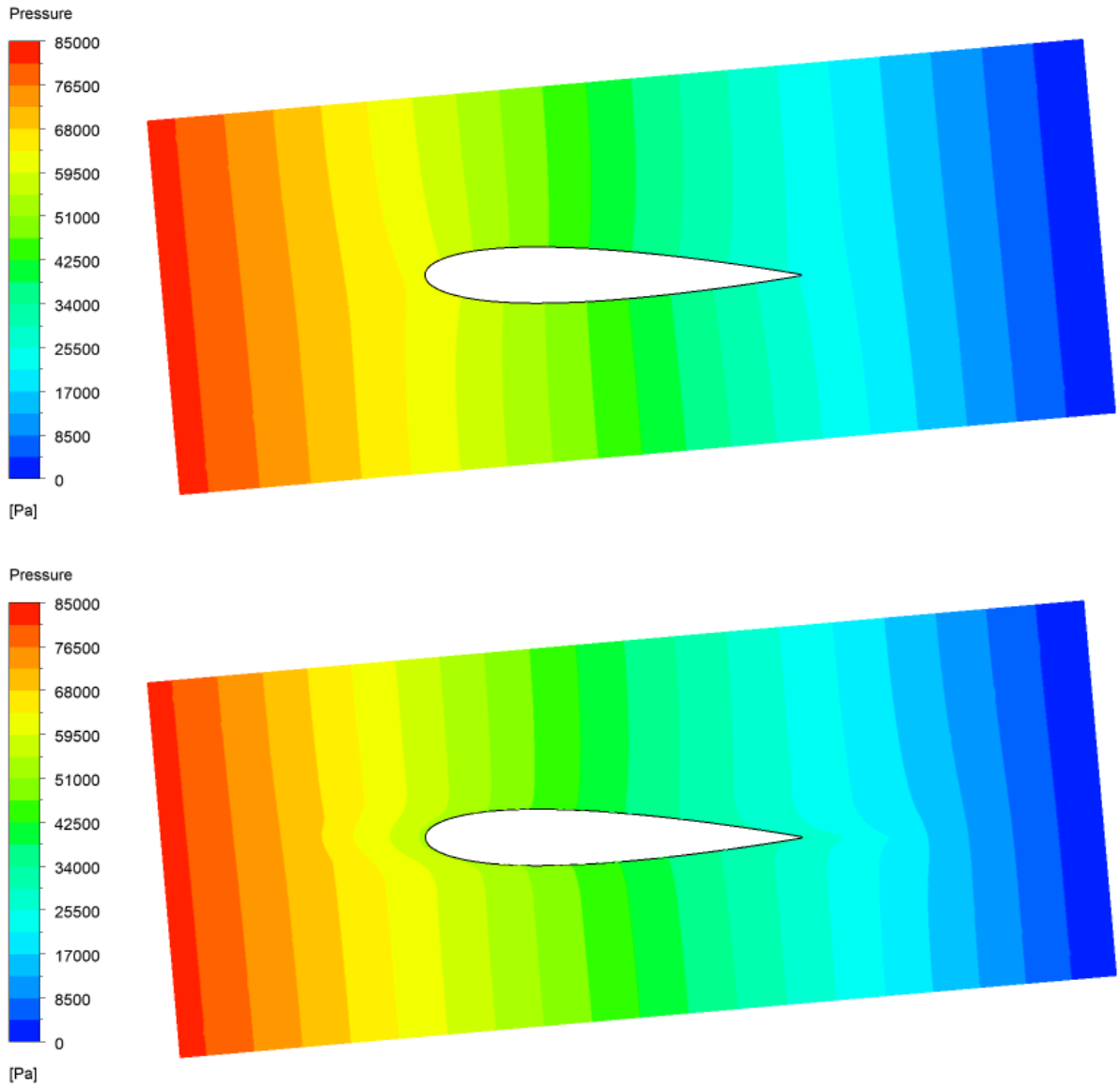

(c) The case without cloak (up) and the case with cloak (down) at Re=100

Figure 42. Pressure fields around the airfoil without and with the improved airfoil cloak cases at 5° angle of attack for different Reynolds numbers

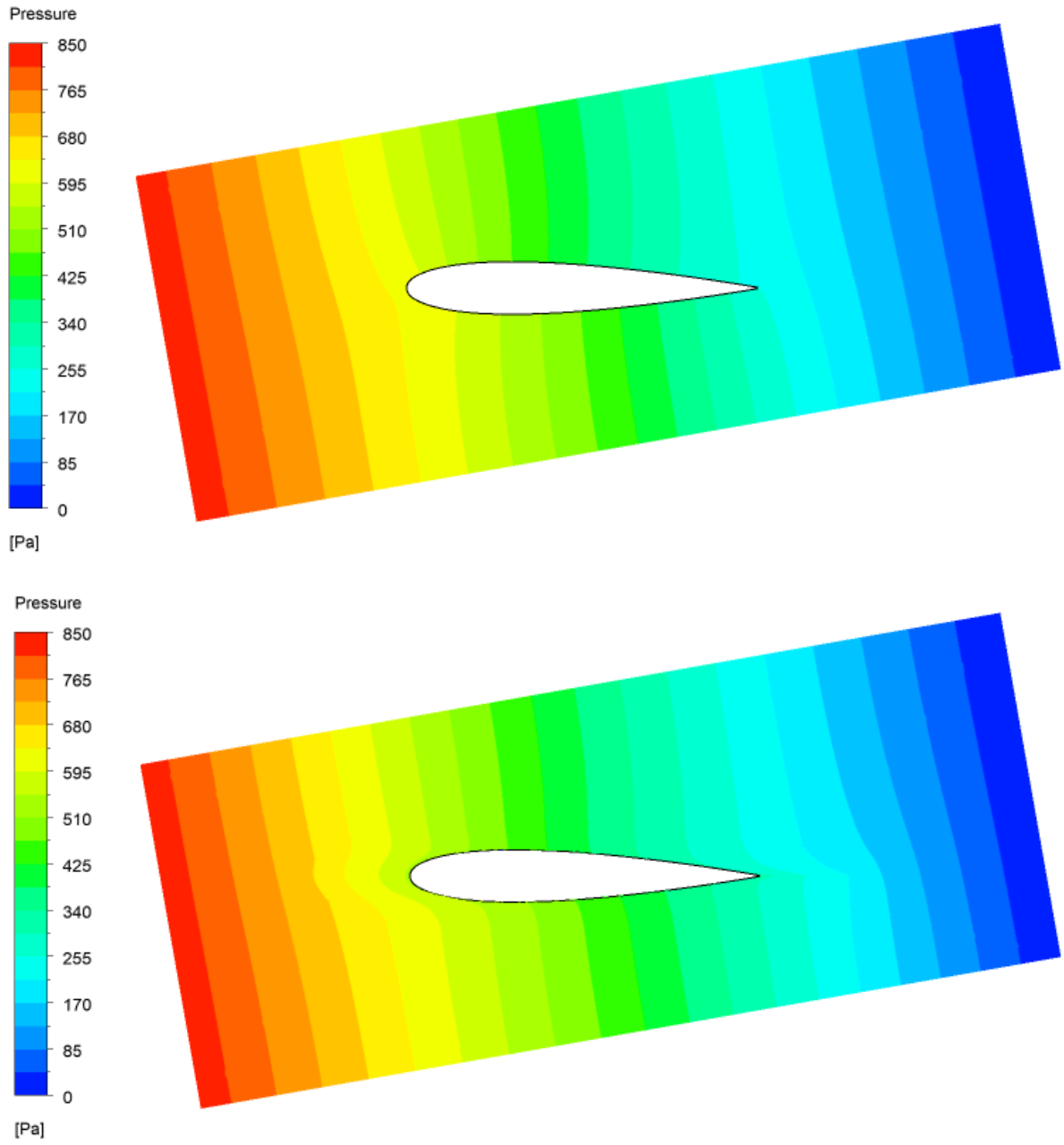

(a) The case without cloak (up) and the case with cloak (down) at Re=1

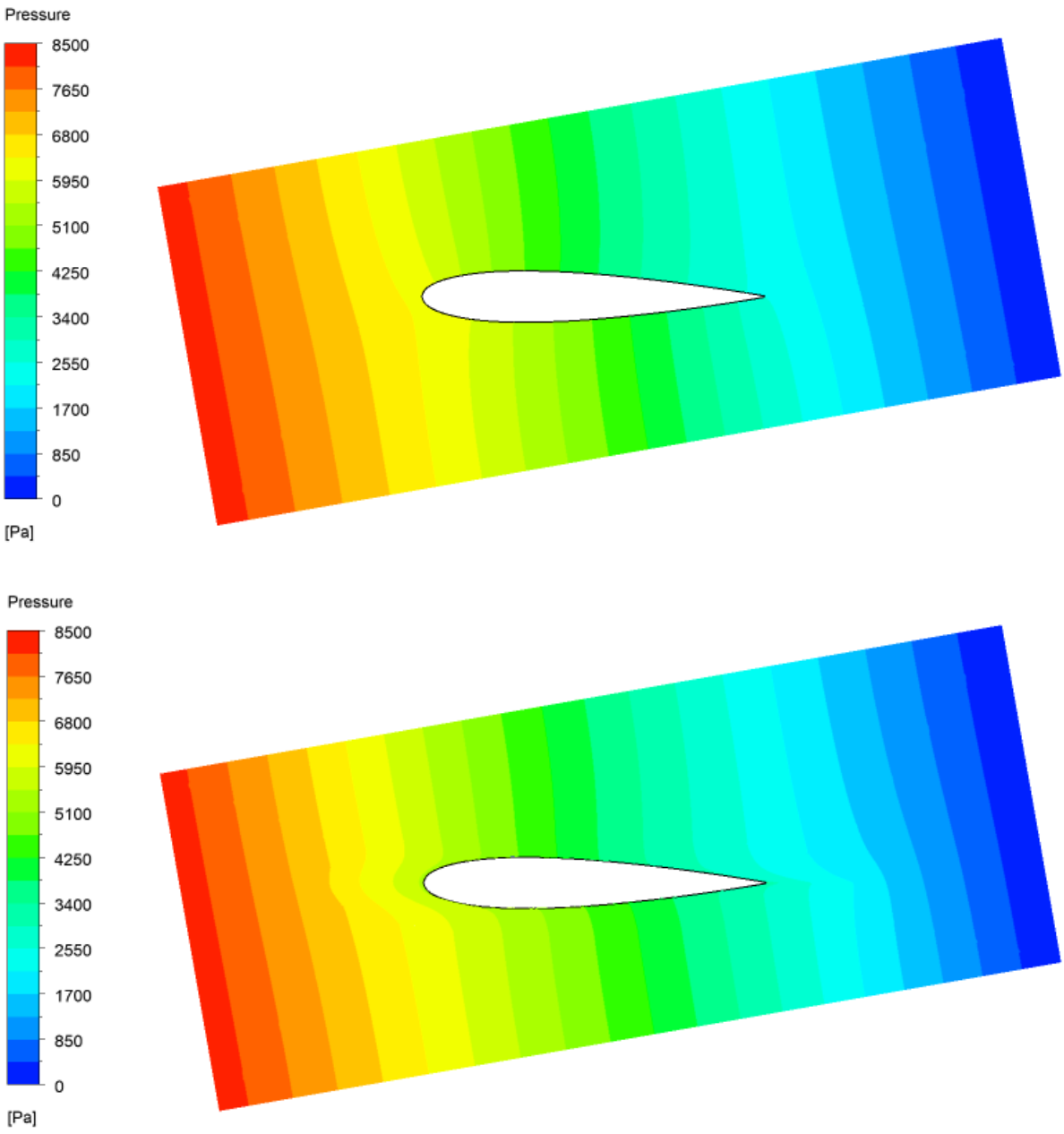

(b) The case without cloak (up) and the case with cloak (down) at Re=10

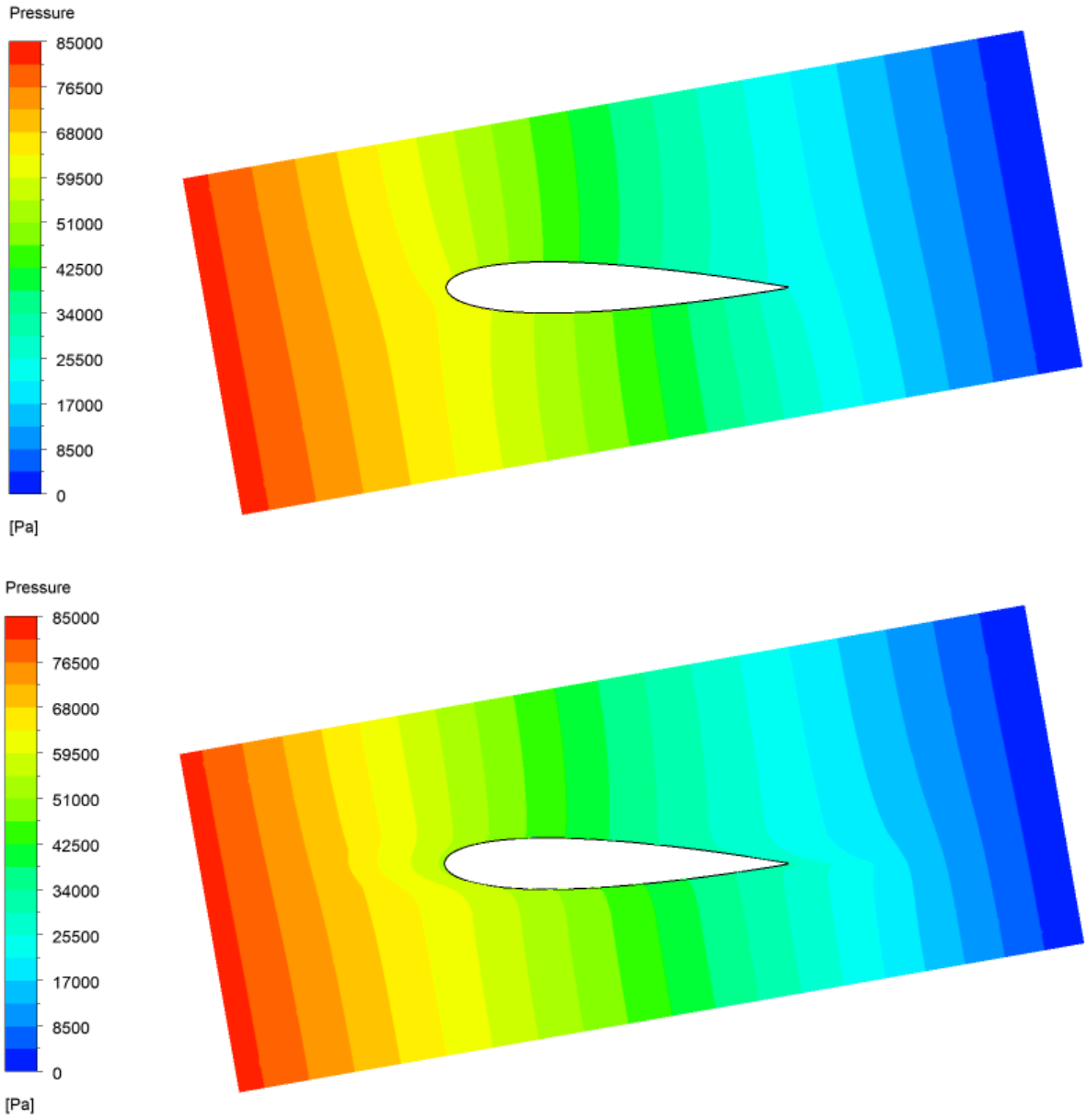

(c) The case without cloak (up) and the case with cloak (down) at Re=100

Figure 43. Pressure fields around the airfoil without and with the improved airfoil cloak cases at 10° angle of attack for different Reynolds numbers

Figures 44, 45 and 46 show the wall skin friction coefficient on the surface of the airfoil without and with cloak at different Re at various angles of attack. In all cases, C_f near the leading edge and the trailing edge is reduced by the cloak significantly. In the center part, C_f is reduced

by a factor of 1.7 compared to that without cloak. When the angle of attack increases, the difference in C_f between the upper surface and the lower surface appears. C_f on the upper surface is larger than that on the lower surface near the leading edge but is smaller near the trailing edge in the cases without cloak. The rapid increase at the trailing edge is caused by the big transition in the geometry model. Because the thickness value in the airfoil shape equation is not 0 at the trailing edge, an arc is used to enclose the airfoil model. That arc causes the rapid change in the airfoil surface and results in some region with high C_f. The difference in C_f between two surfaces is reduced by the cloak, but the effect of the cloak reduces at higher angle of attack.

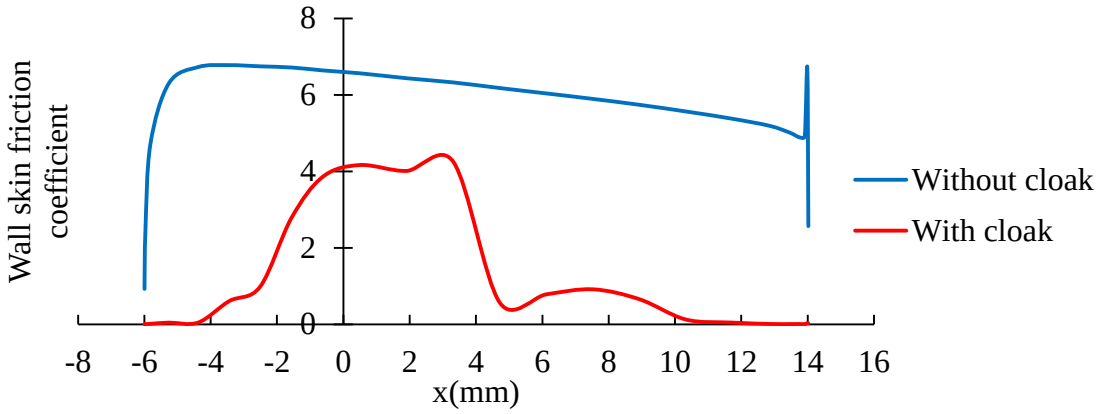

(a) Re=1

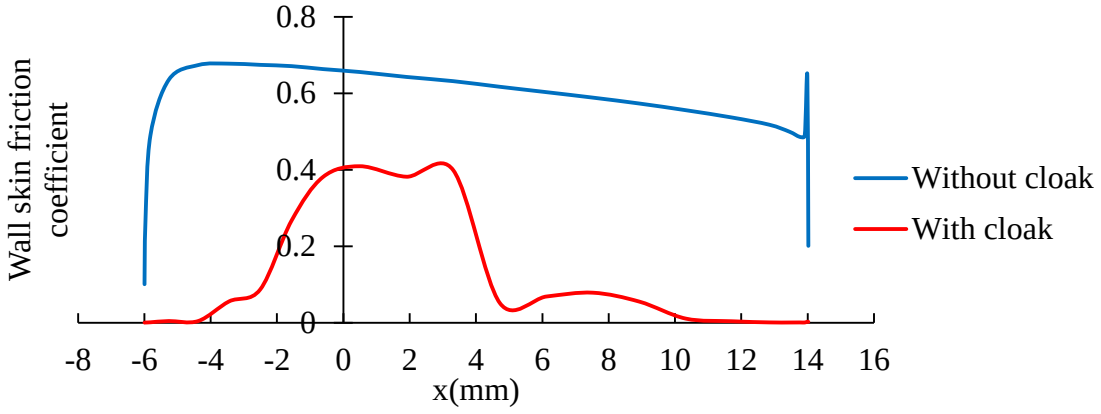

(b) Re=10

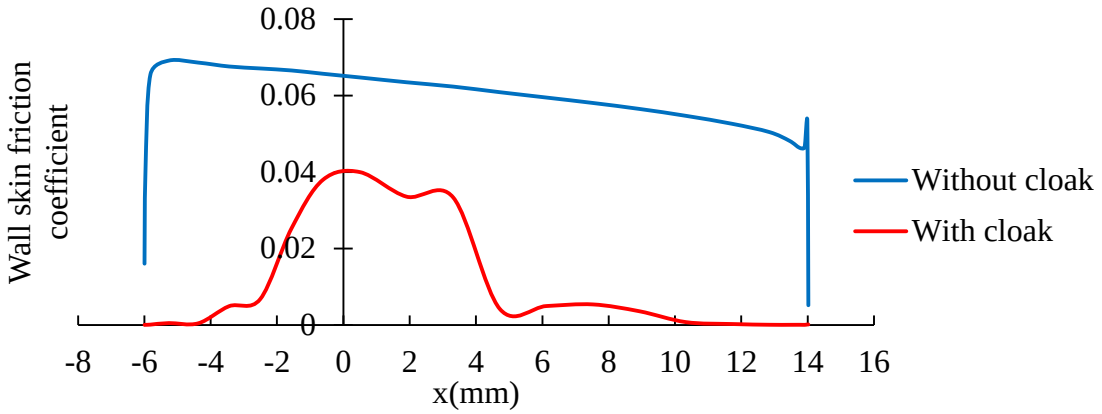

(c) Re=100

Figure 44. Wall skin friction coefficient on the airfoil surface without and with the improved airfoil cloak at 0° angle of attack for different Reynolds numbers

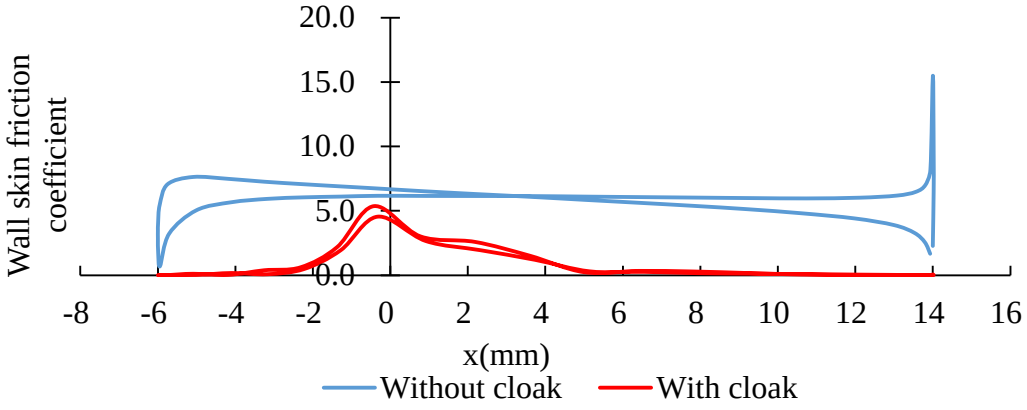

(a) Re=1

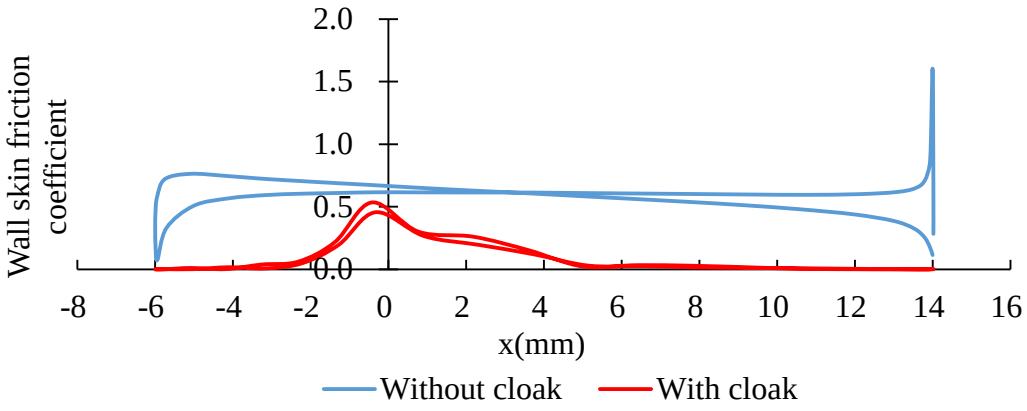

(b) Re=10

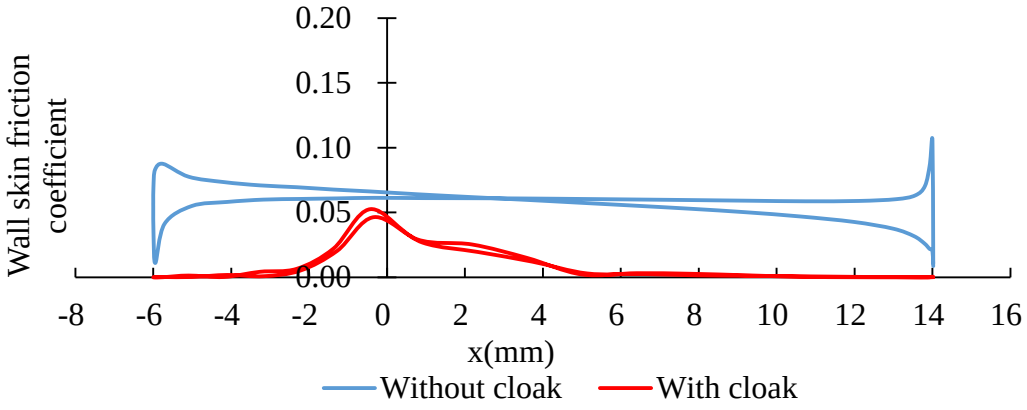

(c) Re=100

Figure 45. Wall skin friction coefficient on the airfoil surface without and with the improved airfoil cloak at 5° angle of attack for different Reynolds numbers

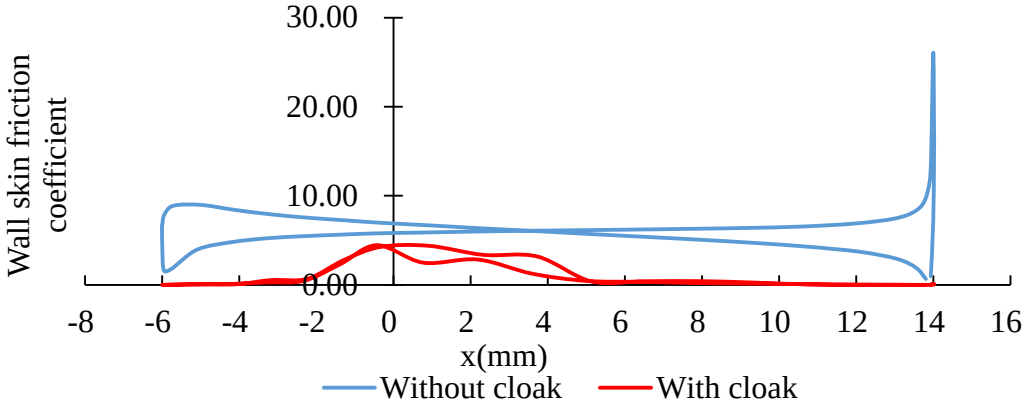

(a) Re=1

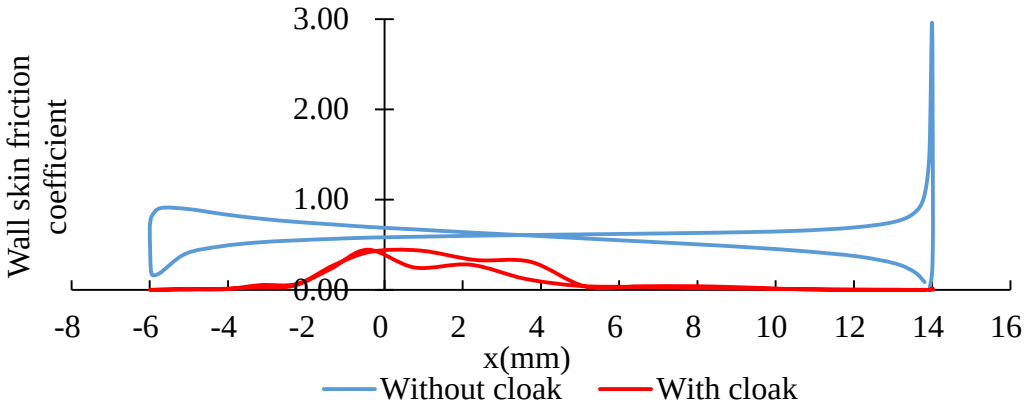

(b) Re=10

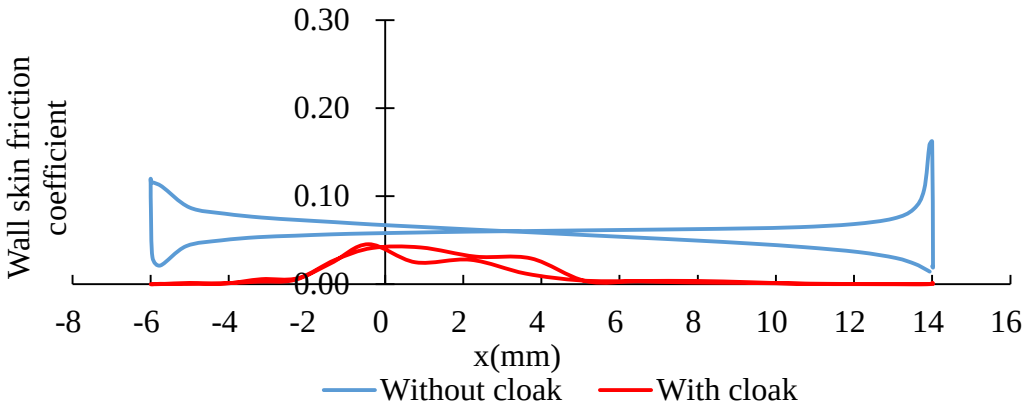

(c) Re=100

Figure 46. Wall skin friction coefficient on the airfoil surface without and with the improved airfoil cloak at 10° angle of attack for different Reynolds numbers

Table 13 shows the drag force on the airfoil without and with the improved airfoil cloak at different angle of attack and Reynolds numbers. In all cases, the pressure force is reduced by about 1.4 times, and the viscous force is reduced by 5 to 7 times compared to that without cloak. The variation with Re and the angle of attack is not obvious. The performance of the cloak at small angle of attack is still significant.

Table 13. Drag force on the airfoil without and with the improved airfoil cloak at various angles of attack and Reynolds numbers

Angle of attack (°)	Re	Pressure Force(μN)		Viscous Force(μN)		Total Drag Force(μN)	
		Without Cloak	With cloak	Without Cloak	With Cloak	Without Cloak	With Cloak
0	1	40.60	29.20	0.675	0.115	41.28	29.32
	10	406.0	290.5	6.70	1.45	412.7	292.0
	100	4040	2895	67	13	4107	2908
5	1	39.85	28.15	0.655	0.100	40.51	28.25
	10	398.2	281.6	6.54	0.995	404.7	282.6
	100	3956.8	2829.2	65.015	9.78	4021.815	2838.98
10	1	39.25	27.50	0.645	0.120	39.90	27.62
	10	392.1	275.2	6.48	1.18	398.53	276.4
	100	3879	2760	64.4	11.5	3944	2771

Thus, the improved airfoil cloak shows significant drag reduction at smaller angle of attack at low Reynolds number as expected.

Chapter 5: Conclusions

In this thesis, the working principles of a HDMM cloak are analyzed. By distorting the velocity field and pressure field in the cloak region, the influence of the object on the region outside the cloak is reduced and the drag force is reduced. Both hydrodynamic hiding effect and drag reduction effect reduce at high Reynolds number because the viscosity tensor in the cloak region is derived from simplified N-S equation at low Reynolds number (known as the Stokes equations).

A feasible method to design a HDMM cloak for objects with various shapes is proposed in this thesis. By stretching a circular cylinder cloak, a new viscosity tensor can be generated for HDMM cloaks for an elliptic-cylinder, a thin vertical elliptic-cylinder (like a flat plate) and an airfoil at an angle of attack. Although the hydrodynamic hiding effect and drag reduction effect of the cloak are weakened if the geometry of the objects is different from a circular cylinder, the hydrodynamic hiding effect and drag reduction effect are still significant.

References

[1] R. Truesdell, A. Mammoli, P. Vorobieff, F. van Swol, and C. J. Brinker. (2006). Drag reduction on a patterned superhydrophobic surface. *Phys. Rev. Lett.* 97, 044504.

[2] U. Leonhardt. (2006). Optical conformal mapping. *Science* 312, 1777-1780.

[3] J.B. Pendry, D. Schurig, and D. R. Smith. (2006). Controlling electromagnetic fields. *Science* 312, 1780.

[4] R. Schittny, M. Kadic, S. Guenneau, and M. Wegener. (2013) Experiments on transformation thermodynamics: Molding the flow of heat. *Phys. Rev. Lett.* 110, 195901.

[5] R. Guenneau, C. Amra, and D. Veynante. (2012) Transformation thermodynamics: Cloaking and concentrating heat flux. *Opt. Express* 20, 8207.

[6] S. A. Cummer, B.-I. Popa, D. Schurig, D. R. Smith, J. Pendry, M. Rahm, and A. Starr. (2008). Scattering theory derivation of a 3D acoustic cloaking shell. *Phys. Rev. Lett.* 100, 024301.

[7] S. Zhang, C. Xia, and N. Fang. (2011). Broadband acoustic cloak for ultrasound waves. *Phys. Rev. Lett*. 106, 024301.

[8] S. Bückmann, M. Thiel, M. Kadic, R. Schittny, and M. Wegener. (2014). An elasto-mechanical unfeelability cloak made of pentamode metamaterials. *Nat. Commun*. 5, 4130.

[9] R. Bückmann, M. Kadic, R. Schittny, and M. Wegener (2015). Mechanical cloak design by direct lattice transformation. *Proc. Natl. Acad. Sci. U.S.A.* 112, 4930.

[10] Y. A. Urzhumov and D. R. Smith. (2011). Fluid flow control with transformation media. *Phys. Rev. Lett*. 107, 074501.

[11] Y. A. Urzhumov and D. R. Smith. (2012). Flow stabilization with active hydrodynamic cloaks. *Phys. Rev. E* 86, 056313.

[12] D. Culver and Y. Urzhumov. (2017). Forced underwater laminar flows with active magnetohydrodynamic metamaterials. *Phys. Rev. E*, 96, 063107.

[13] J. Park, J. R. Youn and Y. S. Song. (2019). Hydrodynamic metamaterial cloak for drag-Free Flow. *Phys. Rev. Lett,* 123, 074502.

[14] H. Chen, C. T. Chan and P. Sheng. (2010). Transformation optics and metamaterials. *Nature Materials,* 9, 387–396.

[15] D. Schurig, J. J. Mock, B. J. Justice and S. A. Cummer. (2006). Metamaterial electromagnetic cloak at microwave frequencies. *Science,* 314, 977-980.

[16] N. Stenger, M. Wilhelm, and M. Wegener. (2012). Experiments on elastic cloaking in thin plates. *Phys. Rev. Lett*. 108, 014301.

Curriculum Vita

Rong Zou

EDUCATION

M.S. in Mechanical Engineering, Department of Mechanical Engineering and Materials Science, Washington University in St. Louis, Saint Louis, MO, USA, 2019-2020

B.S. in Naval Architecture and Ocean Engineering, Department of Vehicle Engineering and Mechanics, Dalian University of Technology, Dalian, China, 2014-2018

PUBLICATIONS

Rong Zou and Ramesh Agarwal, “Evaluation of the Concept of Hydrodynamic Metamaterial Cloak for Drag Reduction,” 2020 AIAA Aviation and Aeronautics Forum and Exposition, Reno, NV, June 2020.